

Applications of Seismic Interferometry in Microseismic Monitoring

by

Yoones Vaezi

A thesis submitted in partial fulfillment of the requirements for the degree of

Doctor of Philosophy

in

Geophysics

Department of Physics
University of Alberta

© Yoones Vaezi, 2016

Abstract

Microseismic monitoring involves the acquisition of continuous seismic data for the purpose of locating and characterizing microseismicity induced mainly by oilfield completion and production processes. Since its inception, microseismic monitoring has proved to be an invaluable tool for understanding underground processes and monitoring subsurface changes associated with hydraulic fracturing, steam stimulation, geothermal energy production, underground deep mines, and CO₂ storage and sequestration. Different existing and emerging new techniques are progressively being employed by the microseismic monitoring industry to provide an even more detailed and comprehensive analysis of the available data. This thesis focuses on potential applications of seismic interferometry in microseismic monitoring, a rather new method which has shown extensive applications in exploration geophysics and global seismology.

Seismic interferometry mainly refers to a technique used for recovering the Green's function between two receivers by crosscorrelating their passive seismic noise recordings, thereby emphasizing the coherent part of noise which is deeply buried under local seemingly incoherent noise. We have used this property to obtain body waves propagating along borehole geophones deployed in downhole microseismic experiments, and therefore, obtain the associated seismic velocities at the neighboring formations surrounding the wellbore at the intervals between the geophones. Whether or not the coherent body waves appear clearly on the crosscorrelation functions depends on the instrument self-noise and clamping quality of borehole geophones.

By obscuring the coherent noise of interest, instrument self-noise levels that are comparable

with or above background noise levels can challenge seismic interferometry which aims at analysis of coherent features in ambient noise wavefields to reveal subsurface structure. Such high levels of instrument self-noise can also act as a major constraint for the detection of weak microseismic events, in particular for borehole deployments in quiet environments such as below 1.5–2 km depths. Estimates of the instrument self-noise are commonly approximated by power spectral densities at the quiet times. The power spectral densities can also themselves be used as a tool for microseismic event detection as such events typically represent stronger spectral content over a frequency band than that of the background noise. This technique outperforms the common event detection method of short-time average/long-time average by detecting a higher number of weak events while keeping the number of false alarms at a reasonable level. It also has the benefit of providing suitable bandpass filters for better picking and further analysis of the events.

On the other hand, the characteristics of the retrieved crosscorrelation waveforms can give insights about the coupling quality of the geophones to the wellbore wall as better coupled arrays result in body waves reconstructed up to a higher frequency range when compared with poorly clamped geophone arrays.

We also study the potential application of coda wave interferometry for monitoring purposes in a surface microseismic monitoring setting, specifically for a wastewater disposal well. Significant changes in the fluid injection pressure into the underground reservoir can have direct impacts on the seismic velocity variations. The relative velocity variations are estimated by a recently developed version of the coda wave interferometry, known as passive image interferometry, using the time shifts between consecutive correlation functions.

Preface

This dissertation is submitted for the degree of Doctor of Philosophy in Geophysics at the University of Alberta. The research described herein is original, and neither this nor any substantially similar dissertation was or is being submitted for any other degree or other qualification at any other university.

A version of **chapter 2** has been published as Vaezi, Y., and van der Baan, M., 2014, Analysis of instrument self-noise and microseismic event detection using power spectral density estimates, *Geophysical Journal International*, **197**(2), 1076–1089, doi: 10.1093/gji/ggu036. I was responsible for code development, data analysis, figure preparation, and manuscript writing.

A version of **chapter 3** has been published as Vaezi, Y., and van der Baan, M., 2015, Comparison of the STA/LTA and power spectral density (PSD) methods for microseismic event detection, *Geophysical Journal International*, **203**(3), 1896–1908, doi: 10.1093/gji/ggv419. I was responsible for code development, data analysis, figure preparation, and manuscript writing.

A version of **chapter 4** has been published as Vaezi, Y., and van der Baan, M., 2015, Interferometric assessment of clamping quality of borehole geophones, *Geophysics*, **80**(6), WC89–WC98, doi: 10.1190/geo2015-0193.1. I was responsible for code development, data analysis, figure preparation, and manuscript writing.

To my family and loved ones...

Acknowledgements

First and foremost, I would like to offer my sincerest gratitude to my intelligent supervisor, Dr. Mirko van der Baan, who continuously supported me throughout this research with his patience and knowledge. His approach in simplifying difficult concepts by providing easy-to-understand examples has helped me significantly in obtaining a concrete understanding of different problems. His infectious enthusiasm, positive outlook, and ability to spot problems and new applications has fueled my work throughout my PhD. Thank you Mirko!

I would like to thank my family, parents, sister and brother and those without whose support and encouragement I could have not finished my PhD. I owe thanks to Yousef, Shahin, Reza, Afsane, Hadis, and Samyar for your unconditional support, energy and love, and thank you a lot for being beside me.

I also thank Ellie for her unconditional support throughout my PhD.

Special thanks to the members of my supervisory and candidacy committee for their insights and feedback: Dr. Vadim A. Kravchinsky, Dr. Moritz Heimpel, Dr. Douglas R. Schmitt, and Dr. Sergiy Vorobyov. I would like to thank Dr. Moritz Heimpel, Dr. Vadim A. Kravchinsky, Dr. Deyan Draganov, and Dr. Juliana Leung for accepting to be part of the examination committee for my thesis defense.

I also thank Dr. Kristof DeMeersman and Dr. Estelle Rebel, my supervisors during my summer internships in 2014 and 2015 at CGG and BakerHughes in Calgary. I learned a lot from them that helped me considerably during my PhD research. I am very happy to still be in contact with you.

I would also like to thank my colleagues and friends at the University of Alberta for their direct or indirect supports and in particular all the students and staff of the Microseismic Industry Consortium.

I would also like to thank Ruby, Mirko's wife, for her hospitality and being so kind for inviting us to their place every once in a while for a party and fun night.

For chapter 2, I would like to thank Arc Resources, Nanometrics, Spectraseis, and ESG Solutions for their support of the field projects involved in the acquisition of the studied

data sets. I also thank Dr. Neil Spriggs, Dr. Brad Birkelo, and Dr. Vladimir Grechka for many discussions, and two anonymous reviewers for their many comments and suggestions in the process of publishing chapter 2. Also, special thanks to Dr. Alex Goertz for research communications.

For chapter 3, I would like to thank Dr. Neil Spriggs for discussions. I also thank Dr. Honn Kao and another anonymous reviewer for their valuable comments and suggestions in the process of publishing chapter 3.

For chapter 4, I would like to thank Carbon Management Canada and the Natural Sciences and Engineering Research Council of Canada for financial support. Arc Resources, Nanometrics, Spectraseis, ESG Solutions, and ConocoPhillips are particularly appreciated for their support, in terms of providing access to their boreholes, data, and/or help in field logistics. I also thank Dr. Vladimir Grechka for many helpful discussions. I would also like to thank Dr. Deyan Draganov, Dr. Yang Zhao, and an anonymous reviewer for their valuable comments and suggestions in the process of publishing chapter 4, specifically the latter two reviewers for their suggestions to use the frequency-slowness domain as an additional way to represent the crosscorrelation functions and find more suitable band-pass filters.

For chapter 5, I would like to thank an anonymous company for their support and permission to use their data.

My appreciations are extended to the sponsors of the Microseismic Industry Consortium for financial support throughout my PhD research.

Contents

1	Introduction	1
1.1	Background	1
1.1.1	Microseismic monitoring	1
1.1.2	Seismic interferometry	3
1.1.3	Potential applications of seismic interferometry in microseismic monitoring	12
1.1.3.1	Surface-wave tomographic inversion	14
1.1.3.2	Extracting P- and S-wave propagation	16
1.1.3.3	Microseismic event localization	17
1.1.3.4	Interferometric time-lapse analysis	19
1.2	Motivation and contribution	22
1.3	Thesis overview	23
2	Analysis of instrument self-noise and microseismic event detection using power spectral density estimates	25
2.1	Introduction	26
2.2	Rolla microseismic experiment	28
2.3	Evaluation of energy variations	29
2.3.1	Observations	29
2.3.2	Interpretation	30
2.4	Instrument self-noise estimation	31

2.4.1	Method	32
2.4.2	Results	32
2.4.3	Implications	33
2.5	A new method for microseismic event detection and time picking	35
2.6	Discussions	37
2.7	Conclusions	39
3	Comparison of the STA/LTA and power spectral density (PSD) methods for microseismic event detection	49
3.1	Introduction	49
3.2	Methodology	51
3.3	Data set	55
3.4	Results	55
3.5	Discussions	60
3.6	Conclusions	63
4	Interferometric assessment of clamping quality of borehole geophones	71
4.1	Introduction	72
4.2	Methodology	74
4.3	Examples	76
4.4	Discussions	84
4.5	Conclusions	85
5	Passive image interferometry for microseismic time-lapse analysis; application to wastewater disposal monitoring	87
5.1	Introduction	88
5.2	Data set	91
5.3	Crosscorrelation functions	94
5.4	Measurement of the velocity variations	98
5.5	Results	101
5.6	Discussions	104
5.7	Conclusions	106

6	Conclusions and suggested future research	118
6.1	Conclusions	118
6.2	Suggested future research	119
	Bibliography	121

List of Tables

3.1	The parameters used for the STA/LTA and the PSD detection methods. . . .	56
3.2	Comparison of the event statistics between the STA/LTA and the PSD methods.	59
4.1	Summary of data set properties.	77

List of Figures

1.1	Typical microseismic monitoring geometry.	2
1.2	Claerbout's 1D interferometry configuration.	5
1.3	An even distribution of random noise sources.	7
1.4	Theoretically ideal source distribution for seismic interferometry.	8
1.5	2D direct-wave interferometry.	11
1.6	The effect of source distribution on the symmetry of the reconstructed Green's function.	15
1.7	Surface-wave tomographic inversion using seismic interferometry.	16
1.8	Body-wave extraction along a monitoring wellbore array.	18
1.9	Comparison of direct and scattered coda-wave raypaths.	21
1.10	An example for coda wave interferometry concept.	21
2.1	Configuration of Rolla microseismic experiment.	29
2.2	Rolla pump curves and the corresponding time series.	40
2.3	Energy variations in Rolla during the treatment time at the shallowest borehole geophone and a surface seismometer.	41
2.4	Average PSD and the corresponding percentiles for two Rolla borehole geophones compared with different noise models.	42
2.5	Average PSD and the corresponding percentiles for two Rolla surface seismometers compared with different noise models.	43
2.6	The time-frequency representation of PSD variations for the vertical component of the shallowest borehole receiver in Rolla.	44
2.7	The time-frequency representation of PSD variations for the vertical component of two surface seismometers in Rolla.	44
2.8	Variation of minimum magnitude detection threshold with distance from the observation well.	45

2.9	Crosscorrelation functions between the vertical component of the shallowest receiver and all other receivers in the Rolla borehole array.	46
2.10	Example microseismic events in Rolla along with their estimated PSDs compared with PSDs of noise-only segments and the average PSD of the data. . .	47
2.11	PSD event detection method and its application to Rolla data set, compared with the STA/LTA technique.	48
3.1	The Z-component of a segment of the raw continuous microseismic data and its zoomed view.	56
3.2	Average PSD estimate along with its standard deviations at each frequency, and PSDs for four events and two sample noise recordings.	57
3.3	The time-frequency representation of the PSD ratios.	64
3.4	The STA/LTA ratio and PSD detection criterion.	65
3.5	Example events of different discriminating frequencies detected by the PSD method mainly related to small regional earthquakes.	66
3.6	Example events detected by the PSD method when applied to raw data but missed by the STA/LTA technique when applied to notch-filtered data. . . .	67
3.7	An example event detected by the PSD method when applied to raw data but missed by the STA/LTA technique when applied to band-passed data. . .	68
3.8	Two example false alarms by the PSD method.	69
3.9	The discriminating frequencies corresponding to each master event detected by the PSD technique.	70
4.1	Processing flowchart for generation of crosscorrelation functions and assessment of clamping quality of a geophone in a borehole array.	75
4.2	Acquisition geometries of different data sets which are assessed in terms of clamping quality of geophones.	77
4.3	The averaged crosscorrelation functions and sonic velocity log for data set A.	78
4.4	The averaged crosscorrelation functions and sonic velocity log for data set B.	79
4.5	The averaged crosscorrelation functions and sonic velocity log for data set C.	80
4.6	The crosscorrelation functions calculated between different components of the shallowest receiver and the corresponding components at other receivers of the array in data set D.	82
4.7	The crosscorrelation functions calculated between different components of the 4th receiver and the corresponding components at other receivers of the array in data set D.	83
5.1	Relative locations and configuration of 5 surface seismometers and the injection wellbore for a wastewater disposal project in northeast British Columbia.	92

5.2	Injection pressure and injection volume curves and monthly event magnitude statistics.	93
5.3	Daily averaged ambient noise spectrograms for stations G006 and G008, and the corresponding amplitudes averaged over a 0.3–0.8 Hz frequency band. . .	96
5.4	The 31-day stacked crosscorrelation functions filtered in the 0.3–0.8 Hz frequency band computed between stations G006 and G008, and the corresponding reference correlation function.	108
5.5	Relative velocity variations and the associated coherency and errors calculated using stretching and doublet methods for station pair G006–G008 in the frequency band between 0.3 and 0.8 Hz at the lapse-time interval between 15 and 70 s in the causal part of the crosscorrelation functions.	109
5.6	Comparison of stability of velocity variation estimations using stretching and doublet methods.	110
5.7	Opposite behavior between the velocity variations estimated from the causal and acausal parts of the crosscorrelation functions for station pair G006–G008.	111
5.8	Opposite behavior between the velocity variations estimated from the causal and acausal parts of the crosscorrelation functions for station pair G008–G010.	112
5.9	The sudden shift on January 10th, year 2, in the crosscorrelation functions towards negative lags for the station pair G008–G010 in the frequency range between 0.3 and 0.8 Hz.	113
5.10	The relative velocity variations estimated at different frequency ranges for station pair G007–G010.	114
5.11	Comparison of the estimated relative velocity variations with environmental data, noise energy, and injection pressure and volume.	115
5.12	A schematic showing the effect of poroelastic stress variations due to injection pressure changes on the velocity changes beyond the injection point.	117

List of Symbols and Abbreviations

- 1D: One-dimensional.
- 2D: Two-dimensional.
- 3D: Three-dimensional.
- 3C: Three-component.
- CF: Characteristic function.
- E-W: East-west.
- FBA: Force balance accelerometer.
- $f - k$: Frequency-wavenumber.
- $f - p$: Frequency-slowness.
- HNM: High noise model.
- LNM: Low noise model.
- LPLD: long-period long-duration.
- LTA: Long-term average.
- N-S: North-south.
- PSD: Power spectral density.
- RMS: Root-mean-square.
- SNR: Signal-to-noise ratio.
- STA: Short-term average.
- STA/LTA : short-time average/long-time average.
- VSP: Vertical seismic profile.

CHAPTER 1

Introduction

1.1 Background

Since its inception in the 1970s and its commercialization in 2000, microseismic monitoring has proved to be an invaluable tool for understanding underground processes in oil and gas and mining industries. Applications of existing and emerging new techniques are being extended to microseismic monitoring that can add even more to its deliverables and therefore provide a more detailed and comprehensive understanding of the subsurface. In this thesis, we investigate the potential applications of seismic interferometry in microseismic monitoring, a rather new method which has shown significant applications in exploration geophysics and global seismology.

1.1.1 Microseismic monitoring

Microseismic monitoring is a term commonly used to refer to methods that include the acquisition of continuous seismic data for the purpose of locating and characterizing microseismicity induced by oilfield completion and production processes. This information can further be used for monitoring resulting reservoir changes and understanding the associated geomechanical processes in the subsurface. It is not only considered as the main technology for monitoring of hydraulic stimulation of "tight" (very low permeability) hydrocarbon reservoirs and steam injection into heavy-oil fields, but is also proven to be useful for geothermal studies, reservoir surveillance, and monitoring of CO₂ storage and sequestration and underground deep mines (Phillips et al., 2002; Maxwell et al., 2004; Maxwell, 2011; McGillivray, 2005; Warpinski, 2009; Verdon et al., 2010; van der Baan et al., 2013). Here, the terms 'microseismicity' or 'microearthquake' are defined as seismicity of magnitude less

than 0 (Maxwell et al., 2010b) and should be distinguished from the terms ‘microtremor’ or ‘microseism’ that commonly refer to more or less continuous motion with a period of 4 to 20 seconds in the Earth, that is unrelated to an earthquake (Ewing et al., 1957; Lee, 1935).

Microseismic monitoring differs in many respects from seismic reflection surveys that are traditionally used for oil and gas exploration and development, including the type of sources, receivers, and methods of analysis. For instance, the process of hydraulic fracturing (also known as “fracking”) involves injecting large volumes of fluids under high pressure into an unconventional (tight) hydrocarbon reservoir formation with the purpose of enhancing the reservoir permeability through creation of additional fluid pathways leading to the production well. This causes stress changes that can lead to deformation of the rockmass. The effects of pressure perturbations and fluid movements can lead to failure in the form of fracturing in the rockmass. Knowing where hydraulic fractures have been created helps in predicting fluid flow, designing additional fractures, and positioning additional production wells.

Microseismic data are typically broadband (10–1000 Hz) and recorded at high sampling rates with three-component (3C) instruments. They are acquired with either an array of seismic instruments (geophones or accelerometers) in one or multiple wellbores, or with a large number (100 to more than 1000) of geophones near or on the surface (Figure 1.1).

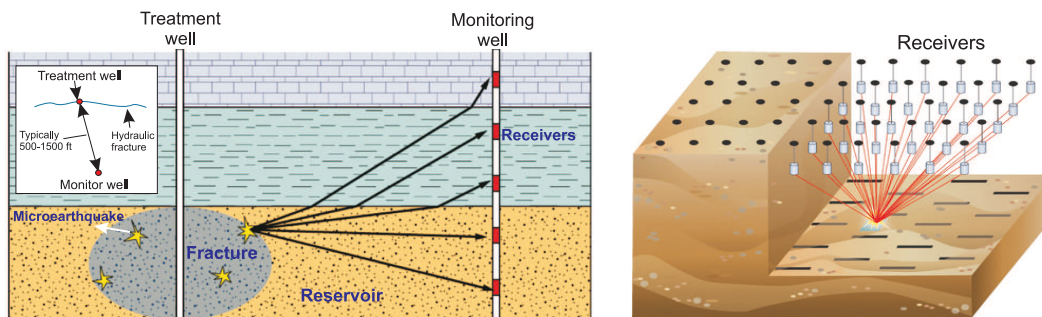


Figure 1.1: Typical monitoring geometries for microseismic data acquisition. The microseismic data are recorded either by borehole (left), or surface or near-surface (right) receivers. Taken from National Research Council (2013) and Warpinski (2009).

The basic microseismic process and strategy are not difficult; they are a direct application of standard earthquake seismology principles that have been developed, used, and tested for decades. Using specialized data processing techniques the accurately detected and picked microseismic events on the recorded data are precisely located in the subsurface to provide valuable information about fracture growth, size, and orientation, etc. If the data are adequate, one can also compute source parameters such as seismic moment, magnitude, and

moment tensors. This information is useful for understanding the geomechanical behavior of the reservoirs, which can in turn reduce the risk associated with the drilling and production operations. The real-time analysis of the data allows aiding the design of hydraulic fracturing procedures, such as injection rate and fluid volume. It can also help completion engineers in wellbore placement and spacing during the infill drilling procedure at the field development stage.

1.1.2 Seismic interferometry

The first derivation of seismic interferometric theory was published for one-dimensional (1D) media by Claerbout (1968), and extended using modal theory by Weaver and Lobkis (2001) and Lobkis and Weaver (2001). It was eventually proved for fully three-dimensional (3D) acoustic media (Wapenaar, 2003; van Manen et al., 2005, 2006; Wapenaar et al., 2010a,b), elastic media (Wapenaar, 2004; Snieder et al., 2006; van Manen et al., 2006; Wapenaar and Fokkema, 2006) and electromagnetic media (Slob et al., 2007; Slob and Wapenaar, 2007), and a unified approach allows application to other wave phenomena such as seismoelectric wave propagation and diffusive wavefields (Wapenaar et al., 2006; Snieder et al., 2007; Vasconcelos, 2008).

As mentioned above, the idea of seismic interferometry was first conceived by Claerbout (1968). He showed that if a 1D medium is bounded on top by a free surface (like the surface of the Earth) and is bounded below by a half-space (homogeneous, infinitely extensive Earth), then the plane-wave reflection response of a horizontally layered medium (what we would record at the surface of the Earth given a source also at the surface) can be obtained directly by autocorrelation of the transmission response (crosscorrelation of the transmission response with itself). This is shown in Figure 1.2. Note that for any two time-dependent wavefields $u_a^{(s)}(t)$ and $u_b^{(s)}(t)$ from the source s recorded by two sensors at a and b the crosscorrelation function over the time interval $[0, T]$ with time lag τ is given by

$$C_{ab}^{(s)}(\tau) = \int_0^T u_a^{(s)}(t)u_b^{(s)}(t + \tau)dt = u_a^{(s)}(-\tau) * u_b^{(s)}(\tau), \quad (1.1)$$

where $*$ means convolution, which is defined as

$$u_a^{(s)}(t) * u_b^{(s)}(t) = \int_0^t u_a^{(s)}(\tau)u_b^{(s)}(t - \tau)d\tau. \quad (1.2)$$

The Fourier transform of a time dependent function $f(t)$ is given by

$$\hat{f}(\omega) = \int_{-\infty}^{\infty} f(t)e^{-j\omega t}dt, \quad (1.3)$$

where ω is the angular frequency and j is the imaginary unit.

The convolution theorem proves that the Fourier transform of the convolution between two functions is equal to the product of the individual Fourier transforms. As time reversal corresponds to complex conjugation in the frequency domain, so the crosscorrelation is, in the frequency domain, given by

$$\hat{C}_{ab}(\omega) = \hat{u}_a^*(\omega)\hat{u}_b(\omega), \quad (1.4)$$

where the asterisk denotes complex conjugation.

Figure 1.2a shows an impulsive unit source in the lower half-space emitting a vertically upward-propagating plane wave. The first arrival reaches the surface after a time t_0 directly with an amplitude $a_0 = \tau$. Note that τ is the transmission coefficient, r is the reflection coefficient (-1 at the free surface), and c is the propagation velocity of seismic waves in the homogeneous, lossless acoustic layer of thickness Δz sandwiched between a stress-free surface (like the Earth's surface) and a homogeneous lossless half-space. The second arrival, resulting from the wave being reflected downwards by the free surface and then upwards by the interface, occurs at time $t_0 + \Delta t$ (with $\Delta t = 2\Delta z/c$) and has amplitude $a_1 = -r\tau$; subsequent arrivals occur at regular time intervals Δt , and have amplitudes $a_2 = -r^2\tau$, $a_3 = -r^3\tau$, etc (Figure 1.2b). If we denote the global transmission response by $T(t)$ and its time-reverse by $T(-t)$, then the autocorrelation of the global transmission response (i.e. the convolution of the signal with its time-reverse) (Figure 1.2c) yields the global reflection response:

$$T(t) * T(-t) = \delta(t) - R(t) - R(-t), \quad (1.5)$$

where $\delta(t)$ is the Dirac delta function which is here the impulse obtained from autocorrelation for zero lag time, and $R(t)$ and $R(-t)$ are the so-called causal and acausal parts of the autocorrelation, respectively (Wapenaar, 2003; Wapenaar et al., 2010a). Equation 1.5 can also be rewritten as

$$R(t) + R(-t) = \delta(t) - T(t) * T(-t). \quad (1.6)$$

According to equation 1.6 and Figure 1.2c, the Earth's reflection response (from a plane wave source at the surface, a source which did not exist) can be constructed by taking either the positive- or negative-time part of the autocorrelation of its transmission response.

In the case of transient, non-impulsive sources (e.g., ambient noise), equation 1.6 can be modified as follows (Claerbout, 1968):

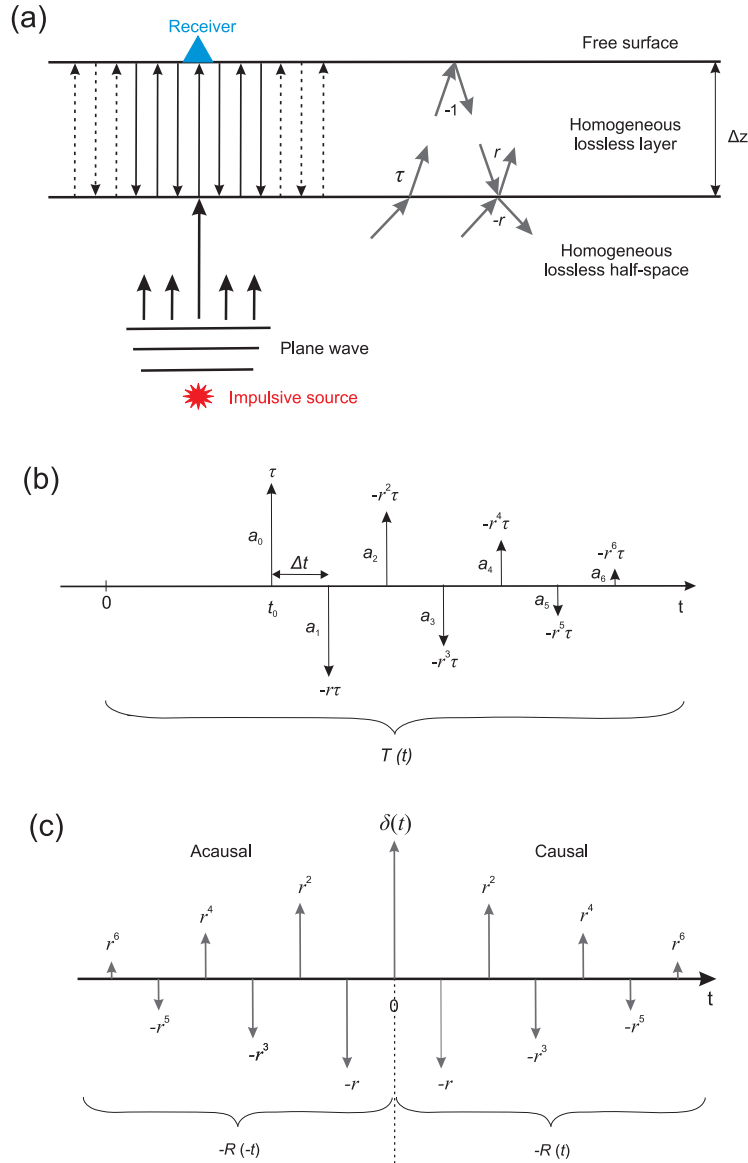


Figure 1.2: (a) Simple layered medium with an upgoing plane wave radiated by a source in the lower half-space. (b) The transmission response $T(t)$ observed at the free surface. (c) The autocorrelation of transmission response. The causal part is, apart from a minus sign, the reflection response $R(t)$. Taken from Galetti and Curtis (2012).

$$(R(t) + R(-t)) * S_N(t) = S_N(t) - \langle u(t) * u(-t) \rangle, \quad (1.7)$$

where $N(t)$ is the noise signal emitted by the source in the lower half-space, $u(t) = T(t)*N(t)$ is the recorded wavefield at the surface, and $S_N(t) = N(t) * N(t)$ is the autocorrelation of the noise source time function. According to equation 1.7, an approximation to the Earth's reflection response can be obtained from the autocorrelation of passive noise transmission records. The theory can be proved to hold for arbitrarily layered media (Claerbout, 1968). Claerbout conjectured that the method could be extended to two-dimensional (2D) and 3D varying media and wavefields, but it was not until 1993 that this was shown to be applicable in reality: Duvall et al. (1993) and Ricket and Claerbout (1999) applied crosscorrelation to records of solar surface noise to obtain the first helioseismological pseudo-impulsive shot records.

Mathematical proofs of 3D seismic interferometry based on representation theorems were derived subsequently by Wapenaar (2003, 2004), van Manen et al. (2005, 2006), Wapenaar and Fokkema (2006), Wapenaar et al. (2006), Slob et al. (2007), Snieder et al. (2007), Vasconcelos (2008), and Wapenaar and van der Neut (2010), and based on a stationary-phase approach by Snieder (2004). The theory has been independently demonstrated through time-reversal laboratory experiments by Lobkis and Weaver (2001), Weaver and Lobkis (2001), Derode et al. (2003a), Derode et al. (2003b), and Larose et al. (2005).

Ricket and Claerbout (1999) made a phenomenal conjecture which states that the cross-correlation of noise traces recorded at two different receiver locations in 3D, heterogeneous media gives the response that would be observed at one of the locations if there were a source at the other. The latter is called a 'virtual' source as it does not really exist (Bakulin and Calvert, 2004, 2006). Weaver and Lobkis (2001) provide one of the first proofs of this conjecture with the assumption that the noise wavefield is diffuse (i.e., waves arrive from all angles with equal strength). Wapenaar (2004) proves the generalization of Claerbout's conjecture (known as seismic interferometry) for 3D (acoustic and elastodynamic) media without assumptions about randomness of the medium, noise sources, or diffusivity of the wavefield. Therefore, seismic interferometry refers to the principle of generating new seismic responses of virtual sources by crosscorrelating seismic observations at different receiver locations (Wapenaar et al., 2010a). This form of seismic interferometry is called inter-receiver interferometry, and it allows one of the receivers to be turned into a virtual (imagined) source. However, inter-receiver interferometry is not the only type of interferometry as two additional forms have recently been developed: inter-source interferometry (Hong and Menke, 2006; Curtis et al., 2009), which allows a real source to be turned into a virtual receiver, and source-receiver interferometry (Curtis, 2009; Curtis and Halliday, 2010), which allows a (perhaps unrecorded) recording of energy traveling between a source and a receiver to be constructed by making use of both virtual sources and virtual receivers.

There are still some fundamental assumptions behind seismic interferometry theory which

currently impose limitations on its domain of applicability. First, if random noise sources (e.g., sources of background noise in the Earth) are to be used in two or three dimensions, then the distribution of that noise must be "even" (Figure 1.3). Second, if active sources are used, then to obtain dynamically correct responses (i.e., with the correct amplitudes) the sources must completely surround the portion of the medium of interest (boundary S in Figure 1.4) (Halliday, 2009). When a free surface (Earth's surface) is present, this surface can form part of the boundary which can be source-free (Figure 1.4c). Third, for an exact application using noise sources on the bounding surface, the medium must be lossless (non-attenuating). Many studies have been undertaken to determine the effect of relaxing some of these constraints.

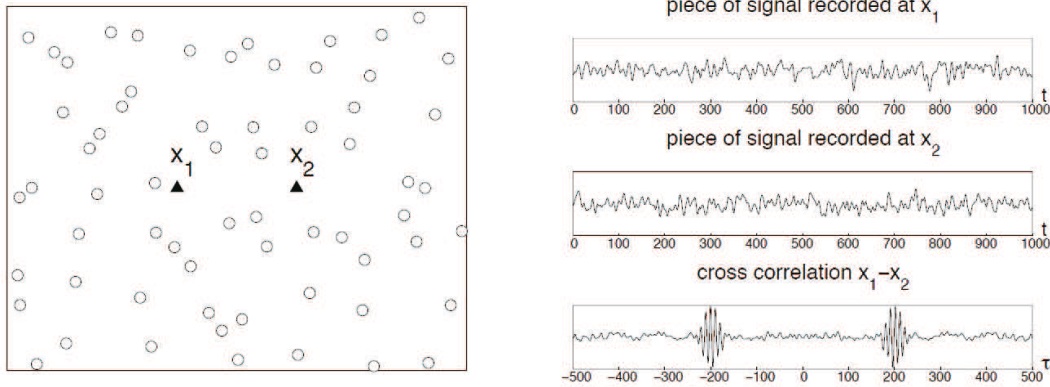


Figure 1.3: Homogeneous distribution of random noise sources around two receivers. The crosscorrelation of the two seemingly uncorrelated noise records at the two receivers results in a response that would have been measured in one of the receivers if there were a source (virtual source) at the location of the other receiver, plus its time-reversed version. These responses are, therefore, related to the inter-receiver Green's function. Taken from Garnier and Papanicolaou (2009).

One can distinguish between controlled-source and passive seismic interferometry. Controlled-source seismic interferometry, pioneered by Schuster (2001), Bakulin and Calvert (2004), and others, comprises a new processing methodology for seismic exploration data. Apart from crosscorrelation, controlled-source interferometry also involves summation of correlations over different source positions. Assuming a mass density $\rho = \rho(x)$ and a propagation velocity $c = c(x)$, for impulsive sources distributed on a boundary S (Figure 1.4) the acoustic representation of the Green's functions based on the concept of seismic interferometry can be written as (Wapenaar, 2006; Wapenaar et al., 2010b; Derode et al., 2003a,b)

$$G(x_B, x_A, t) + G(x_B, x_A, -t) \approx \frac{2}{\rho c} \oint_S G(x_B, x, t) * G(x_A, x, -t) d^2x, \quad (1.8)$$

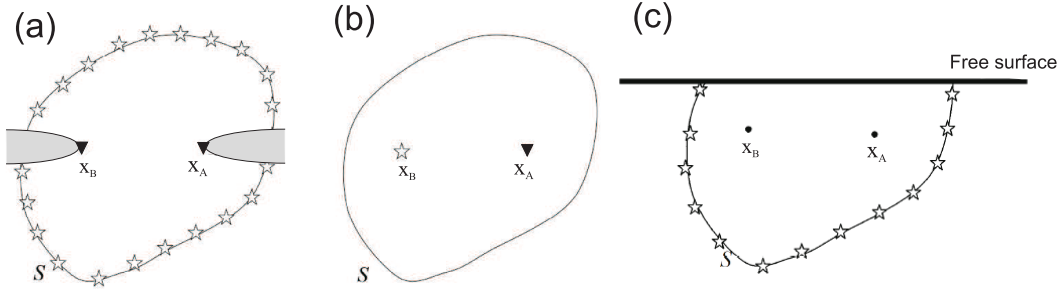


Figure 1.4: (a) Typical configuration for wavefield interferometry. Sources (stars) are located on the arbitrarily-shaped surrounding boundary S and responses are recorded at two receiver positions, x_A and x_B (triangles). Sources located within the grey regions contribute the most to the Green's function computation. (b) Interferometry synthesizes the response as if one of the receivers had been a source. (c) Configuration with a free surface, where the boundary does not span the free surface. Taken from Halliday (2009).

where G denotes the Green's function. The Green's functions are the signals that would be recorded at one receiver if an impulsive point source was fired at the location of the other receiver. The right-hand side represents an integral of crosscorrelations of observations at x_A and x_B , respectively, due to impulsive sources at x on S ; the integration takes place along the source coordinate x . The left-hand side is the superposition of the response from x_A to x_B and its time-reversed version, which is symmetric in time.

Passive seismic interferometry, on the other hand, is a methodology for turning passive seismic measurements (ambient seismic noise or microearthquake responses) into deterministic seismic responses. Traditionally, seismologists analyze waves from earthquakes or artificial energy sources that travel through the Earth, in order to make inferences about Earth's subsurface structure and properties. However ambient seismic noise also constantly travels through the Earth. Somewhere within its complex wavefield, ambient seismic noise must also contain similar information about the Earth's subsurface. When the sources on boundary S are noise sources $N(x, t)$ that act simultaneously for all x on S , the responses at x_A and x_B are $u(x_A, t) = \oint_S G(x_A, x, t) * N(x, t) d^2x$ and $u(x_B, t) = \oint_S G(x_B, x', t) * N(x', t) d^2x$, respectively. We assume that any two noise sources $N(x, t)$ and $N(x', t)$ with $x \neq x'$ are uncorrelated and that their autocorrelation $S_N(t)$ is independent of x . Hence, we assume that the source distribution on boundary S obeys the relation $\langle N(x, -t) * N(x', t) \rangle = \delta(x - x') S_N(t)$, where $\langle \cdot \rangle$ denotes a spatial ensemble average (Roux et al., 2004; Snieder, 2004; Wapenaar et al., 2002; Wapenaar, 2004; Weaver and Lobkis, 2004; Derode et al., 2003b). Equation 1.8 can thus be rewritten as

$$\{G(x_B, x_A, t) + G(x_B, x_A, -t)\} * S_N(t) = \frac{2}{\rho c} \langle u(x_B, t) * u(x_A, -t) \rangle. \quad (1.9)$$

According to this equation, the crosscorrelation of the observed noise fields at x_A and x_B yields the Green's function from x_A to x_B plus its time-reversed version, convolved with the autocorrelation of the noise sources. Therefore, in passive interferometry of ambient noise, no explicit summation of correlations over different source positions is required because the correlated responses are a superposition of simultaneously acting uncorrelated sources.

However, in all cases, the response that is retrieved by crosscorrelating two receiver recordings (and summing over different sources) can be interpreted as the response that would be measured at one of the receiver locations as if there were a source at the other. Because such a point-source response is equal to a Green's function convolved with a wavelet, seismic interferometry is also often called Green's function retrieval (Wapenaar et al., 2010a). The importance of a Green's function is that it contains information about how energy travels through the Earth between the two locations.

Seismic interferometry can also be further classified into direct-wave and reflected-wave interferometry (Wapenaar et al., 2010a). Since microseismic monitoring involves mainly acquisition of passive direct waves, in this context we mainly concentrate on direct-wave interferometry of ambient noise and its applications.

Figure 1.5 shows the latter in a simple 2D example taken from Wapenaar et al. (2010a). Figure 1.5a shows the distribution of point sources, denoted by black dots, on a pineapple slice. They assumed that these sources emit transient signals that propagate at a velocity of 2000 m/s through a homogeneous medium to two receivers at x_A and x_B , which are 1200 m apart. The positions of the sources are represented by their radius r_S from the center and azimuth φ_S . Figure 1.5b and c show the responses at the points x_A and x_B , respectively. Figure 1.5d shows the correlation gather, where each signal is the crosscorrelation between responses at x_A and x_B for each source separately. Despite the randomness of the traveltimes in Figures 1.5b and c the arrival times in the correlation gather vary smoothly with φ_S . This is because only the time difference along the paths from each source to the receivers matters in the crosscorrelation process.

The summation of the waves in Figure 1.5d over all angles results in the time-symmetric response shown in Figure 1.5e, which consists of two waves arriving at 0.6 s and -0.6 s, respectively. As discussed earlier, these events are equivalent to the response of the medium at x_B to a source at x_A . Note that the crosscorrelation of signals emitted by a source at $\varphi_S = 0^\circ$ reveals a wave arriving at time $(|x_A - x_S| - |x_B - x_S|)/c = -|x_B - x_A|/c = -0.6$ s at $\varphi_S = 0^\circ$ in Figure 1.5d. Similarly, the crosscorrelation of signals emitted by a source at $\varphi_S = 180^\circ$ reveals a wave arriving at time 0.6 s at $\varphi_S = 180^\circ$ in Figure 1.5d. In the

sum, only signals arriving at ± 0.6 s survive. Waves emitted by sources in the vicinity of $\varphi_S = 0^\circ$ and $\varphi_S = 180^\circ$ – the so-called stationary-phase zones delimited by dashed lines in Figure 1.5a and d – interfere constructively, whereas waves excited by sources at other angles interfere destructively. The noise that exists between the two events in Figure 1.5e is due to the fact that noise sources outside the stationary phase zone cancel each other completely only when they are sufficiently close to each other. The stationary-phase zones are also referred to as Fresnel zones.

When independent transient sources are replaced by simultaneously acting noise sources the cross-terms disappear, if the noise sources are uncorrelated. Hence, a single crosscorrelation of noise observations at x_A and x_B suffices to obtain inter-receiver Green’s function plus its time-reversed version, convolved with the autocorrelation of the noise source time function (Figure 1.5f). Note that the symmetry of the responses in Figure 1.5e and f relies on the isotropic illumination of the receivers.

Of course, what is demonstrated here for a 2D distribution of sources also holds for a 3D source distribution. In that case, all sources in Fresnel volumes rather than Fresnel zones contribute to the retrieval of the direct wave between x_A and x_B .

Therefore, seismic interferometry allows us to decode the information contained in the ambient noise wavefield to create a useful signal, in fact an artificial seismogram, from what used to be called noise. This is why seismic interferometry is considered as a method for ‘turning noise into signal’ (Curtis et al., 2006). This new seismogram can then be used to image the subsurface of the Earth using traditional seismological tomographic or imaging methods.

Other than crosscorrelation-type interferometry, a few alternative seismic interferometry implementations have been developed in the last few years. Slob et al. (2007) introduced the application of seismic interferometry by crossconvolution instead of crosscorrelation. In this case, one of the receivers needs to be located outside a volume surrounded by sources, and the other receiver inside this volume. The advantage of this approach is that losses are treated correctly. Also, losses are treated correctly when crosscorrelations of source responses are added that precisely compensate for the losses (Snieder, 2007). However, the necessary sources are unlikely present in an actual medium. As explained in Wapenaar et al. (2010b), a deconvolution of the wavefields detected at two different receivers (e.g., Trampert et al. (1993); Snieder and Safak (2006); Vasconcelos and Snieder (2008)) may be casted in the framework of seismic interferometry. The disadvantage of this approach is the need for stabilization. The advantage is that losses are well accounted for. Besides losses, also an irregular source distribution may lead to suboptimal Green’s function retrieval by crosscorrelation seismic interferometry. Given a well sampled receiver array, besides losses and source wavelets, also imprints of an irregular source distribution can be deconvolved for.

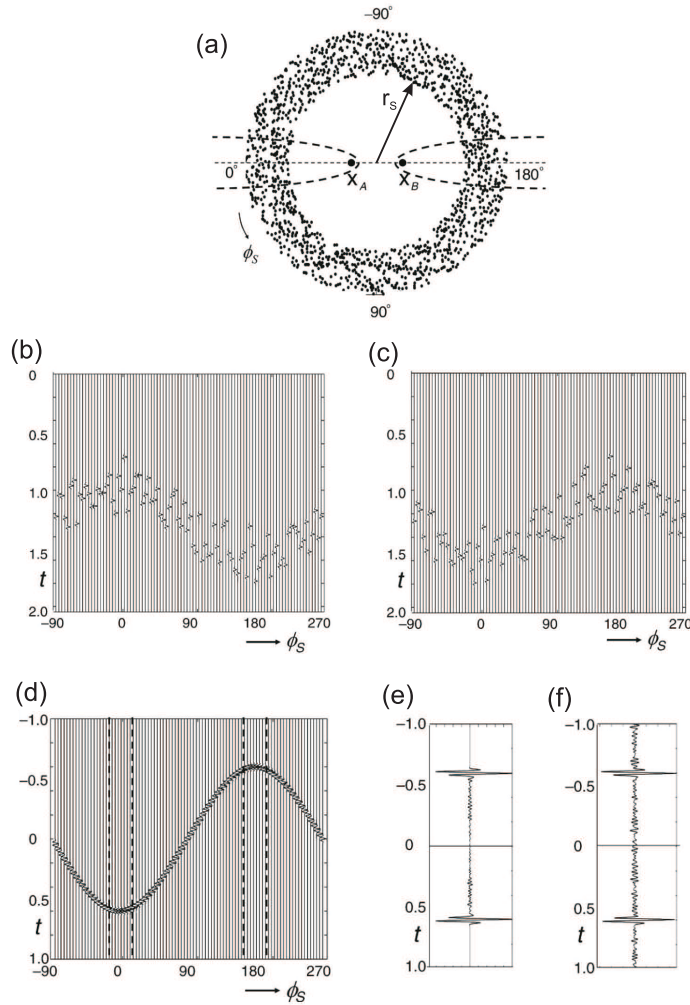


Figure 1.5: Direct-wave interferometry in a 2D example. (a) Isotropic distribution of point sources around the receivers at x_A and x_B . The stationary phase zones (Figure 1.4) are indicated by the thick dashed lines. (b) Responses at x_A as a function of the (polar) source coordinate ϕ_S . (c) Responses at x_B . (d) Crosscorrelation of the responses at x_A and x_B . The dashed lines here also show the stationary phase zones. (e) The sum of the correlations in (d). This is interpreted as sum of Green's function between the receivers and its time-reversed version, convolved with the wavelet autocorrelation. The main contributions come from sources in the stationary phase zones indicated in (a) and (d). (f) Single crosscorrelation of the responses at x_A and x_B of simultaneously acting uncorrelated noise sources. Taken from Wapenaar et al. (2010a).

This is achieved by replacing the 1D deconvolution by a 2D or 3D deconvolution (Schuster and Zhou, 2006; Wapenaar et al., 2008a,b). Crosscoherence is another algorithm that can

be used for seismic interferometry (Aki, 1957; Prieto et al., 2009). However, we only use the crosscorrelation-type interferometry throughout this thesis due to its generality and simplicity.

1.1.3 Potential applications of seismic interferometry in microseismic monitoring

The applications of seismic interferometry span a number of different fields, including crustal seismology, volcano monitoring, and industrial exploration. Almost all of these applications take advantage of the fact that inter-receiver interferometry allows real receivers to be converted into virtual sources, hence increasing the number of available sources and possible source-receiver paths. As of today, surface wave tomographic inversion in global and regional scales to obtain Rayleigh and Love wave velocity maps (Campillo and Paul, 2003; Shapiro and Campillo, 2004; Shapiro et al., 2005) remains the most common application.

Body waves may also be extracted from seismic interferometry of closely spaced receivers (Roux et al., 2005; Draganov et al., 2007; Gerstoft et al., 2008; Zhang et al., 2010; Ruigrok et al., 2011). Miyazawa et al. (2008) extract P- and S-waves from noise crosscorrelation on a vertical array deployed for monitoring steam injection into an oil reservoir. Grechka and Zhao (2012) retrieved body waves and the inferred corresponding formation velocity models nearby the wellbore from correlation of noise records at borehole geophones in different single and crosswell acquisition geometries in microseismic monitoring experiments and for the horizontal and vertical observation wells. Their velocity estimates are comparable to the existing velocity models obtained from well logs.

In industrial exploration geophysics, some of the first applications of seismic interferometry were to perform seismic imaging and redatuming of sources to the positions of receivers (Schuster, 2001; Schuster et al., 2004). Schuster's work inspired many other researchers to develop interferometric methods for exploration geophysics. For example, vertical seismic profile (VSP) data can be transformed into crosswell data (Minato et al., 2007) or into single-well reflection profiles to improve salt-flank delineation and imaging (Willis et al., 2006; Xiao et al., 2006; Hornby and Yu, 2007; Lu et al., 2008). Interferometry can be used to turn multiples in VSP data into primaries and in this way enlarge the illuminated area (Yu and Schuster, 2006; He et al., 2007; Jiang et al., 2007). Surface multiples can be turned into primaries at the position of missing traces (Wang et al., 2009).

Crosscorrelation (plus convolution) of refracted waves gives virtual (and supervirtual) reflections that can be used for better first-break picking and, therefore, improved estimation of the subsurface parameters (Dong et al., 2006a; Mikesell et al., 2009; Mallinson et al., 2011; Vaezi and DeMeersman, 2014). Ground roll (the industrial term for surface waves)

can be predicted by interferometry and subsequently subtracted from exploration seismic data (Curtis et al., 2006; Dong et al., 2006b; Halliday et al., 2007, 2010; Xue et al., 2009). This is important for removal of scattered ground roll (surface waves that have scattered from heterogeneities in the subsurface), which are particularly difficult to remove using standard frequency-wavenumber ($f - k$) filters because they may occupy the same part of the $f - k$ space as the body wave reflections or refractions of interest.

Schuster (2009) systematically discusses all possible interferometric transformations between surface data, VSP data, single-well profiles, and crosswell data. Another approach to interferometric redatuming of controlled-source data, known as the 'virtual-source method' (Bakulin and Calvert, 2004, 2006), is based on the principles of time-reversed acoustics. This method allowed the authors to image below the complex surface overburden by turning real downhole receivers into virtual sources. Hence, many of the distortions caused by the complex near-surface are eliminated, providing much cleaner and distortion-free data, without any knowledge of the complex overburden.

Bakulin et al. (2007) and Mehta et al. (2008) suggest how the virtual-source method may also be used as a time-dependent reservoir monitoring technique thanks to its ability to eliminate the effect of temporal variations in the overburden. King et al. (2011) introduce the method of 'interferometric velocity analysis', which allows layer velocity and thickness to be retrieved using non-physical as well as physical energy. The recent passive monitoring investigations find their roots in the early work of Poupinet et al. (1984), who proposed the measurement of small velocity variations using the direct arrivals of earthquake multiplets. This technique, which was originally called the doublet technique in seismology, was later revisited by coda wave interferometry from repetitive sources (earthquake doublet or repeated artificial seismic sources) in geophysics at higher frequencies and on smaller scales (Snieder et al., 2002; Snieder, 2006; Grêt et al., 2005). Also a new advancement to the coda-wave interferometry technique introduced by Sens-Schönfelder and Wegler (2006) was to replace the use of repetitive sources by the computation of the seismic-noise correlation function between two sensors. The coda of the estimated Green's function are examined to find time shifts that are directly related to the relative velocity variations in the medium. This method is commonly referred to as 'passive image interferometry'.

Poliannikov et al. (2011) use the concept of inter-source interferometry on some synthetic data to obtain additional information, such as azimuth and distance, that can help with microseismic event localizations.

Among the above-mentioned applications, those that possess higher potential to be applied to microseismic monitoring include surface-wave tomographic inversion for shallow microseismic experiments, extraction of body waves along wellbores for retrieval of velocity information and other subsurface parameters, interferometric event localization, and

coda wave interferometry (or passive image interferometry) for time-lapse purposes. These applications are described in more details in the following.

1.1.3.1 Surface-wave tomographic inversion

One of the most widely used applications of direct-wave interferometry is the retrieval of seismic surface waves between seismometers and the subsequent tomographic determination of the surface-wave velocity distribution of the subsurface. This approach has been pioneered by Campillo and Paul (2003), Shapiro and Campillo (2004), Sabra et al. (2005a), and Sabra et al. (2005b). In fact, for receivers at the surface, seismic interferometry holds the potential to reconstruct surface waves because seismic noise propagates mostly as surface waves in the shallow crust. In other words, surface waves are by far the strongest events in ambient seismic noise.

In layered media, surface waves consist of several propagating modes, of which the fundamental mode is usually the strongest. As long as only the fundamental mode is considered, surface waves can be seen as an approximate solution of a 2D wave equation with a frequency-dependent propagation velocity. So by considering the 2D configuration of Figure 1.5a as a plan view, the analysis above holds for ambient surface-wave noise. The Green's function of the fundamental mode of the direct surface wave can thus be reconstructed from the crosscorrelation of ambient noise records (assumed to be diffuse, or coming from an approximately complete boundary of noise sources) for as many inter-receiver paths as possible within a network of receivers. In other words, each seismometer can be turned into a virtual source, the response of which is observed by all other seismometers. From the resulting cross-correlograms, the surface wave (Rayleigh or Love) group or phase velocities are obtained at different frequencies and used to perform surface wave tomography. As different frequencies are sensitive to seismic velocities at different depths in the Earth (generally higher frequencies oscillate in shallower layers, lower frequencies in deeper layers), it is possible to construct velocity models of the subsurface at a range of depths that depend on the set of frequencies considered. Since in principle this method does not depend on source location but only on the location of the receivers, it is particularly useful in aseismic regions where traditional tomography using teleseismic earthquake sources is not able to provide sufficiently high resolution.

In the case of a spatially homogeneous distribution of noise sources, the crosscorrelation is expected to be nearly symmetric in amplitude and in arrival time with its positive and negative parts corresponding to the Green's function of the medium and its anticausal counterpart, respectively (e.g., Lobkis and Weaver (2001); Van Tiggelen (2003); Snieder (2004); Sánchez-Sesma and Campillo (2006)). In practice, the causal and anticausal parts of the crosscorrelation may strongly differ in amplitude. This amplitude factor depends

directly on the energy flux of the waves traveling from one station to the other (Van Tiggelen, 2003; Paul et al., 2005). In other words, in the case of a perfectly isotropic distribution of sources, the energy flux between two stations is the same in both directions and the resulting crosscorrelation between these stations is symmetric (Figure 1.3). On the other hand, if the density of sources is larger on one side than on the other, the amounts of energy propagating in both directions are different. In this case, the resulting crosscorrelation is no longer symmetric in amplitude, although the arrival time remains the same (Figure 1.6) (Stehly et al., 2006).

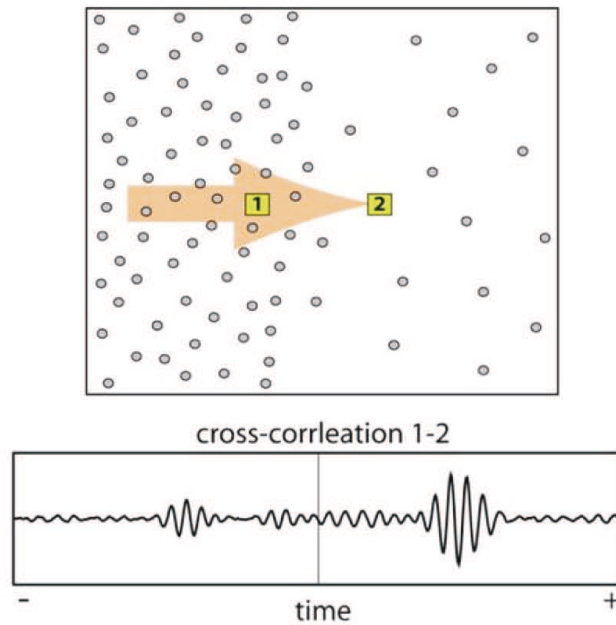


Figure 1.6: Schematic illustration of the effect of inhomogeneous noise source distribution on the degree of symmetry of crosscorrelation. Even distribution of noise sources around the receivers 1 and 2 results in symmetric crosscorrelation (Figure 1.3). Nonisotropic distribution of sources leads to asymmetric crosscorrelation (but symmetric travel times). Taken from Stehly et al. (2006).

Figure 1.7 shows example velocity maps of California produced by Shapiro et al. (2005) and Sabra et al. (2005b) in the frequency band 0.05–0.2 Hz using the correlational method described above, which agreed well with the known regional geology. The results also compare favorably with previous estimates obtained using more conventional and elaborate inversion procedures. Figure 1.7b shows the passive shot record indicating an outward-traveling wave. In this area, the seismic noise is strongly directionally biased, originating from the Pacific Ocean as ocean microseisms. For this reason a one-sided impulse response is obtained from interferometry of the noise (Figure 1.6).

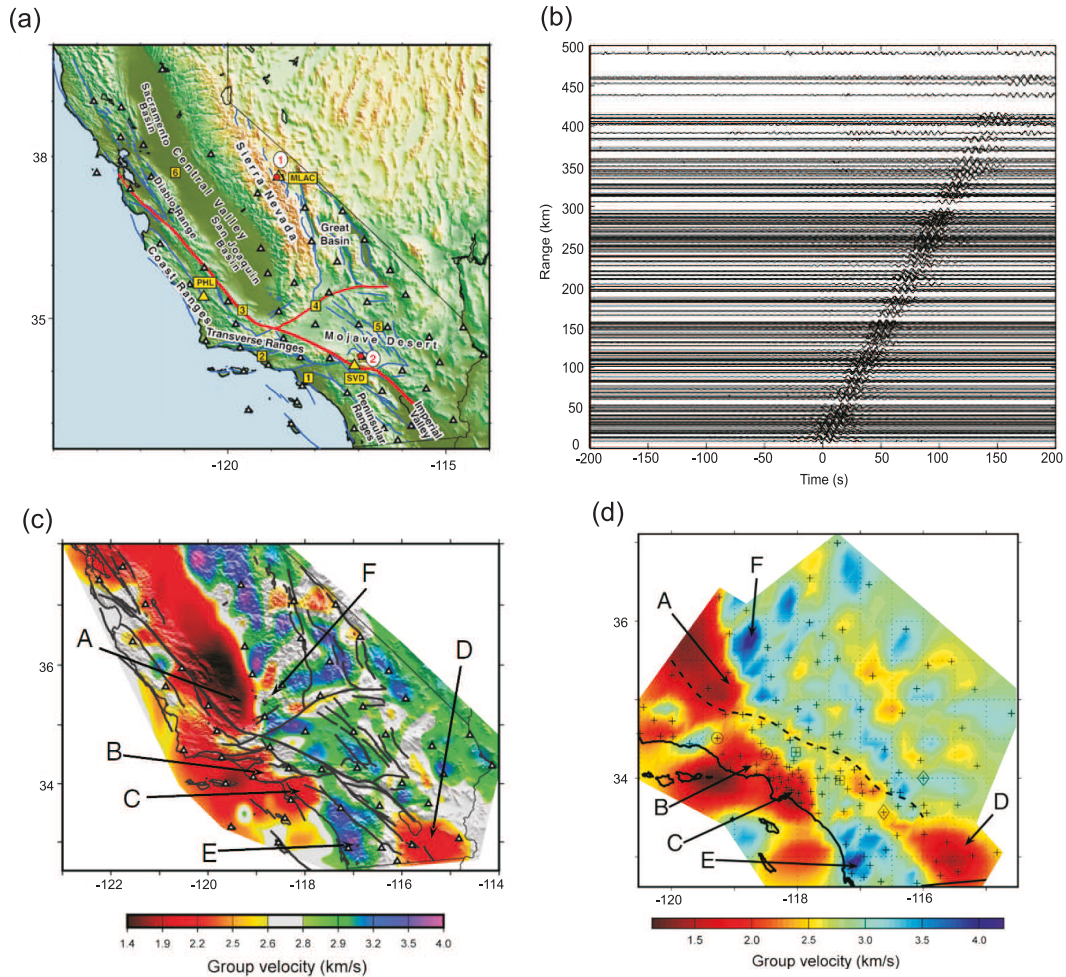


Figure 1.7: (a) Reference map of California. (b) Shot record generated from cross-correlation of one month of the noise. Group-velocity maps obtained from ambient noise tomography by (b) Shapiro et al. (2005) and (c) Sabra et al. (2005b). The numbers and letters denote different geological features in the area. Taken from Shapiro et al. (2005) and Sabra et al. (2005b).

In terms of microseismic monitoring, this application is of particular interest for monitoring in-situ heavy-oil exploitation via steam injection which occurs generally at depths between 400–600m.

1.1.3.2 Extracting P- and S-wave propagation

Using the same principles as in surface-wave tomographic inversion described above, body waves may also be extracted from seismic interferometry of closely spaced receivers (Roux

et al., 2005; Draganov et al., 2007; Gerstoft et al., 2008; Zhang et al., 2010; Ruigrok et al., 2011). Miyazawa et al. (2008) extract direct P- and S-waves from noise crosscorrelation that account for wave propagation between sensors on a vertical array deployed in an observation well for monitoring steam injection into a Canadian heavy-oil reservoir. Figure 1.8a shows the schematic of the facility and an 8-level geophone array in the vertical monitoring well. Figure 1.8b shows two example waveforms at the shallowest and deepest geophones. Although the two signals hardly appear related, correlations between them are hidden in the time series and can be extracted by computing the crosscorrelation. After band-pass filtering, the results of crosscorrelating the noise recorded at the shallowest receiver with that of all the other sensors for the vertical, east-west (E–W), and north-south (N–S) components, give the eight traces shown in Figure 1.8c from top to bottom, respectively, which are related to Green’s functions between the top receiver and each of the other receivers. The crosscorrelation process reveals a pulse that propagates down the array and is visible as the downward propagating wave. The gray lines give the P- and S-wave traveltime curves computed from known properties of the rock. The estimated Green’s functions are strongly one-sided. This is because the noise is predominantly generated at the surface by industrial pumps and other equipment (Figure 1.6).

Therefore, with this analysis, fast high-frequency and slow low-frequency signals propagating vertically from the surface to the bottom were found for the vertical and horizontal components of the wave motion, which are identified with P- and S-waves, respectively. Miyazawa et al. (2008) also found that the fastest S-wave is about 1.9% faster than the slowest S-wave. So, their study demonstrates the useful application of seismic interferometry to field data to determine structural parameters, which are P- and S-wave velocities and a shear-wave-splitting coefficient, with high accuracy.

Similarly, Grechka and Zhao (2012) retrieved body waves and the inferred corresponding formation velocity models nearby the wellbore from correlation of noise records at borehole geophones in different single and crosswell acquisition geometries in microseismic monitoring experiments and for the horizontal and vertical observation wells. Their velocity estimates are comparable to the existing velocity models obtained from well logs.

1.1.3.3 Microseismic event localization

One of the main issues in microseismic monitoring of hydraulically fractured reservoirs is to accurately locate induced microseismic events to monitor propagation and geometry of fractures. The standard location procedures determine the origin time and the coordinates of the hypocenter, and they can be categorized into two types; travel-time-based approach and migration-type approach. The travel-time-based approach originates from the determination of earthquake hypocenter in seismology and it requires the identification of seismic phase and

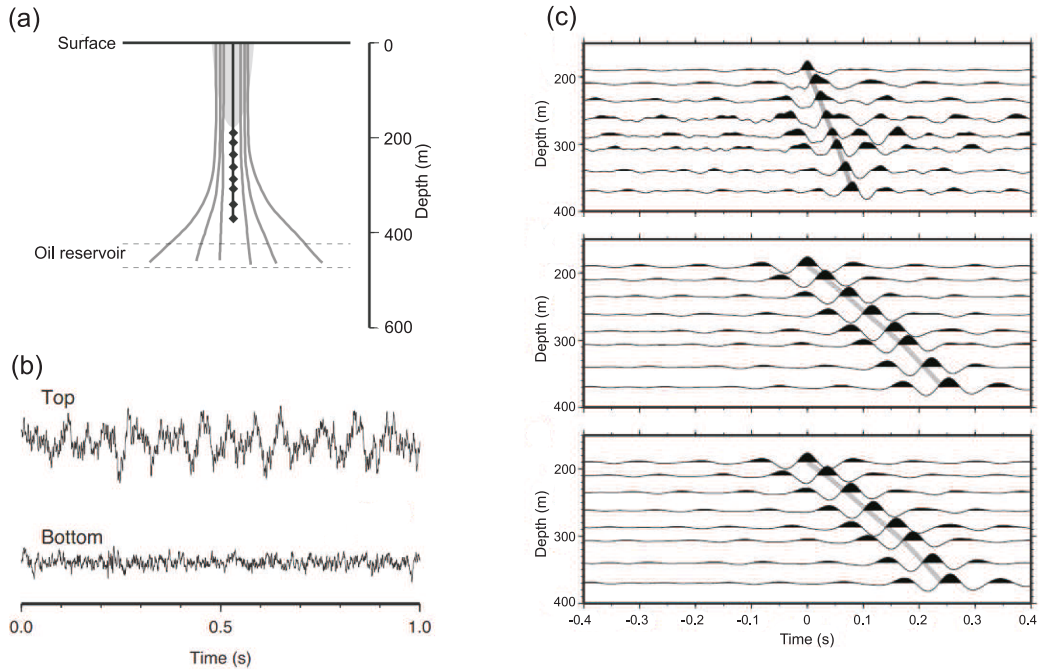


Figure 1.8: (a) Schematic of a heavy-oil production facility in Canada and a vertical array of geophones (black dots) deployed for monitoring the steam injection through a series of underground wells into a layer of heavy oil. Noise (gray) from industrial pumps and other equipment is generated at the surface and recorded along the array. (b) noise waveforms in the vertical component in velocity at the shallowest and deepest sensors. (c) Crosscorrelations between the waveforms at the top sensor and those at other sensors for each component (top) vertical, (middle) E-W, and (bottom) N-S, band-pass filtered from 10 to 55 Hz. A travelttime curve of the downward P-wave reduced by the travelttime at the top sensor is shown by a gray line in top plot; the S-wave is shown in the middle and bottom plots. Taken from Miyazawa et al. (2008).

picking of direct P- and S-wave arrivals. The migration-type approach backward propagates the microseismic energy around a detected/predicted event from all the receivers to the hypocenter and increases the signal-to-noise ratio (SNR) by the number of receivers.

Empirical observations show that small-magnitude microseismic events have higher frequency of occurrence with a logarithmic increase. Those microseismic hypocenters are treated as repeating sources. In surface acquisitions, the key idea of locating microseismicity by seismic interferometry is to first crosscorrelate the direct P- and S-waves from repeating sources in order to transform the original passive seismic data to a virtual source gather. Next, a 'time-difference' migration is applied to the redatumed data (Schuster et al., 2004; Xiao et al., 2006, 2009). With this approach the repeating sources inside a Fresnel

zone give high-SNR arrivals after stacking in a virtual source gather. This gives superiority over traditional microseismic processing to remove noises, reflections, and surface waves in the virtual source gather. Moreover, knowledge of the source excitation time is not needed and more reliability is provided.

When a 1D receiver array is deployed in the monitoring well, the geometry dictates that sources closest to the monitoring well can be imaged better with traditional methods than those further away because the velocity is likely to be better constrained near the observation well, and the receivers form a larger angular coverage relative to the further event locations. So one can suggest that instead of locating events in a more distant fracture independently, we can use available information about the reference (closest) fracture to improve the estimated locations in the more distant fractures. We can use seismic interferometry to couple together events from both fractures.

The principle of inter-receiver interferometry allows physical sources to be redatumed to receiver locations. Receivers can likewise be redatumed to source locations according to the principle of reciprocity, resulting in the idea of inter-source interferometry (Curtis et al., 2009). For a single borehole the full recovery of the Green's function between two source locations is fundamentally impossible. The signal recorded in the well can only be partially redatumed to an event in the first fracture. The end result of the redatuming process is not the complete Green's function, but partial information about it. Poliannikov et al. (2011) show that even with this partial information, the dip angle and radial distances of the sources can still be retrieved by seismic interferometry, although azimuth information is lost.

1.1.3.4 Interferometric time-lapse analysis

For some geophysical applications, such as monitoring of changes in hydrocarbon reservoirs, volcanoes, or fault zones, the major goal is to detect temporal variations in the Earth structure. In addition to surface-wave tomography, passive processing based on seismic-noise (auto) crosscorrelation is of growing interest for the monitoring of temporal changes in complex structures, such as volcanoes or fault zones at the geophysical scale (Sabra et al., 2006; Sens-Schönfelder and Wegler, 2006; Brenguier et al., 2008a, 2011; Hadziioannou et al., 2009).

One of the promising features of seismic interferometry is that it provides us with a snapshot of the Earth's properties at a certain time but it may also potentially reveal continuous changes simply by analyzing noise characteristics recorded using (semi-) permanent receivers. For instance, coda wave interferometry is a technique for inferring time-dependent changes within the medium using acoustic or elastic waves. Seismic waves that

travel through a medium are scattered multiple times by heterogeneities in the medium and generate slowly decaying (late-arriving) wave trains, called coda waves. Despite their noisy and chaotic appearance, coda waves are highly repeatable such that if no change occurs in the medium over time, the waveforms are identical. While the directly arriving phases only sample the medium along the (perhaps virtual) source-receiver path (Figure 1.9a), coda waves have a much longer propagation path due to multiple scattering (Figure 1.9b) and are therefore sensitive to changes within a much larger volume of the medium. Consequently, if a perturbation in the medium (i.e. a bulk variation in velocity, scatterer positions, source location, etc.) occurs over time, it can often be identified by a change in traveltime of the coda waves while this change is undetectable in the first arrivals (Snieder et al., 2002; Snieder and Hagerty, 2004; Snieder, 2006; Grêt et al., 2005, 2006a,b; Pandolfi et al., 2006; Nagaoka et al., 2010; Zhou et al., 2010).

Figure 1.10 shows an example in which two similar artificially-generated events which were recorded a year apart at Merapi Volcano (Galetti and Curtis, 2012) are compared. The same events were also analyzed by Snieder (2003). The waveforms seem to be very similar and match each other at the early times while there appears to be a time shift between them when the later coda are compared. This time shift is a result of changes that occurred within the interior of the volcano. The differences in the waveforms recorded before and after the perturbation can be quantified using the normalized crosscorrelation coefficient $CC(t)$. The correlation coefficient attains its maximum value $CC(t_{max})$ when the correlation time-shift is equal to the average time-shift of the waveforms in the correlation time window considered.

Three types of perturbations that affect the coda include a change in the velocity of the medium, a variation in the scatterers' locations, and the displacement of the source position (Snieder et al., 2002). Each of these perturbation types influences the scattered wavefields in a different way and has a distinct effect on the coda. Velocity perturbations can be identified by a linearly increasing magnitude of the shift in t_{max} ; changes in the scatterers' positions instead cause the maximum crosscorrelation value $CC(t_{max})$ to decrease with time; finally, a variation in the source location only affects the path between the source and the first scatterer, and the maximum crosscorrelation value $CC(t_{max})$ is independent of time. For a constant velocity perturbation δv and fixed scatterer and source locations, the relative velocity change $\delta v/v$ can be obtained from the ratio of the measured time-shift $\langle \tau \rangle$, which gives the maximum crosscorrelation coefficient, and the central time of the considered window t_c :

$$\frac{\delta v}{v} = -\frac{\langle \tau \rangle}{t_c}. \quad (1.10)$$

Coda wave interferometry can be applied to events generated by either earthquake doublets or repeated artificial seismic sources. But the challenge is that repeated artificial seismic

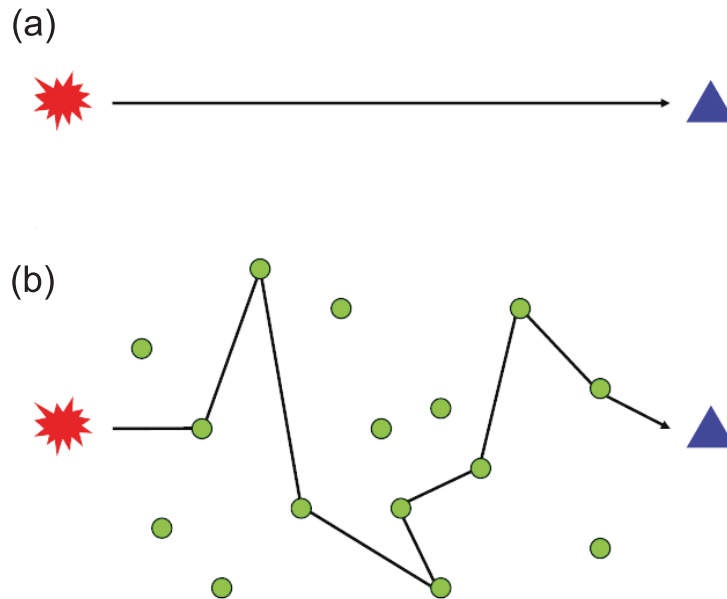


Figure 1.9: (a) the raypath for a direct wave which follows the shortest path between the source and receiver. (b) The raypath for a coda wave, which follows a longer path due to multiple scattering. The red star denotes the source, blue triangle the receiver, and green circles the scatterers. Taken from Galetti and Curtis (2012).

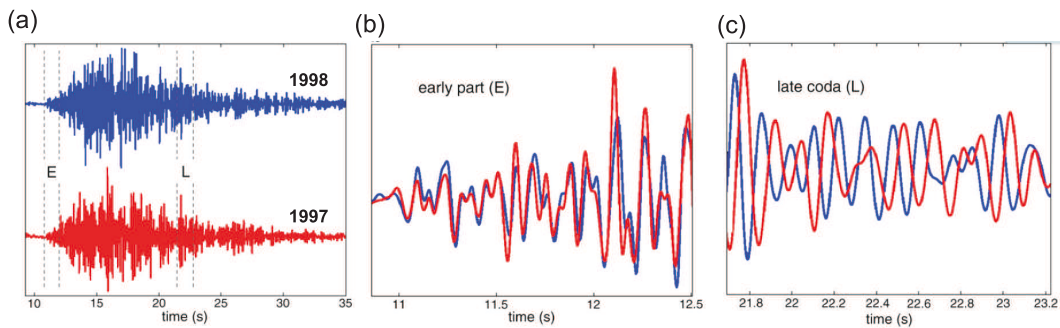


Figure 1.10: Comparison of two waveforms recorded at Merapi volcano in the years 1997 and 1998 for the same source and receiver: (a) complete waveforms; (b) early arrivals; (c) late coda. Taken from Galetti and Curtis (2012).

sources are expensive. On the other hand, repeated earthquakes with almost identical source positions and mechanisms are rare and there is no control on their occurrence. A new approach to overcome these challenges is to combine the methods of seismic interferometry presented in the preceding sections with coda wave interferometry described here, to create a powerful new monitoring methodology. The idea is to replace the use of repetitive sources

by the computation of the seismic-noise correlation function between two sensors. Using this method, the elastic Green's function between two seismometers is constructed as a first step using the crosscorrelation of seismic noise recorded at the two sensors. Then, in a second step, the Green's functions obtained for different times are treated as similar earthquakes and coda wave interferometry is used to extract a temporal variation in seismic velocity. This technique was first introduced by Sens-Schönfelder and Wegler (2006) and is commonly referred to as passive image interferometry. In seismological contexts, these principles have been applied to resolve relative velocity changes between $O(0.01\%)$ and (1%) associated with volcanic activity (Breguier et al., 2008b; Obermann et al., 2013a; Rivet et al., 2014; Duputel et al., 2009), rapid (Wegler and Sens-Schönfelder, 2007; Breguier et al., 2008a; Wegler et al., 2009; Hobiger et al., 2012; Froment et al., 2013) and slow (Rivet et al., 2011) slip on earthquake faults, water content in the shallow crust (Sens-Schönfelder and Wegler, 2006; Meier et al., 2010; Froment et al., 2013; Hillers et al., 2014), thermal processes (Sens-Schönfelder and Larose, 2008; Richter et al., 2014; Hillers et al., 2015a), and tidal-induced deformation (Hillers et al., 2015b).

Acquiring continuous microseismic data (long time period of noise which is required for ambient seismic noise interferometry) in hydraulically fractured reservoirs would allow us to make use of time-lapse interferometry in order to measure the velocities accurately and image subtle changes in the seismic velocity or anisotropy of the reservoir unit (that occur as a result of fluid substitution and/or opening of fractures). This can be done by monitoring the phase shift observed in the retrieved Green's functions. The other possible applications of this method include monitoring changes of density and orientation of fractures in subsurface media from continuous analyses. This can be useful to monitor the reservoir and mitigate potential hazards during production. Further, this could address challenges related to monitoring stress orientation and velocity changes.

1.2 Motivation and contribution

The standard microseismic data analysis involves detecting and locating microseismic events in order to infer information about the fracture geometry and propagation, and the source mechanisms. This information can then be used for obtaining useful reservoir geomechanical properties that are linked with the in-situ stress field, local rock properties, and any existing areas of weakness including faults, fractures, and joints. Altogether, this information is analyzed to understand the subsurface better. However, microseismic events account for only a small percentage of large volumes of typically continuously-recorded microseismic data. The majority of the data consist of complicated seismic coda (the multiply scattered parts of seismic waveforms) and background noise (whatever is recorded when no identifiable

active source is emitting, and which is superimposed on all recorded data). These parts of the data are commonly referred to as 'noise' and mostly filtered out of most analyses. But those parts of seismograms consist of waves that reflect and refract around exactly the same subsurface heterogeneities as waves excited by active sources and microseismic events. Therefore, somewhere within its complex wavefield, ambient seismic noise must also contain similar information about the Earth's subsurface.

Also, monitoring methods applied in reservoir management are mainly based on microseismicity, where properties of induced seismicity can provide estimates of hydraulic rock properties, and local and stress fields, and real-time assessments of seismic hazard. But the problem here is that once the reservoir has matured and percolation networks are established, the induced seismicity greatly decreases, or it stops altogether. On the contrary, passive methods based on ambient noise do not suffer from this as noise is extensively available in time and space.

The key question is how to unravel that subsurface information from these relatively complex-looking waveforms; in other words, how we can turn the noise from a nuisance into signal. Seismic interferometry is a tool that can help us do that.

In this thesis we examine some of the previously-mentioned potential applications of seismic interferometry in microseismic monitoring. During this research we changed tracks to also investigate several other new ideas that can help significantly in the processing and interpretation of microseismic data, including analysis of instrument self-noise, quality assessment of geophone coupling to the wellbore walls, and microseismic event detection.

The main contributions of this thesis can be summarized as:

- analysis of the effect of instrument self-noise in addition to the observation distance on the detectability of microseismic events and seismic interferometry results.
- introducing a new microseismic event detection algorithm based on power spectral density (PSD) estimates of the events compared with that of the background noise.
- proposing a new method for assessment of clamping quality of borehole geophones used in microseismic monitoring.
- investigating the potential of passive image interferometry for time-lapse monitoring of seismic velocities in a wastewater disposal setting.

1.3 Thesis overview

Chapter 2 describes how the instrument self-noise levels that are comparable to or above background noise levels can act as a major constraint for the detection of weak microseismic

events at larger distances, in particular for borehole deployments in quiet deep environments. High instrument self-noise levels also challenge methods such as seismic interferometry which aims at analysis of coherent features in ambient noise wavefields to reveal subsurface structure. This chapter also provides a new criterion for microseismic event detection based on variations of the PSDs in a time-frequency representation, which were initially used for instrument self-noise estimations. Also using a real data example, a preliminary comparison of the proposed event detection algorithm with the common short-time average/long-time average (STA/LTA) method is provided.

Chapter 3 provides a more detailed description of the PSD event-detection method introduced in chapter 2 by comparing its performance with that of the STA/LTA method when applied to a 1-hr long segment of the vertical component of some raw continuous data recorded at a borehole geophone in a hydraulic fracturing experiment. The PSD technique outperforms the STA/LTA technique by detecting a higher number of weak events while keeping the number of false alarms at a reasonable level. Also, the PSD time-frequency representations can also help define a more suitable band-pass filter which is usually required for the STA/LTA method.

Chapter 4 proposes a new interferometric-based approach for assessment of clamping quality of borehole geophones, which suggests that the characteristics of the retrieved cross-correlation functions between a reference receiver and other receivers in an array are indicative of the clamping quality of the former geophone to the borehole wall. The criterion based on which the clamping quality is evaluated is the 'separation frequency' or 'emergence frequency', which is defined as the frequency below which direct body waves propagating along the receiver line are clearly observed on the crosscorrelation gathers. In fact, the clamping issue is introduced as an alternative explanation for the relatively low number of detected microseismic events in the data set investigated in chapter 2, which was postulated to be due to relatively high instrument noise in addition to the distance of the observation well from the individual perforations.

Chapter 5 investigates the possibility of passive monitoring of a wastewater disposal well and its surroundings using continuously-recorded ambient seismic noise, based on the idea of coda wave interferometry and passive image interferometry. We are particularly interested in seismic velocity variations induced by reduction of injection pressure in an effort to mitigate the elevated level of seismicity most likely due to injection of large volumes of waste fluid. Preliminary results show the existence of some relationship between the measured relative velocity variations and the injection pressure, specifically for the optimally positioned station pairs. Hydrologic data and noise energy trends are also investigated, which show no direct impact on the observed velocity variations.

Chapter 6 presents the concluding remarks of this research.

CHAPTER 2

Analysis of instrument self-noise and microseismic event detection using power spectral density estimates¹

Reliability of microseismic interpretations is very much dependent on how robustly microseismic events are detected and picked. Various event detection algorithms are available but detection of weak events is a common challenge. Apart from the event magnitude, hypocentral distance, and background noise level, the instrument self-noise can also act as a major constraint for the detection of weak microseismic events in particular for borehole deployments in quiet environments such as below 1.5–2 km depths. Instrument self-noise levels that are comparable with or above background noise levels may not only complicate detection of weak events at larger distances but also challenge methods such as seismic interferometry which aims at analysis of coherent features in ambient noise wavefields to reveal subsurface structure.

In this article we use PSDs to estimate the instrument self-noise for a borehole data set acquired during a hydraulic fracturing stimulation using modified 4.5-Hz geophones. We analyze temporal changes in recorded noise levels and their time-frequency variations for borehole and surface sensors and conclude that instrument noise is a limiting factor in the borehole setting, impeding successful event detection. Next we suggest that the variations of the spectral powers in a time-frequency representation can be used as a new criterion for event detection. Compared to the common STA/LTA method, our suggested approach requires a similar number of parameters but with more flexibility in their choice. It detects small events with anomalous spectral powers with respect to an estimated background noise

¹A version of this chapter has been published as Vaezi, Y., and van der Baan, M., 2014, Analysis of instrument self-noise and microseismic event detection using power spectral density estimates, *Geophysical Journal International*, **197**(2), 1076–1089, doi: 10.1093/gji/ggu036.

spectrum with the added advantage that no band-pass filtering is required prior to event detection.

2.1 Introduction

Microseismic monitoring involves the acquisition of continuous seismic data for the purpose of locating and characterizing microseismicity induced by hydraulic fracturing due to fluid injection, monitoring resulting reservoir changes, and understanding the associated geomechanical processes in the subsurface. Its wide applications in hydrofracture monitoring, geothermal studies, reservoir surveillance, and monitoring of CO₂ sequestration have turned microseismic monitoring into an invaluable tool (Phillips et al., 2002; Maxwell et al., 2004; Warpinski, 2009; van der Baan et al., 2013). Microseismicity should not be confused with "microseism" which is the term commonly used to describe the strong and continuous peak in the spectra of the Earth noise field dominantly observed in the period range of 4–20 s and is related to ocean waves' interactions (Ewing et al., 1957; Lee, 1935). In this context, we strictly adhere to the term "microseismic event" to describe microearthquakes which are typically known as earthquakes with magnitudes below zero (Maxwell et al., 2010b). Microseismic monitoring differs in many respects from seismic reflection surveys that are traditionally used for oil and gas exploration and development, including the type of sources, receivers, and methods of analysis. Microseismic data are typically broadband (10–1000 Hz) and recorded at high sampling rates with 3C surface and/or borehole receivers. A crucial step in the processing of microseismic data is event detection and time picking that should be done accurately. Any errors in the onset-time picking may be amplified when locating or identifying the events, and performing source mechanism analysis.

Microseismic data are mostly acquired continuously and comprise therefore large volumes. Manual detection is subjective and time consuming. Therefore, an automatic event detection algorithm is required to make this process economic in terms of computation time and effort. There are a great number of trigger algorithms available for onset-time picking that are generally characterized into time domain, frequency domain, particle motion processing, or pattern matching (Withers et al., 1998). All of these algorithms are either based on the amplitude, the envelope, or the power of signals in the time or frequency domains. Although there are more sophisticated trigger methods than the STA/LTA technique (Allen, 1978), they usually require complicated parameter adjustment operations. Therefore, the STA/LTA remains the most popular method in which the ratio of average energy in a short-term window and a long-term window (STA/LTA ratio) is used as a criterion for picking. However, this method has also its own disadvantages. It requires careful setting of parameters (Trnkoczy, 2002) including two window lengths and a SNR threshold. A high

threshold may lead to missing weak events while a low threshold can result in many false triggers.

A common shortcoming among various event detection algorithms is that they are very sensitive to the SNR level so that weak events whose energies and amplitudes are comparable to background noise may not be triggered. In other words, weak events may be obscured in the presence of strong noise. There are many sources of noise. They could be generated either naturally or artificially. The natural sources include oceans, high waterfalls, rivers, lakes, etc., while artificial sources are industrial machinery, railways, highway traffic, buildings, etc. (Nofal et al., 2004).

Another important source of noise other than site noise is instrumental self-noise. Self-noise of an instrument is the noise that is introduced and recorded by the equipment system itself even if there is no external source of noise. Both sensor and the digitizer of a seismograph system have their own self-noise (Ackerley and Spriggs, 2012). Instrument self-noise can act as a major constraint for detection of microseismic events and analysis of ambient seismic noise in quiet environments because these signals can easily be masked in the presence of strong instrument self-noise. Therefore, it is crucial to know the instrument self-noise level before any analysis and interpretation. Lack of a self-noise standard makes it difficult to assess when a sensor's self-noise is above the manufacturers' specifications, indicating a possible problem with the sensor or noisy site conditions (Ringler and Hutt, 2010).

With this in mind, we have studied microseismic data recorded using modified 4.5-Hz geophones deployed in a borehole to monitor a hydraulic fracture treatment over a shale-gas reservoir. These geophones have significantly better noise performance (higher sensitivities and lower minimum magnitude detection threshold) than that of standard 15-Hz sensors. However, we suggest that because the levels of ambient noise, which can be considered as being mostly surface waves, are very low in deep boreholes due to the distance from the surface, a comparatively large instrument self-noise can prevent detection of weak events with negative magnitudes, especially at viewing offsets in excess of 500 m. However, the decay of the surface noise is frequency-dependent (Carter et al., 1991; Stephen et al., 1994) and some frequency bands may still have energies above the instrument self-noise level.

The method used to calculate instrument self-noise is based on PSD estimations. We analyze the temporal changes in recorded noise levels and their time-frequency variations using a modified Welch transform. In order to show the effects of measurement depth and instrument self-noise we compare the calculated PSDs and energy variations of the borehole recordings with those of surface broad-band seismometers in this study. We then describe how this comparison could add to the ongoing discussions about surface versus borehole microseismic monitoring (Maxwell et al., 2012; Eisner et al., 2013). Finally we describe how variations from known background noise levels can be used for semi-automated event detec-

tion without prior knowledge of signal frequency contents. This algorithm is then compared with the typical STA/LTA technique.

2.2 Rolla microseismic experiment

The microseismic data used for this study are from a borehole array consisting of six 3C low-frequency (4.5-Hz) receivers deployed in a slightly deviated (<20 degrees) monitoring well (well E in Figure 2.1) and also from surface 3C broad-band seismometers measured during the Rolla Microseismic Experiment (Eaton et al., 2013). The sampling intervals of the borehole receivers and surface seismometers are 0.5 and 2 ms, respectively. The experiment recorded a multistage (21 stages) hydraulic fracture stimulation of a Montney gas reservoir in northeastern British Columbia, Canada.

The overall layout of field equipment, relative locations of the two treatment wells H_1 and H_2 , a cross-section through the borehole array, and configuration of a broad-band array are shown in Figures 2.1a–d, respectively. The shallowest borehole receiver is located at a true vertical depth of 1668 m with the other receivers positioned at 32 m spacing.

Broad-band sensors are deployed either as part of four mini-arrays consisting of four 3C seismometers (A–D) or as single 3C seismometers (F and G). 10 stages of fracture treatments took place in well H_1 during August 15–18 and 11 stages in well H_2 during August 20–25 in 2011. The broad-band seismograph units recorded data continuously while the downhole toolstring was deployed twice, successfully recording both sets of fracs. Only the borehole recordings and surface recordings at seismometers F and A_3 from the treatments at well H_2 are used for this study.

Perforation shots were fired at 200 m spacing along the horizontal component of the well H_2 and used for velocity model calibration. The true vertical depths of the perforation shots range from 1946 to 1954 m. Source-to-borehole receivers offsets for the perforation shots vary from 756.9 to 2018.8 m which are significantly larger than in typical borehole hydrofracture monitoring. Generally, the maximum distance at which microseismic events can accurately be detected depends on the size of the events, attenuation, and noise level at the monitoring well (Warpinski et al., 2009). However, the viewing distances are typically set to be below 800–1000 m (Maxwell et al., 2010a; Warpinski et al., 2009).

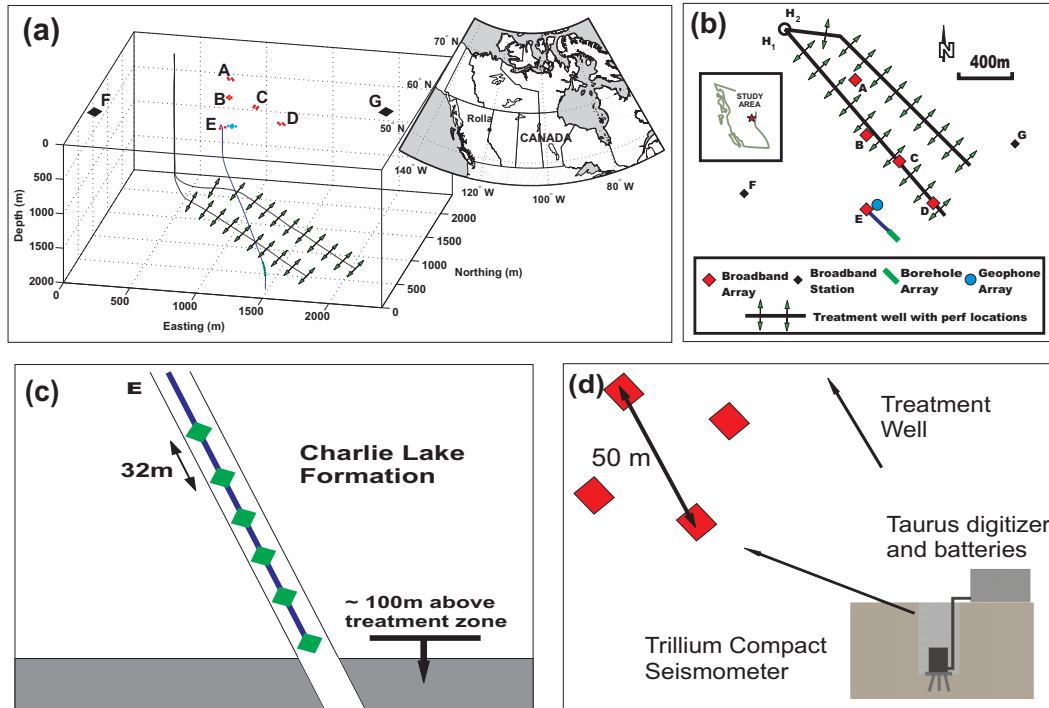


Figure 2.1: (a) 3D view and (b) map view of the acquisition geometry of the Rolla microseismic experiment. Three types of microseismic recording systems were used; a borehole toolstring (E), a set of broad-band seismograph systems deployed within four-station arrays (A, B, C and D) or as individual stations (F and G), and a 12-channel array of geophones located near the borehole system. H_1 and H_2 are the injection wells. (c) Cross section showing borehole toolstring of six 3C geophones (modified after Eaton et al. (2013)). (d) Configuration of surface broad-band seismometers. Each array consists of 4 stations forming a diamond shape pointing at the injection well head.

2.3 Evaluation of energy variations

2.3.1 Observations

A considerable increase in energy levels is anticipated during hydraulic fracture treatments. Energy fluctuations are likely to follow injection strategies with observed seismic energy proportional to fluid injection rates for receivers situated close to the injection wells. Alternatively, energy levels may be in-line with fluctuations in ambient noise levels, e.g., due to anthropogenic activities, if receivers are placed closer to the surface. Figure 2.2a shows the pump curves (treatment pressure, slurry rate, and blender density) for the 4th stage of the fracture treatment. The corresponding time series for the vertical and two horizontal

components in the shallowest borehole receiver are also plotted. The vertical component has higher amplitudes than the horizontal ones. The time series are constructed by combining positive values from high-pass filtered traces (>200 Hz) with negative values from low-pass filtered traces (<50 Hz). Amplitudes of low-pass filtered traces are multiplied by 8 for the purpose of representation. Trace amplitudes do not increase significantly during fluid injection. There is only some correlation between slurry rate and the vertical component amplitudes for frequencies less than 50 Hz. The period jumps in signal strength on the horizontal components are thought to be electronics-related and discarded in our following analyses. The time series at broad-band surface seismometers A₃ and F corresponding to the same hydraulic fracturing stage are also shown in Figures 2.2b and c, respectively. At the surface, the horizontal components have higher amplitudes than the vertical ones. Contrary to the borehole receivers, surface seismometers display various amplitude increases associated with fluid injection.

In Figure 2.3a, temporal variations in recorded energy are plotted for all three components of the shallowest borehole receiver. The energies are computed for individual 20-min long windows of data overlapping by 50% and attributed to the time at the center of the windows. Energies are displayed on a logarithmic scale. The blue dashed line represents the time when the 4th stage of treatment takes place. The red dashed lines identify the times of all other treatment stages. No significant energy variations are observed over the entire measurement period. Furthermore, there is no noticeable energy increase corresponding to treatment times except for stage 1. For comparison, the temporal energy variations are also computed for surface broad-band seismometers A₃ and F and displayed in Figures 2.3b and c, respectively. As expected, the background noise energy levels are much higher on surface records than on the borehole receivers. On the other hand, more energy variations are observed at the surface during the recording time. Figure 2.3d shows the recorded energies at seismometer F for corresponding time series high-passed above 0.7 Hz. The diurnal energy variations are now much more evident than in Figure 2.3c meaning that frequencies below 0.7 are contributing predominantly to the total energy in Figure 2.3c.

2.3.2 Interpretation

Generally, when recording the ambient background noise for a long period of time (days or more), a diurnal energy trend is observed with higher energy at daytime than night time (Bonnetoy-Claudet et al., 2006). Figure 2.3a shows no diurnal energy variations or any kind of periodicity in the recorded energy but an essentially constant level. This is the case for all other borehole receivers too.

Ambient noise, which is considered as mostly comprised of surface waves, becomes weaker with depth (Carter et al., 1991; Stephen et al., 1994) due to diminishing noise sources,

e.g., anthropogenic noise is predominantly generated at the surface. This fact can also be inferred from comparing energy levels at surface seismometers and borehole receivers displayed in Figure 2.3. The rate of decay in ambient noise level with depth is site and frequency dependent. Generally reduction in noise amplitudes at high frequencies is much higher than for low frequencies. For instance, Carter et al. (1991) have reported that noise levels in their study area between 15 and 40 Hz are more than 10 dB less at 945 m depth than at the surface, and from 40 to 100 Hz the difference is more than 20 dB. The lack of any diurnal energy trend in our borehole data set can be attributed therefore to the depth of the experiment (1668–1828 m). The observation of diurnal energy variations at surface (Figure 2.3) favors this idea. However, the depth cannot justify lack of energy bursts caused by injection of large volumes of fluids in the borehole recordings. Furthermore, if depth was the sole reason, no energy increase associated with fluid injection should have been observed for the surface recordings either, which is not the case as shown in Figures 2.2b and c.

Constant noise levels for borehole sensors, however, can be justified assuming the background noise level is below the instrument self-noise. In addition, lack of correlation between variations in recorded energy and treatment times, except possibly for the first and closest stage, can also be justified if instrument self-noise averaged over all frequencies overwhelms the coherent signals emitted during hydraulic fracturing due to the distance of the injection well H₂ from the observation well (Figure 2.1). The source of instrument noise can be either thermal noise in the geophone itself, Johnson noise, voltage, and current noise in the preamplifier, or digitizer noise (Riedesel et al., 1990). Obviously the large time window (20 min) implies that individual microseismic events are less likely to dominate average energy computations, as individual coherent events including perforation shots have been recorded. Likewise, the energy of low-pass filtered recordings shows a clearer correlation with the injection rates (Figure 2.2a). Therefore individual frequency bands may still contain coherent energy above the instrument self-noise level in this experiment. Nonetheless, a clear understanding of instrument self-noise levels is an important factor in microseismic analyses.

2.4 Instrument self-noise estimation

In the previous section we described how self-noise of the recording instrument obscures background noise and also signal and noise energy variations for deep deployments more than 700 m away from the injection stages and may consequently complicate the interpretability of data. It may bury small microseismic events rendering their detection and make time picking challenging. Only strong events whose energies are above the self-noise can then easily be detected. In this section, we analyze the recorded energy levels as a function of

frequency.

2.4.1 Method

The different methods available to estimate self-noise of sensors make side-by-side comparisons of their performance difficult (Hutt et al., 2009). We use PSD estimates to obtain the self-noise assuming a stationary background noise. Calculating the noise PSD is a common method for quantifying seismic background noise. We compute the average PSDs of the entire data for each component and consider them as the upper bound of the instrument noise floor. Power spectra are computed using the Fourier transform and a modified Welch method (Welch, 1967) as outlined by McNamara and Buland (2004) using Hanning window tapers of 20-s and 400-s length for borehole sensors and surface seismometers, respectively, with 50% overlap. By removing the energetic events, transients, and any types of noise bursts, we consider only the noise at quiet times to calculate the PSDs (Peterson, 1993). The calculated individual PSDs are transformed into dB and averaged over the number of windows to obtain the average PSD for each component. The 1st, 5th, 25th, 50th, 75th, 95th, and 99th percentiles (Berger et al., 2004) are also calculated for the transformed PSDs to provide a better understanding of their statistical variations at different frequencies and more insight in stationary (or non-stationary) constituents of the ambient noise field. Moreover, the percentiles can be used to estimate the probability of detecting a microseismic event (Goertz et al., 2012).

2.4.2 Results

The estimated average and percentile PSDs for all three components of the first and the fifth borehole sensors (counted from the top) and surface broad-band seismometers A_3 and F are shown in Figures 2.4 and 2.5, respectively. The Peterson's high noise model (HNM) and low noise model (LNM) (Peterson, 1993) have been plotted for comparison. In Figure 2.4, the blue dashed line represents the self-noise model of a conventional 15-Hz sensor while the green-dashed line represents the manufacturer's self-noise model for the 4.5-Hz instruments used in this study (Goertz et al., 2011). The manufacturer's self-noise model for the broad-band seismometers are plotted as blue dashed lines in Figure 2.5. The subtle peaks in all spectra at frequency of 0.2–0.3 Hz represents the ocean microseism generated primarily by the wave-wave interaction beneath storms over the ocean (Ewing et al., 1957; Lee, 1935).

The modified borehole instruments in this experiment have higher sensitivity and lower detection thresholds than the common 15-Hz sensors, with sensitivities close to the Peterson's low-noise model for surface recordings. Since the averaged PSDs have been computed

for quiet times, we consider them as the detection threshold at each receiver. The flat PSD curve bottoms in the interval of 30–200 Hz in Figure 2.4 suggest that the detection threshold in this frequency range may have been reached, especially for receiver 5, and the instrument self-noise could be what is recorded dominantly. This threshold is around -195 dB. This is somewhat higher than the published instrument self-noise level (green line) but still significantly better than a 15-Hz geophone (blue line). Nonetheless, any event without significant energy beyond this threshold will be difficult to detect on the recordings. This will be explored in more details in the next section.

Comparing the statistical distribution of percentile curves at different frequencies in Figure 2.4 shows that their shapes vary only slightly, justifying the assumption of a stationary background noise model. Comparing Figure 2.4 and Figure 2.5 shows that background noise levels are much higher at the surface by 30–40 dB at 10 Hz, and exceed the instrument self-noise level at all frequencies below 30 Hz. The surface PSD curves closely follow the trends of the Peterson’s noise models and nearly all percentiles are contained within the high- and low-noise platforms. Surface PSD percentile curves display a larger variety of shapes and span a larger magnitude range than the corresponding borehole PSD curves. This implies a larger noise variability at the surface, and may also be indicative of a larger degree of nonstationarity in the surface noise.

To check if the frequency plateau between 30 and 200 Hz in Figure 2.4 is indeed close to the self-noise level of the borehole instruments, we compute averaged time-frequency spectrograms in a similar way as before. Figure 2.6a shows the variation of PSDs over time for the vertical component of the shallowest borehole receiver. The PSDs are averaged for each hour of recording and plotted versus time in this figure. The color bar specifies the power values. Figure 2.6b zooms in on the frequency range of 30–200 Hz. No significant changes in the power levels are visible except between 1 and 15 Hz. The latter have a diurnal time period and are likely related to anthropogenic or ambient noise from the surface. The absence of significant energy fluctuations for all other frequencies confirms our hypothesis that the plateau is indeed indicative of the instrument self-noise level. For comparison purpose, the averaged time-frequency spectrograms for surface seismometers A₃ and F are displayed in Figures 2.7a and b, respectively. The diurnal energy variations are evident in these figures for most of the frequency bandwidth as opposed to Figure 2.6a.

2.4.3 Implications

The minimum magnitude detection threshold increases with distance from the observation well (Figure 2.8a). One view is that this is due to attenuation of signal energy with increasing distance combined with high ambient noise levels. Ambient noise levels decrease, however,

with depth. Therefore in deep wells, the instrument noise level may well be the limiting factor for event detection. Figure 2.8a also shows that the minimum detection threshold for a 4.5-Hz sensor (blue curve) is 0.5 magnitude unit improved with respect to that of the 15-Hz seismometer (red curve). Figures 2.8b and c show source spectra for 5 events of different magnitudes between -3 and -1 at 0.5 magnitude steps for source-receiver distances of 200 and 1200 m, respectively, together with the manufacturer’s self-noise estimates of the used tool, a standard 15-Hz tool, and the Peterson’s reference noise models (Goertz et al., 2012). A quality factor of 150, a generic stress drop of 1 MPa, and shear velocities of 3400 m/s at the source and 3060 m/s at the receiver are assumed (Goertz et al., 2011). For a source-receiver distance as large as 1200 m, the detection threshold of the modified 4.5-Hz geophones is approximately $MW = -1.5$, about 1/2 magnitude unit better than a conventional tool. This can be translated into detection of nearly 3 times more events (Goertz et al., 2011).

In the Rolla microseismic experiment we are dealing with distances to the perforation shots in excess of 700 m for well H₂ (Figure 2.1), thereby significantly reducing the minimum anticipated magnitude detection threshold. Nonetheless, a reduced instrument self-noise level in this quiet environment clearly allows for reduction of the magnitude detection thresholds with distance (Figure 2.8). Therefore we might be able to reduce magnitude detection thresholds with distance (Figures 2.8a and b). This may lead not only to more useful events but also aids in multi-well recordings where many events are solely detected on a single well.

Our observations also have implications for ambient noise tomography using seismic interferometry in order to obtain a velocity model and reveal the subsurface structure nearby the wellbore (Miyazawa et al., 2008; Grechka and Zhao, 2012). This method aims at recovering the Green’s function between two receivers by crosscorrelating passive seismic recordings, thereby emphasizing coherent features in an apparently random ambient noise field. After removing the mean and dc trend from 1-hr long data windows from borehole recordings, the data are fragmented into individual 15-s segments. In order to calculate the average crosscorrelation functions between the shallowest receiver and each of the other receivers the signs (1-bit form) of corresponding individual pre-whitened segments are correlated and then stacked (Bensen et al., 2007; Larose et al., 2004).

Figure 2.9a demonstrates the obtained result for the vertical component after applying a band-pass filter with corner frequencies of [180, 200, 400, 440] Hz. It is related to a causal coherent signal traveling from the shallowest receiver, acting as a virtual source (Bakulin and Calvert, 2004), down the array to the deepest receiver. The moveout velocity of about 1500 m/s calculated from the red dashed line suggests that these high amplitude features are actually related to tube waves propagating within the fluid and along the wellbore. Unfortunately tube waves hold little information about the subsurface beyond the immediate

borehole vicinity and are therefore less useful for analyzing, for instance, temporal variations in the Earth due to fluid injection.

Figure 2.6a, however, shows some diurnal variations in the recorded powers at the low frequency range of 1–15 Hz. Figure 2.9b shows the crosscorrelation functions for this frequency range. A best-fitting line through the maximum correlation values shows an apparent velocity of 6200 m/s. Based on the sonic velocity log shown in Figure 2.9c, these waveforms can be attributed to a high-amplitude low-frequency P-wave originated from the surface and traveling down the borehole array. This P-wave may have been caused by either a low-frequency noise source at the surface or conversion of anthropogenic surface waves to waves traveling along the borehole. At first sight the recovered P-wave moveout seems high. The Charlie Lake formation (where the borehole sensors are sitting) is however composed of large bodies of anhydrites, limestone, and dolomite which can increase the P-wave velocities quite significantly (Edwards et al., 2012).

We suggest that the inability to recover the weaker coherent signals corresponding to P- and S-waves along the borehole is due to the relatively high level of instrument self-noise with respect to the background noise. Therefore, analysis of coherent ambient noise using seismic interferometry can be challenged by dominant instrument self-noise in deep environments.

2.5 A new method for microseismic event detection and time picking

Our PSD analysis method can also be used as an event detection algorithm by computing the average PSD for the entire record and the standard deviations for the individual frequencies. Any short time segments with a PSD that is statistically larger than the average PSD by some likelihood threshold is then a potential event. This method can also indicate which individual frequency bands are statistically above the average threshold. This may be useful in determining suitable band-pass filters.

An example is shown below to demonstrate our proposed detection algorithm. The inset in Figure 2.10 displays 4 microseismic events (B_1 , B_2 , B_3 and B_4) appearing at short time intervals right after the fourth treatment stage at the shallowest borehole receiver. This figure also shows the computed average PSD and its standard deviations at each frequency, as well as the PSDs for the four microseismic events and two noise recordings. A window length of 0.25 s is chosen so that sufficient temporal and spectral resolutions in the time-frequency representations are provided. All event PSDs exceed the average PSD, especially at the frequency range of 25–430 Hz. Also the PSDs of two segments just before event B_1

and after event B₄, which consist of background noise only, have been plotted (dashed lines in Figure 2.10) to show that the noise PSD lies mostly within one standard deviation.

In the next step, a rolling window of length 0.25 s is used and the PSD is computed for each segment throughout the data. The average PSD is then subtracted from all individual PSDs:

$$misfit_t(f) = PSD_t^i(f) - \overline{PSD}(f), \quad (2.1)$$

where $misfit_t(f)$ stands for the PSD difference at each time t as a function of frequency f , $PSD_t^i(f)$ denotes the individual PSD at the corresponding time, and $\overline{PSD}(f)$ is the calculated average PSD. These differences are then divided by the standard deviations at each frequency as following:

$$y_t(f) = \frac{misfit_t(f)}{std(f)}, \quad (2.2)$$

where $std(f)$ is the standard deviation at frequency f Hz. The resulting time-frequency representation highlights then all signals that stand out in a statistical sense from the reference spectrum, in this case the background noise.

Figure 2.11a displays the results $y_t(f)$ in the neighborhoods of the events B₁–B₄. The events can easily be detected as they correspond to anomalous high values over specific frequency ranges. As microseismic events are expected to be of greater powers than the background noise and most of the background noise lies within 1–2 standard deviations, only the values greater than 1 standard deviation at each frequency are kept (Figure 2.11b). This figure shows that the frequency band over which the events are significantly dominant with respect to the noise is 25–430 Hz. This can help in designing suitable band-pass filters in order to better identify and analyze microseismic events.

Events B₁ to B₄ have PSDs that are larger by 2–6 times the standard deviation of the noise model within this frequency range. Assuming a Gaussian probability distribution, this quantifies to probabilities only from 2.27% to less than 0.01% that these are due to random noise fluctuations. In order to make the onset-time picking of the events easier, the calculated quantities in Figure 2.11b are summed over all frequencies:

$$Y(t) = \sum_{f=0}^{f_{Nyq}} y_t(f), \quad (2.3)$$

where $Y(t)$ is the sum as a function of time and f_{Nyq} represents the Nyquist frequency. The result in Figure 2.11c shows how microseismic events stand out of the noise at the

corresponding arrival times.

For comparison, Figure 2.11d shows the result of the STA/LTA method considering a short and a long window length of 15 and 150 ms, respectively. By setting a STA/LTA ratio threshold equal to 4 one can easily detect the events at similar times as our technique. Choosing shorter window lengths has provided a better time resolution for the STA/LTA method than our suggested method. Nonetheless, the PSD method can easily detect the presence of the coherent signals, even if the exact frequency bandwidth of the original signals is *a priori* unknown. The STA/LTA method on the other hand can more easily detect the onset of the various signals, thereby better distinguishing between arrivals B_2 and B_3 (Figure 2.10) but at the expense of more variations in the STA/LTA output levels even if no signals are present (Figure 2.11d).

2.6 Discussions

Event detection and automatic time picking is a very important step in the processing of microseismic data. The accuracy of the event location, event identification, and source mechanism analysis is very much dependent on data quality. Instrument self-noise in quiet environments or consistently high ambient noise levels can complicate event picking using the STA/LTA method. In such environments weak microseismic events will be obscured in the presence of relatively higher instrument self-noise. Therefore, compared with shallow studies, we suggest that deep borehole microseismic acquisitions require sensors of higher sensitivity and lower self-noise to be installed at offsets in excess of 1 km from the treatment area to reduce the minimum magnitude detection threshold. This will increase the probability of detecting a greater number of microseismic events and consequently more detailed interpretations.

Other than strong instrument self-noise relative to the ambient noise level, bad coupling of the borehole instruments to the well could also explain the observations for the borehole data set in the Rolla microseismic experiment. If the sensors are not well clamped to the wellbore they may mostly record the instrument self-noise. Therefore, weak events are unlikely to be detected. Although surface recordings may not suffer from instrument self-noise as much as borehole experiments do, they are more affected by high levels of surface noise so that detection of weak microseismic events at the surface might be cumbersome. Waveform stacking (Özbek et al., 2013; Shemeta et al., 2009) can be an alternative for improving the event amplitudes with respect to the ambient noise but does rely on the recorded signal amplitudes exceeding the instrument self-noise level. In other words, stacking can only retrieve weak signals if their arrivals are aligned, their waveforms are consistent, and the individual signals amplitudes are masked by ambient instead of instrument noise. Signal

amplitudes below the instrument noise level are less likely to be retrieved using stacking, as instrument noise can act more as an amplitude threshold breaking the assumption of linear superposition of signal and noise required for eliminating random noise by summation. On the other hand, waveform stacking can reduce the effect of ambient noise since the recording is comprised of a linear superposition of ambient noise and desired signal, as long as both are contained within the dynamic range of the acquisition system.

This has important implications for borehole versus surface acquisition of microseismicity. Acquisition at the surface is significantly more cost effective and allows for deployment of hundreds to thousands of receivers; yet it has the disadvantage that the propagation distances from the microseismic events to the receivers are much larger, greatly reducing the number of easily detected events. Borehole deployments are significantly more expensive, generally use two to three orders less instruments but allow for detection of many more events. The larger number of surface receivers may allow for improved ambient noise reduction; yet both acquisition strategies may be limited by their instrument sensitivity, in particular if conventional 15-Hz geophones are used, and event locations are more than 1 km away from the receivers (Figure 2.8).

Compared with the STA/LTA algorithm, our suggested event detection method uses a similar number of parameters, namely a detection threshold and a sliding window of pre-specified length. As the PSD technique is based on the time-frequency representations, the window size should be chosen such that it trades-off between temporal and spectral resolutions. The window length should be small enough to make closely spaced events distinguishable and large enough to allow long-period components to be adequately accounted for in the analysis. The PSD method is devised to be insensitive to variations in signal frequency content. Conversely, it does assume constant background noise levels. It can also be used to design a more suitable band-pass filter for further analysis of microseismic data whereas the STA/LTA method usually requires the data to be band-passed prior to event detection.

However, it should be noted that onset-time picking and event detection are two different concepts. The former includes specifying the exact arrival time of the event whereas the latter implies only the presence of events. When the parameters are best set, the STA/LTA technique seems to better determine the onset times while the PSD method works best in identifying the presence of an event. We suggest that the PSD method would relatively do better in detection of emerging events where the gradual amplitude increase can make the STA/LTA method fail.

2.7 Conclusions

Considering the depth of the receivers, observation of very small to absent energy variations during the fracture treatments and fluid injections, lack of diurnal energy trend, and a constant energy level throughout the borehole data suggest that the self-noise of the instruments is a major limiting factor in deep microseismic experiments. The averaged and time-varying PSDs show that the instrument noise floors are being reached in this data set especially at the frequency interval of 30–200 Hz. In quiet environments, instrument self-noise may thus be the limiting factor determining the magnitude-distance detection threshold. It can also make the analysis of ambient noise using seismic interferometry challenging.

Conversely, surface recordings show more energy variability in seismic background noise and higher power levels. The use of a large number of instruments at the surface allows also for a greater reduction in ambient noise by waveform stacking, if the waveforms are consistent across the array, individual arrivals can be aligned, and signal strengths exceed the instrument noise level. Therefore, a clear understanding of instrument self-noise levels is an important parameter in microseismic analyses for both borehole and surface deployments.

Knowledge of the instrument self-noise and the ambient noise level can also aid in event detection, since it permits to extract signals that are statistically different from the background PSD at individual frequencies. This has the advantage over the STA/LTA method that no prior band-pass filtering is required to enhance the SNR and also permits for detection of signals with characteristically different frequency contents if the background noise spectrum is stationary.

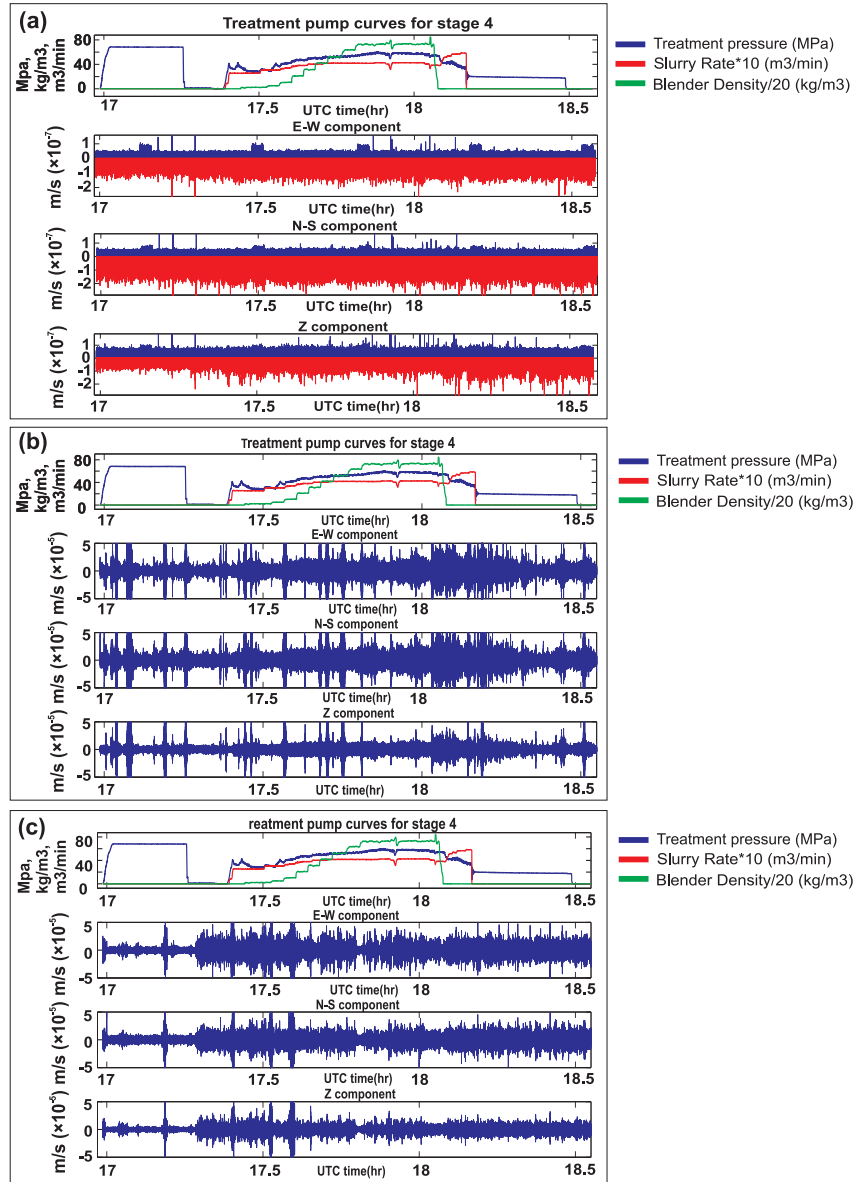


Figure 2.2: (a) The pump curves for proppant (green), slurry (red), and pressure (blue) rates for the 4th stage of the treatment in well H₂ along with the corresponding vertical and two horizontal component recordings at the shallowest receiver, respectively. Positive values represent high-passed filtered trace (>200 Hz) while negative values show low-pass filtered traces (<50 Hz). Time axis is in Universal time (UTC). No significant energy increase corresponding to treatment time is observed, except for the low-frequency part of the vertical component. (b) and (c) The pump curves for the 4th treatment stage along with the corresponding horizontal and vertical component time series at the surface seismometers A₃ and F, respectively. The recorded energy increases during the treatment times.

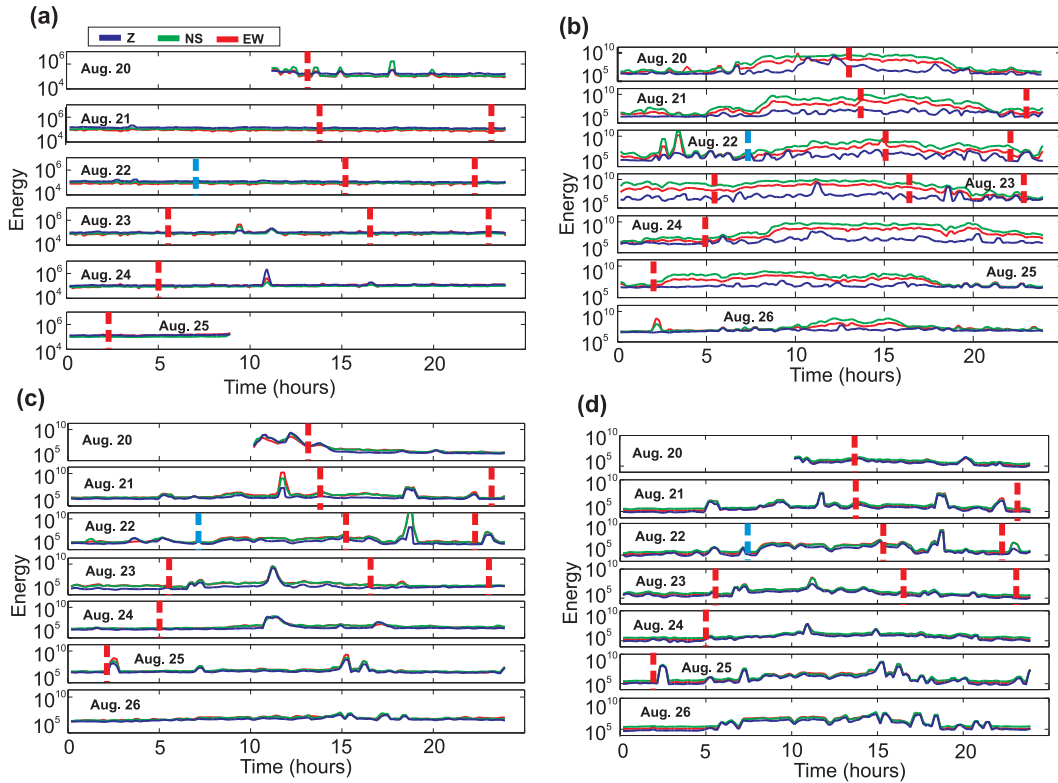


Figure 2.3: (a) Energy variations over the entire treatment period at well H_2 for the shallowest borehole receiver. Red, green, and blue correspond to the E-W, N-S, and vertical (Z) components, respectively. Blue dashed line denotes the time at which the 4th treatment stage starts and red dashed lines show the start time of all the other stages. Recorded energy is mostly constant and shows little to no correlation with injection times nor any diurnal variations. (b) and (c) The same for surface seismometers A_3 and F , respectively. Energy variations associated with diurnal energy variations plus treatments are observed, especially for A_3 . (d) Similar to (c) but for time series high-passed above 0.7 Hz. The energy variations are more evident.

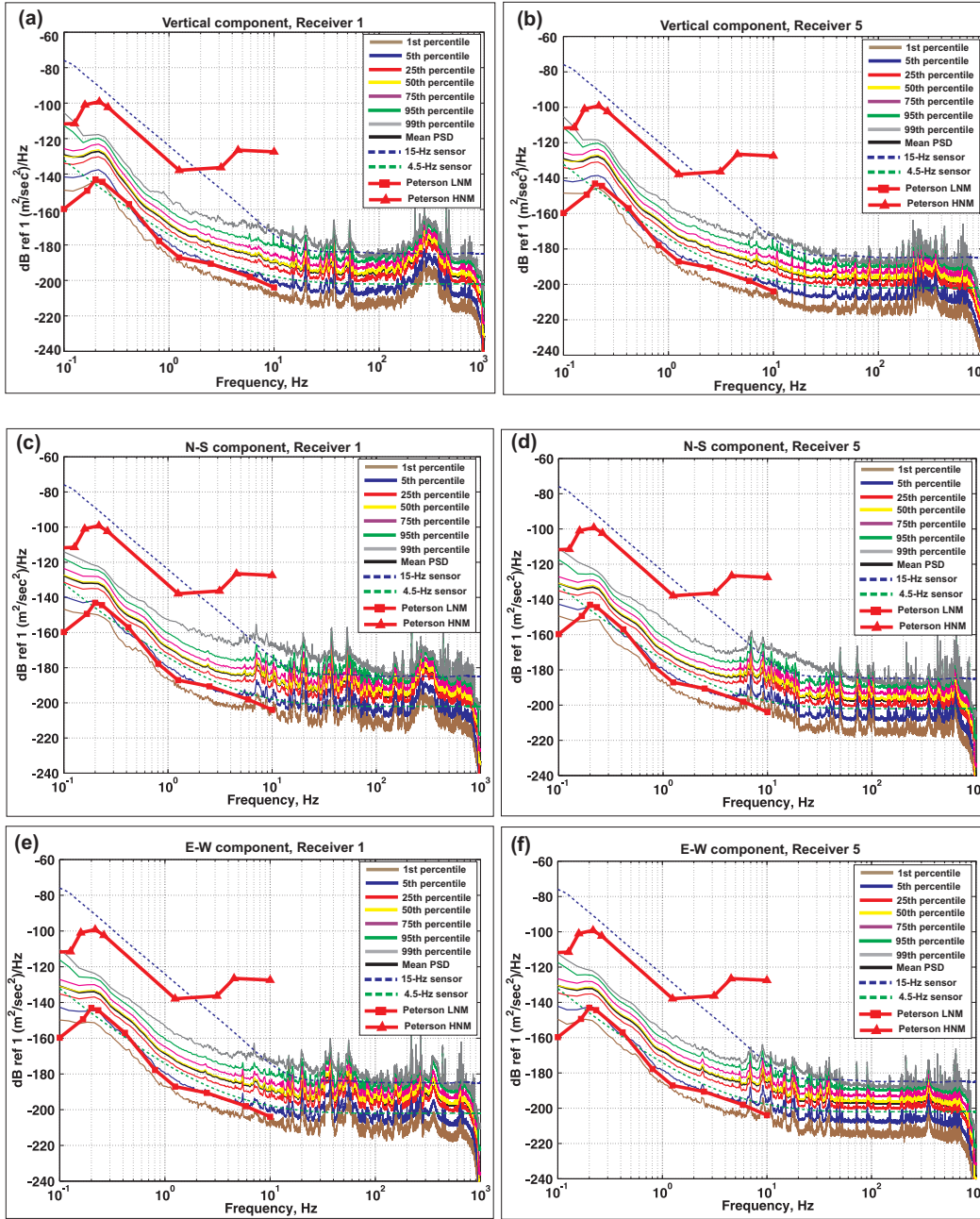


Figure 2.4: (a), (c) and (e) The average PSD plus 1st, 5th, 25th, 50th, 75th, 95th, and 99th PSD percentile estimates for the vertical and two horizontal components at borehole receiver 1 (counted from the top), respectively, as a function of frequency. (b), (d) and (f) The same for receiver 5. The solid black curves demonstrate estimated average PSD. Upper and lower red curves show Peterson’s low noise and high noise models, respectively (Peterson, 1993). The blue dashed line represents the self-noise model of a conventional 15-Hz sensor while the green-dashed line represents the manufacturer’s self-noise model for the 4.5-Hz instruments used in this study. Estimated PSDs are above the manufacturer’s specification but lower than for a 15-Hz geophone.

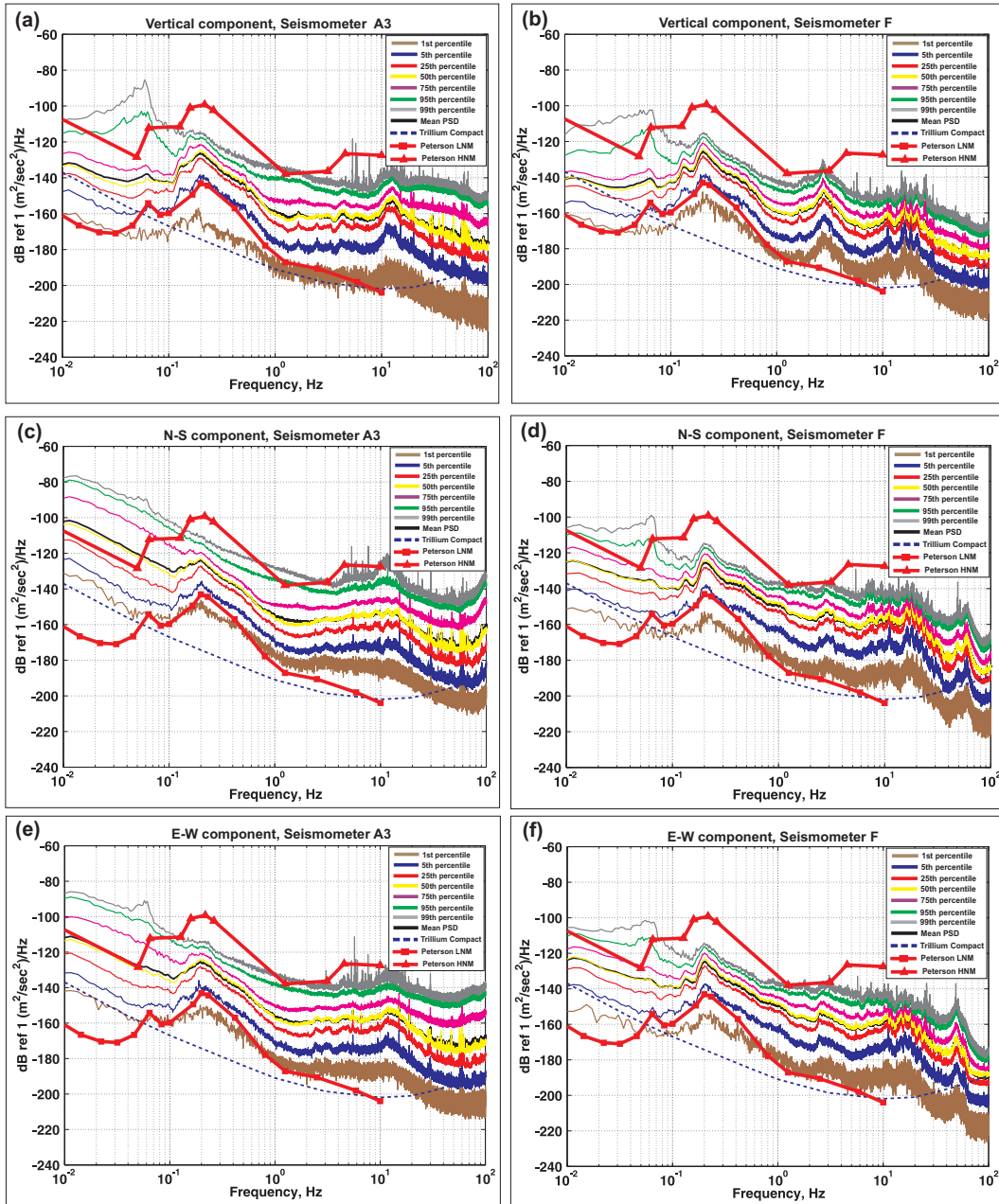


Figure 2.5: (a), (c) and (e) The average PSD plus 1st, 5th, 25th, 50th, 75th, 95th, and 99th PSD percentile estimates for the vertical and two horizontal components at surface seismometers A_3 , respectively, as a function of frequency. (b), (d) and (f) The same for seismometer F. The solid black curves demonstrate estimated average PSD. Upper and lower red curves show Peterson’s low noise and high noise models, respectively (Peterson, 1993). The blue dashed line represents the self-noise model of the seismometers. The noise power levels are well above the estimated self-noise model and also higher than in borehole receivers.

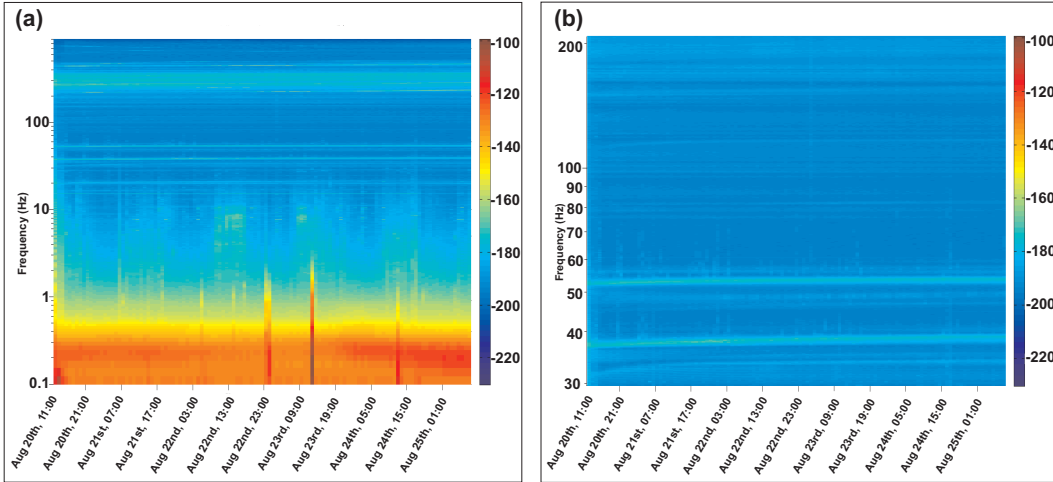


Figure 2.6: (a) The time-frequency representation of PSD variations for the vertical component of the shallowest borehole receiver. (b) Zoom in for the frequency range of 30–200 Hz only. Energy levels are approximately constant except possibly between 1 and 15 Hz.

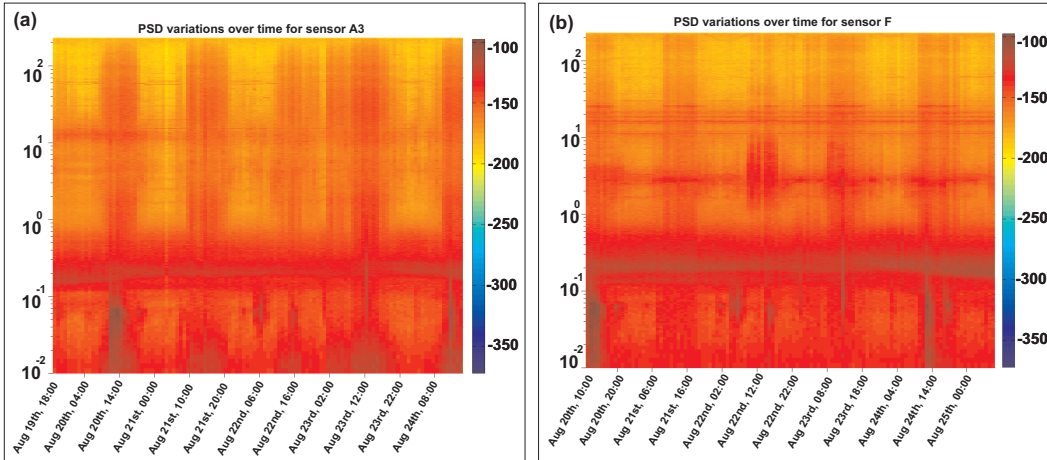


Figure 2.7: (a) and (b) The time-frequency representation of PSD variations for the vertical component of the surface seismometers A_3 and F, respectively. The diurnal energy variations exist in most of the bandwidth.

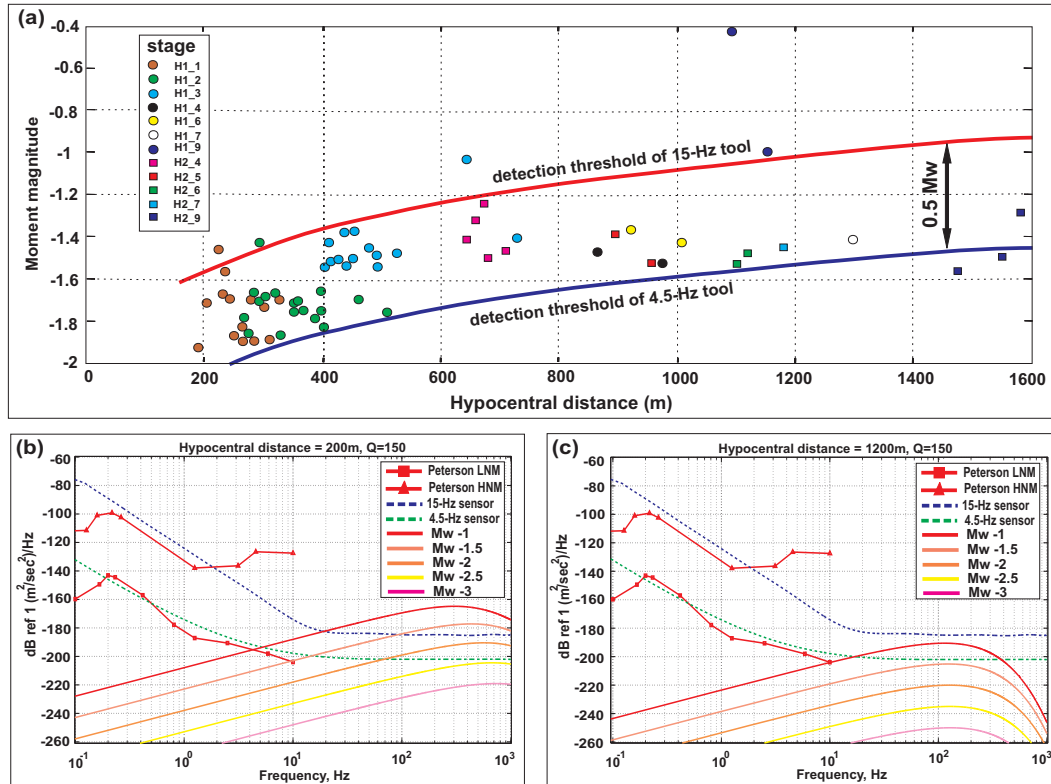


Figure 2.8: (a) Minimum magnitude detection threshold increases with distance from the observation well. Sensitive tools can lower the threshold leading to detection of more weak events (modified after Eaton et al. (2013); Goertz et al., personal communication, 2012). (b) and (c) Source spectra for events of different magnitudes for source-receiver distance of 200 and 1200 m, respectively, assuming $Q = 150$. Contrary to the 15-Hz geophones, the 4.5-Hz receivers can still detect events of magnitude around -1.5 for the distance of 1200 m.

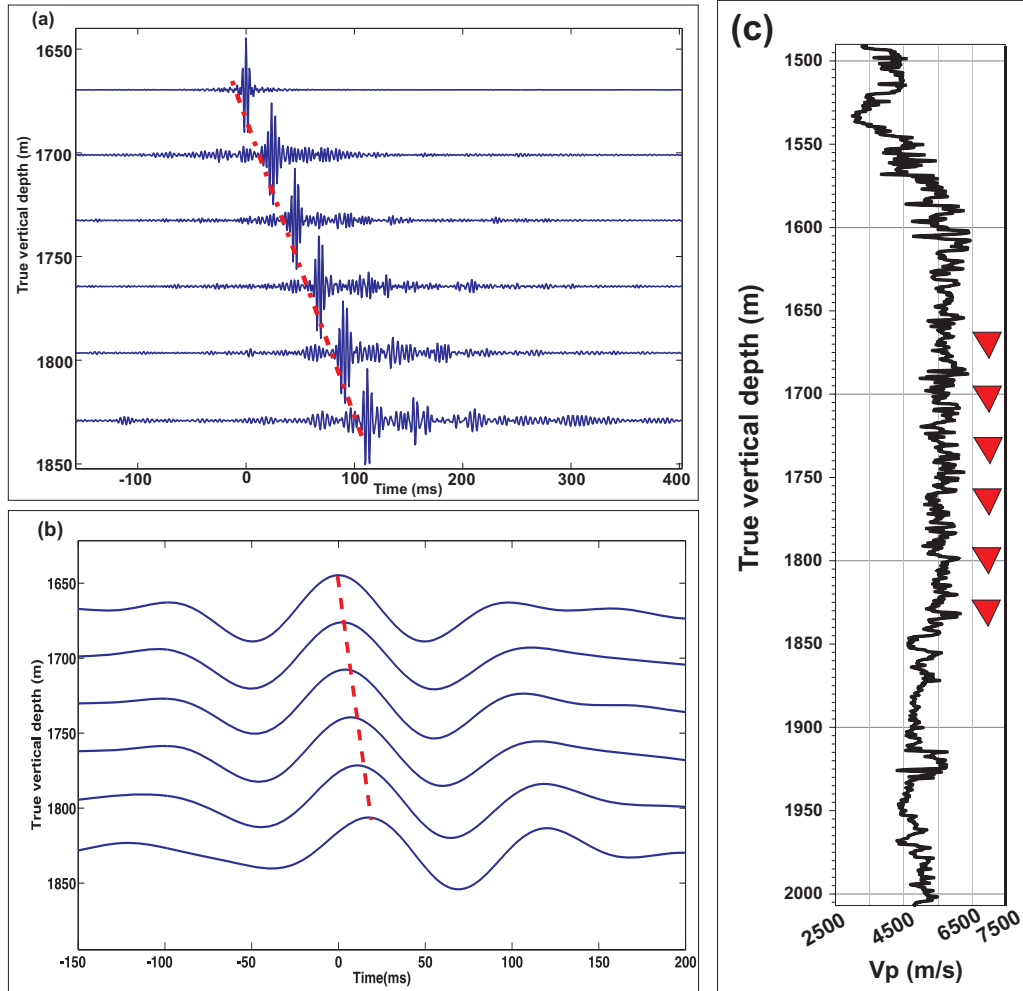


Figure 2.9: The averaged crosscorrelation functions between the vertical component of the shallowest receiver and all other receivers in the borehole array after applying a band-pass filter with corner frequencies of [180, 200, 400, 440] Hz. The moveout velocity of the reconstructed coherent and high-amplitude waveforms is approximately 1500 m/s. This suggests that these waveforms are most probably tube waves propagating down the array and within the borehole fluid. (b) Corresponding result for frequencies of [1, 5, 10, 15] Hz. The moveout velocity is 6200 m/s. (c) The sonic velocity log for P-waves. The high velocities suggest that the waveforms in (b) may represent a P-wave traveling down the array.

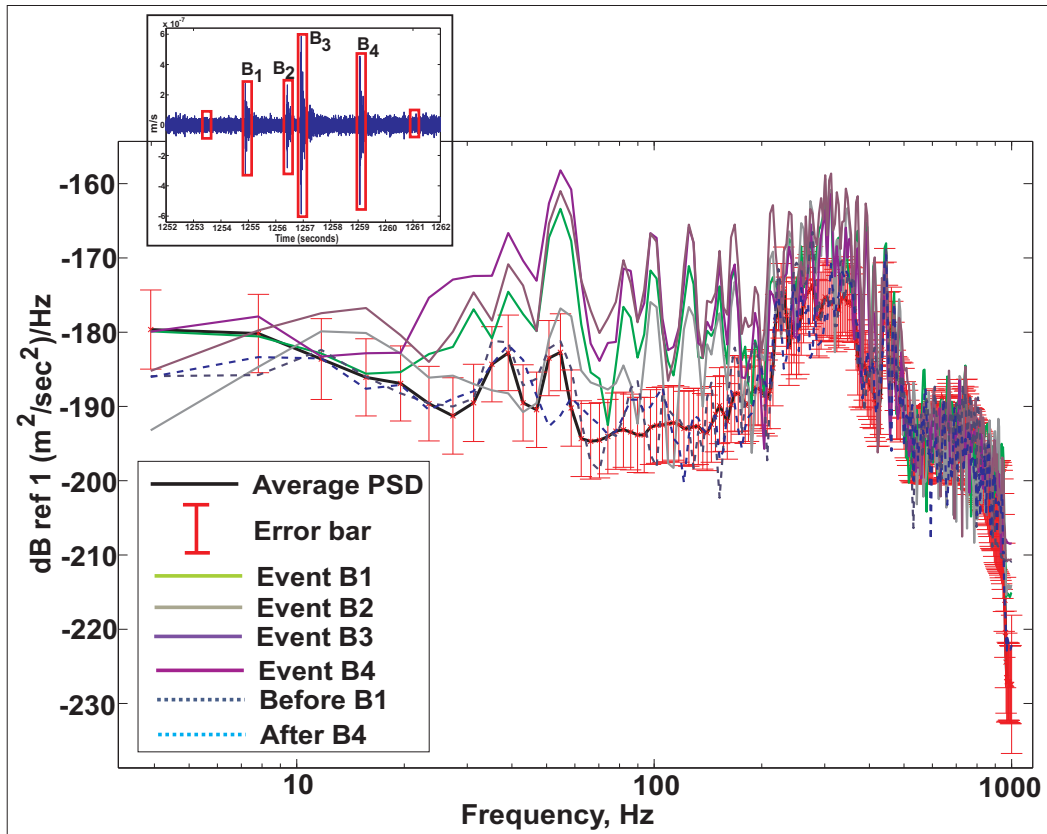


Figure 2.10: Four microseismic events (B_1 to B_4) during the 4th treatment stage recorded on shallowest borehole receiver with red boxes showing analyzed microseismic and noise recordings (top inset), PSD estimates for all four events (continuous colored line) and the averaged PSD (black line) including frequency-dependent standard deviations. The dashed lines correspond to PSD of segments just before B_1 and after B_4 .

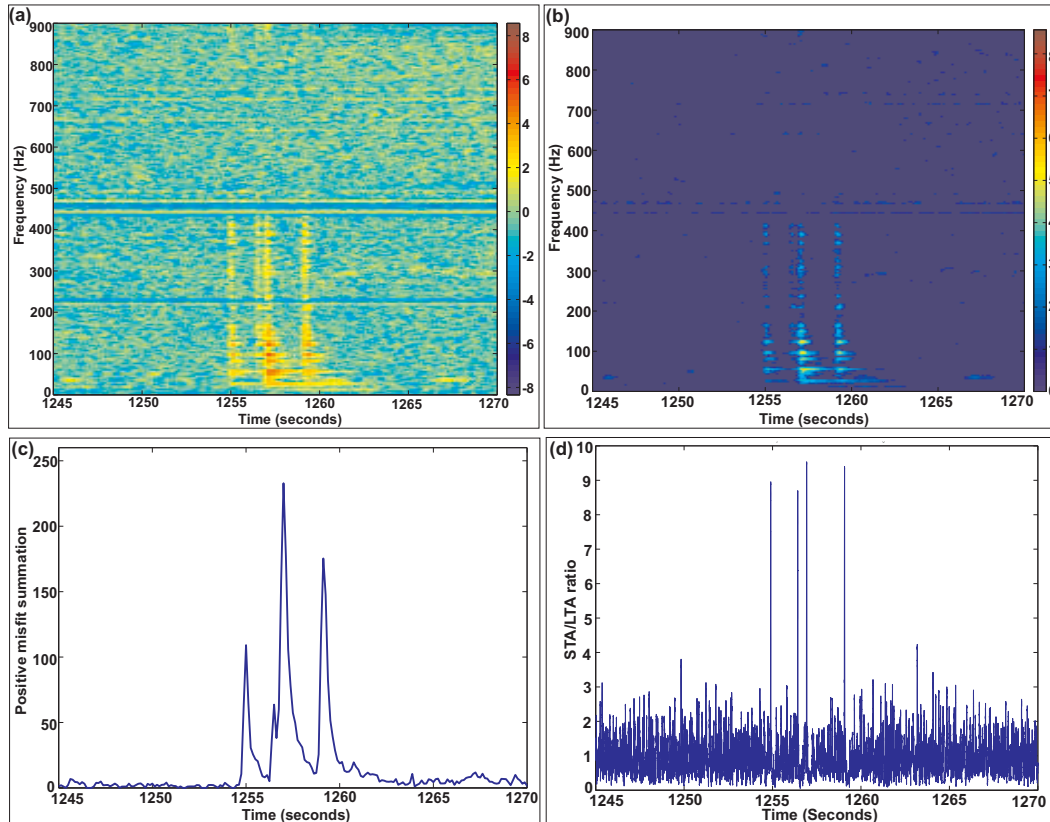


Figure 2.11: (a) The time-frequency representation of individual segment PSDs minus the average PSD, divided by the standard deviations at each frequency (Equation 2.2). (b) The same as (a) but only misfits greater than one standard deviation are kept. (c) The summation of results in (b) over all frequencies. The events can be identified by their anomalous high values. (d) The result of the STA/LTA analysis showing that these events represent high ratios.

CHAPTER 3

Comparison of the STA/LTA and power spectral density (PSD) methods for microseismic event detection¹

Robust event detection and picking is a prerequisite for reliable (micro-) seismic interpretations. Detection of weak events is a common challenge among various available event detection algorithms. In this chapter, we compare the performance of two event detection methods, the STA/LTA method, which is the most commonly used technique in industry, and a newly introduced method that is based on the PSD measurements. We have applied both techniques to a 1-hr long segment of the vertical component of some raw continuous data recorded at a borehole geophone in a hydraulic fracturing experiment. The PSD technique outperforms the STA/LTA technique by detecting a higher number of weak events while keeping the number of false alarms at a reasonable level. The time-frequency representations obtained through the PSD method can also help define a more suitable band-pass filter which is usually required for the STA/LTA method. The method offers thus much promise for automated event detection in industrial, local, regional, and global seismological data sets.

3.1 Introduction

Microseismic monitoring is a term commonly used to refer to methods that include the acquisition of continuous seismic data for locating and characterizing microseismicity induced by oilfield completion and production processes. This information can further be

¹A version of this chapter has been published as Vaezi, Y., and van der Baan, M., 2015, Comparison of the STA/LTA and power spectral density (PSD) methods for microseismic event detection, *Geophysical Journal International*, **203**(3), 1896–1908, doi: 10.1093/gji/ggv419.

used for monitoring resulting reservoir changes and understanding the associated geomechanical processes in the subsurface. It is not only considered as the only technology for hydrofracture monitoring, but is also known to have proven useful for geothermal studies, reservoir surveillance, and monitoring of CO₂ sequestration (Phillips et al., 2002; Maxwell et al., 2004; Warpinski, 2009; van der Baan et al., 2013). Here the term 'microseismicity' is defined as seismicity of magnitude less than 0 (Maxwell et al., 2010b) and should be distinguished from the terms 'microtremor' or 'microseism' that commonly refer to more or less continuous motion with a period of 4–20 s in the Earth that is unrelated to an earthquake (Ewing et al., 1957; Lee, 1935).

One of the main processing steps that is of paramount importance for accurately monitoring spatio-temporal distribution of microfractures is in fact to first detect these events. Since microseismic data are mostly acquired continuously they usually comprise large volumes. Likewise, earthquake monitoring can lead to large data volumes simply because many instruments can be operational over a long time span. Such large volumes of data call for an automatic event detection algorithm to replace manual detection, which is highly subjective and time consuming. Numerous automatic trigger algorithms are available which are generally characterized into time domain, frequency domain, particle motion processing, or pattern matching (Withers et al., 1998). They are all either based on the envelope, the absolute amplitude, or the power of signals in the frequency or time domains.

Although there are many sophisticated trigger methods they usually require complicated parameter adjustments to reflect actual signal and noise conditions at each seismic site. Finding suitable parameters has proven unwieldy and subject to error. Therefore, in practice, only relatively simple trigger algorithms have been really broadly accepted and can be found in seismic data recorders in the market and in most real-time processing packages. Among all, the STA/LTA technique (Allen, 1978) continues to remain as the most popular method in which the ratio of continuously calculated average energy (or envelope or absolute amplitude) of a recorded trace in two consecutive moving-time windows, a short-term window and a subsequent long-term window (STA/LTA ratio), is used as a criterion for picking. However, this method has also its own disadvantages. For instance, it requires careful setting of parameters (Trnkoczy, 2002) including a trigger threshold level and two window lengths (both short- and long-term windows). A low threshold can lead to many false triggers (false positives) while a high threshold may result in missing weak events (false negatives).

High sensitivity to the SNR level is a common shortcoming among various event detection algorithms. This may cause the weak events whose energies and amplitudes are comparable to the background noise to be obscured in the presence of strong noise and go untriggered. In this chapter we compare the performance of two event detection methods, a modified version

of the PSD technique introduced by Vaezi and van der Baan (2014) and the STA/LTA algorithm, when applied to 1-hr long single-trace data recorded by the vertical channel of a geophone in a borehole array in a microseismic experiment. We conclude that compared to the STA/LTA method, the PSD technique not only detects a larger number of weak events at a still tolerable number of false triggers, but also helps design a more suitable band-pass filter for further analysis of microseismic data, whereas the STA/LTA method usually requires the data to be band-passed prior to event detection. We also suggest that the PSD method would perform relatively better in triggering emerging events where the gradual amplitude increase can cause the STA/LTA method to fail.

3.2 Methodology

The idea behind the STA/LTA method is simple; the STA/LTA ratio is calculated continuously at each time t for every k th data channel x_t as $R = \frac{STA}{LTA}$, where

$$STA = \frac{1}{N_S} \sum_{n=1}^{N_S} y_{k,n}, \quad (3.1)$$

and

$$LTA = \frac{1}{N_L} \sum_{n=-N_L}^0 y_{k,n}. \quad (3.2)$$

The STA is the N_S -point short-term average and the LTA is the N_L -point long-term average. Note that we have considered non-overlapping STA and LTA windows. The parameter y_t is the characteristic function (CF) $y_t = g(x_t)$, which is devised in such a way that it enhances the signal changes. The common CF choices include energy ($y_t = x_t^2$) (McEvelly and Majer, 1982), absolute value ($y_t = |x_t|$) (Swindell and Snell, 1977), and envelope function ($y_t = \sqrt{x_t^2 + h(x_t)^2}$, where h denotes Hilbert transform) (Earle and Shearer, 1994). The STA measures the instantaneous amplitude level (or other CF) of the seismic signal and watches for events while the LTA takes care of the current average seismic noise amplitude (or other CF). When the ratio (R) of y_t exceeds a predetermined (user-selected) threshold τ , a detection is declared. The trigger is active until the ratio falls below a dettrigger threshold (Trnkoczy, 2002). Although they can be different, the trigger and dettrigger thresholds are commonly taken to be equal and are simply called the detection threshold ($\tau > 1$). The most important STA/LTA trigger algorithm parameters are thus the STA and LTA window lengths (N_S and N_L), and the detection threshold (τ).

For an event to be detected by the STA/LTA method, its energy (amplitude) should be adequately higher than that of the background noise. This simply may not be always true for weak events. Also the STA/LTA method is commonly applied to data which are band-passed over a frequency range where signal dominates with respect to the background noise. But in general, for energy detectors (such as STA/LTA method) no single filter will be optimal for a large variety of signals in a dynamic noise environment.

An alternative to this problem is to analyze the time series in the frequency domain. In order to detect events in a relatively stationary noise condition, Vaezi and van der Baan (2014) use the fact that the microseismic events typically represent stronger spectral content over a frequency band (narrow or wide, depending on the nature of the event) than that of the background noise. The main steps involved in this technique are described here.

Assume a continuous data record $x(t)$ that is stationary with average $\bar{x} = 0$. First the average PSD of the seismic background noise, $\overline{PSD}(f)$, is estimated using a Welch method (Welch, 1967; McNamara and Buland, 2004), which is known to reduce the variability of spectral estimates. By removing the energetic events, transients, and any types of noise bursts we consider only the noise at quiet times, $x'(t)$, to calculate the average noise PSD (Peterson, 1993). A quiet version of the data record can be roughly obtained by discarding samples of absolute amplitudes greater than a multiple of the original record's root-mean-square (RMS) amplitude (Figure 3.1). The quiet noise record is divided into M overlapping segments, $x'_m(t_l)$, each of length L , with $m = 1, 2, \dots, M$ and $l = 1, 2, \dots, L$, using windowing tapers of length L . The total average PSD is then calculated by averaging the one-sided PSD estimates over all the individual background noise segments:

$$\overline{PSD}(f) = \frac{1}{M} \sum_{i=1}^M PSD'_m(f), \quad (3.3)$$

where $PSD'_m(f)$ stands for the PSD estimate of the m th noise segment as a function of frequency f given by:

$$PSD'_m(f) = \begin{cases} \frac{a |\sum_{l=1}^L x'_m(t_l) w(t_l) e^{-j2\pi f l}|^2}{f_s L U} & \text{if } f = 0, f_{Nyq} \\ \frac{2a |\sum_{l=1}^L x'_m(t_l) w(t_l) e^{-j2\pi f l}|^2}{f_s L U} & \text{if } 0 < f < f_{Nyq} \end{cases} \quad m = 1, 2, \dots, M, \quad (3.4)$$

where a is a scale factor that accounts for variance reduction which depends on the type of the taper w , f_{Nyq} is the Nyquist frequency in Hz, f_s is the sampling frequency in Hz, $j = \sqrt{-1}$, and U is the window normalization constant that ensures the modified periodograms are asymptotically unbiased and is given by:

$$U = \frac{1}{L} \sum_{i=1}^L w(t_i)^2. \quad (3.5)$$

The standard deviations are also calculated at each frequency of the average PSD. As there are no redundant components in the Fourier transforms at the frequencies of 0 and f_{Nyq} , the PSD estimates at these frequencies do not double in equation 3.4 when converting the two-sided PSD estimates to one-sided PSDs, as opposed to those in the frequency range of $0 < f < f_{Nyq}$.

In the next step, the original data $x(t)$ are similarly divided into N overlapping segments of length L . In other words, a rolling window of predetermined length L is used to compute the PSD for each windowed segment throughout the original data $x(t)$:

$$PSD_n^t(f) = \begin{cases} \frac{a|\sum_{l=1}^L x_n(t_l)w(t_l)e^{-j2\pi ft_l}|^2}{f_s LU} & \text{if } f = 0, f_{Nyq} \\ \frac{2a|\sum_{l=1}^L x_n(t_l)w(t_l)e^{-j2\pi ft_l}|^2}{f_s LU} & \text{if } 0 < f < f_{Nyq} \end{cases} \quad n = 1, 2, \dots, N. \quad (3.6)$$

The purpose of using tapers is to suppress side-lobe spectral leakage and also reduce the bias of the spectral estimates. However, they increase the width of the main lobe of the spectral window, therefore reducing the resolution. There is always a trade-off between variance reduction and resolution as long as single data tapers are used for spectral estimations (Park et al., 1987). There are several types of tapers available with different variance and resolution properties (Harris, 1978). The Hanning and cosine tapers are the two most commonly used tapers. In this study, we use Hanning taper which has a relatively high variance but with very good spectral leakage properties (Park et al., 1987). Although applying moving average filters to single-taper spectral estimates reduces the variance, it adversely increases the bias of the estimate due to short-range loss of frequency resolution (Park et al., 1987). However, instead of single-taper estimations which suffer from relatively high variance, one can use the multitaper spectral estimation method to provide a more consistent estimate with lower variance. In this technique, a single spectral estimate is formed by combining several eigenspectra obtained by taking discrete Fourier transform of the product of several leakage-resistant tapers with the data (Thomson, 1982; Park et al., 1987). However, even multitaper analysis cannot fix the variability caused by non-stationary noise components of high amplitudes that, if present, may obscure the variability due to single data tapers.

The average PSD is then subtracted from all individual PSDs:

$$misfit_n^t(f) = PSD_n^t(f) - \overline{PSD}(f), \quad (3.7)$$

where $misfit_n^t(f)$ stands for the PSD difference at each time t associated with the middle point of the n th segment as a function of frequency f , which is hereafter denoted by $misfit_t(f)$ for simplicity, $PSD_n^t(f)$ denotes the individual PSD at the corresponding time, and $\overline{PSD}(f)$ is the calculated average PSD. These differences are then divided by standard deviations at each frequency to calculate the normalized PSDs $u_t(f)$ as:

$$u_t(f) = \frac{misfit_t(f)}{std(f)}, \quad (3.8)$$

where $std(f)$ is the standard deviation at frequency f computed from the PSDs of each noise segment $PSD'_m(f)$ analogous to equation 3.3. The resulting time-frequency representation highlights then all signals that stand out in a statistical sense from the reference spectrum, in this case the background noise. The ratios that are below 1 are set to zero to have a clearer depiction of the events:

$$\Gamma_t(f) = \begin{cases} u_t(f) & \text{if } u_t(f) > 1 \\ 0 & \text{otherwise} \end{cases}. \quad (3.9)$$

In other words, Vaezi and van der Baan (2014) suggest that any short time segment with a PSD statistically larger than the average PSD by some likelihood threshold includes a potential event. Both transient and persistent events are detectable by this method. This method can also be used for detecting individual frequency bands that are statistically above the average threshold, and subsequently determining suitable band-pass filters. In the next step an averaged PSD criterion is calculated by summing the computed quantities $\Gamma_t(f)$ over all frequencies and dividing them by the number of frequencies:

$$\Lambda_{PSD}(t) = \frac{\sum_{f=0}^{f_{Nyq}} \Gamma_t(f)}{N_f}, \quad (3.10)$$

where $\Lambda_{PSD}(t)$ is the averaged version of the PSD detection criterion as a function of time and N_f is the total number of frequencies. Another alternative approach is to use the average of $\Gamma_t(f)^2$ s as the triggering criterion:

$$\Phi_{PSD}(t) = \frac{\sum_{f=0}^{f_{Nyq}} \Gamma_t(f)^2}{N_f}. \quad (3.11)$$

When the $\Lambda_{PSD}(t)$ (or $\Phi_{PSD}(t)$) becomes larger than a predetermined value, say λ_{PSD} (or ϕ_{PSD}), an event is declared. Assuming a Gaussian distribution, for any selected λ_{PSD} , the probability in percentages that a trigger with a measured averaged PSD criterion of $\Lambda_{PSD}(t)$ at time t is due to noise can be calculated by:

$$\begin{aligned}
Pr\{\Lambda_{PSD} \text{ is noise} | \Lambda_{PSD} = \Lambda_{PSD}(t)\} \\
= \frac{1}{2}(1 - erf(\frac{\Lambda_{PSD}(t) - \mu}{\sigma\sqrt{2}})) \times 100\%,
\end{aligned}
\tag{3.12}$$

where μ and σ are the mean and standard deviation for the $\Lambda_{PSD}(t)$ and $erf(x)$ is the error function (Andrews, 1997) defined as:

$$erf(x) = \frac{2}{\sqrt{\pi}} \int_0^x e^{-t^2} dt. \tag{3.13}$$

3.3 Data set

The data set we have used for this study consists of a 1-hr segment out of 44-hr long continuous borehole microseismic data which were acquired to monitor multistage fracture treatments taking place at two horizontal wells for the purpose of increasing the formation permeability of a tight gas reservoir. The borehole array consists of 12 triaxial conventional 15-Hz geophones deployed in a vertical monitoring borehole, which is located between the two injection wells (Eaton et al., 2014). The sampling time interval is 0.25 ms. For simplicity we have considered the vertical component of the shallowest receiver (receiver 1) only. Figure 3.1 shows the data segment used for the current analysis.

3.4 Results

The parameters shown in Table 3.1 are used to calculate the STA/LTA ratios and the PSD criterion (Vaezi and van der Baan, 2014). The detection thresholds in both methods are selected in such a way that they give the best balance between the false alarms and missed events. The minimum event separation specifies the minimal time length between the end of the previous active triggering and the beginning of the current triggering. When two detections are very close in time, this parameter decides if they should be considered as two separated phases or not. The minimum event duration for the STA/LTA method is the minimal time length between the time of an event triggering and the time of detraggering. In other word, this parameter specifies the minimum duration of a seismic phase to be detected. If this parameter is very small, it becomes increasingly possible to misidentify an instrument glitch (a spike) as a seismic phase.

The average PSD is calculated using the same PSD window length and overlap as in Table 3.1 via a modified Welch method (McNamara and Buland, 2004). In order to prevent

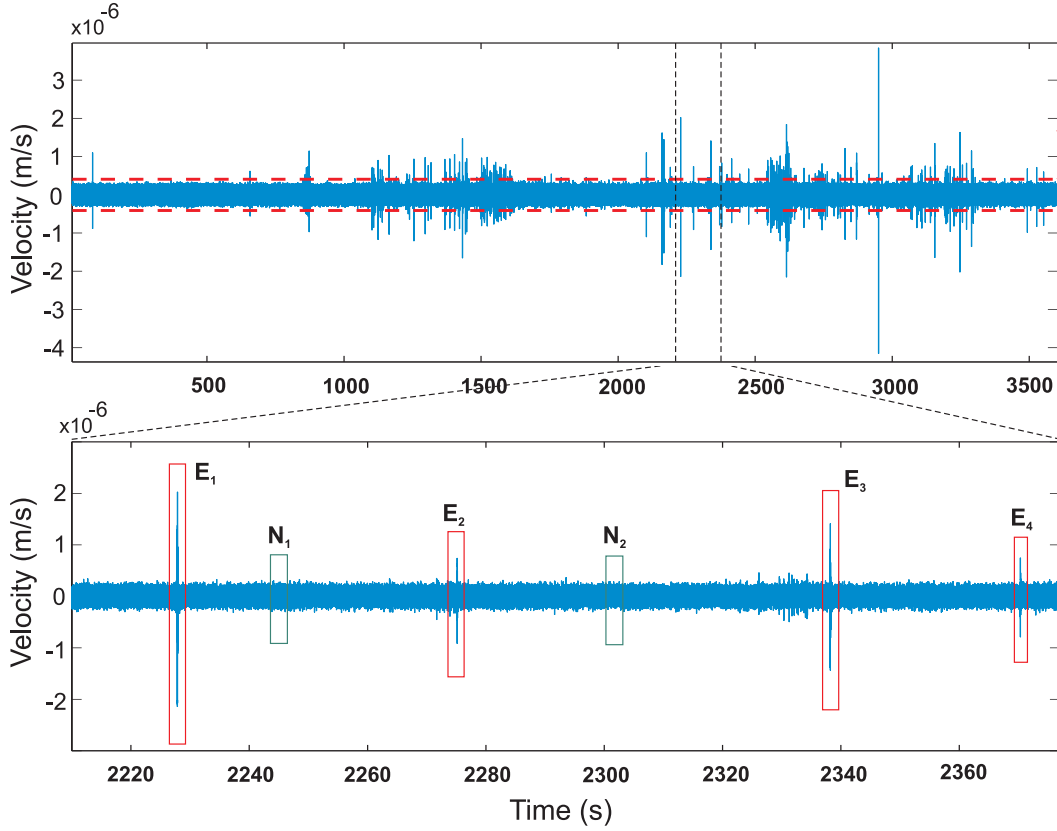


Figure 3.1: The Z-component of a 1-hr long segment of the raw continuous microseismic data and its zoomed view in which 4 events E_1 – E_4 and 2 background noise segments N_1 – N_2 are denoted by red and green boxes, respectively. The PSD estimates of these features are compared with the average PSD in Figure 3.2. Only the data in the region between the two red dashed lines (here with an absolute amplitude of 5 times the RMS amplitude) are used when calculating the average noise PSD.

Table 3.1: The parameters used for the STA/LTA and PSD detection methods

STA/LTA parameters		PSD parameters	
STA window length	30 ms (120 samples)	PSD window length	0.25 s (1000 samples)
LTA window length	100 ms (400 samples)	Window overlap	50%
Minimum event separation	0.5 s	Minimum event separation	0.5 s
Minimum event duration	50 ms		
STA/LTA detection threshold	2.00	PSD detection threshold	0.065

the energetic events, transients, and any types of noise bursts to bias the average noise PSD estimation, we simply removed the samples with absolute amplitudes greater than 5 times the RMS amplitude of the entire raw trace (red dashed lines in Figure 3.1). Therefore, we

roughly consider only the noise at quiet times to calculate the average noise PSD. Figure 3.2 shows the average PSD curve ($\overline{PSD}(f)$ in equation 3.3) in black along with the calculated standard deviations at each frequency ($std(f)$ in equation 3.8) in red bars. To better show how the PSD method works, this figure shows also the PSD estimates for 4 different microseismic events (red boxes in Figure 3.1) and two noise segments randomly selected from some quiet region of the data (green boxes in Figure 3.1) in different colors. Note that all event PSDs exceed the average PSD, especially at the frequencies below 120 Hz, while the sample noise PSDs lie mostly within one standard deviation. This property is used to detect microseismic events using the PSD technique. The spectral peaks observed at the frequency of 60 Hz and its multiples are related to the 60-Hz electric noise and its harmonic overtones. A frequency tolerance equal to two times the Rayleigh resolution (Harris, 1978) for the Hanning tapers used in this analysis is considered to discard the PSD ratios calculated around these frequencies and also to account for slight variability in the frequencies at which the harmonics are expected to appear.

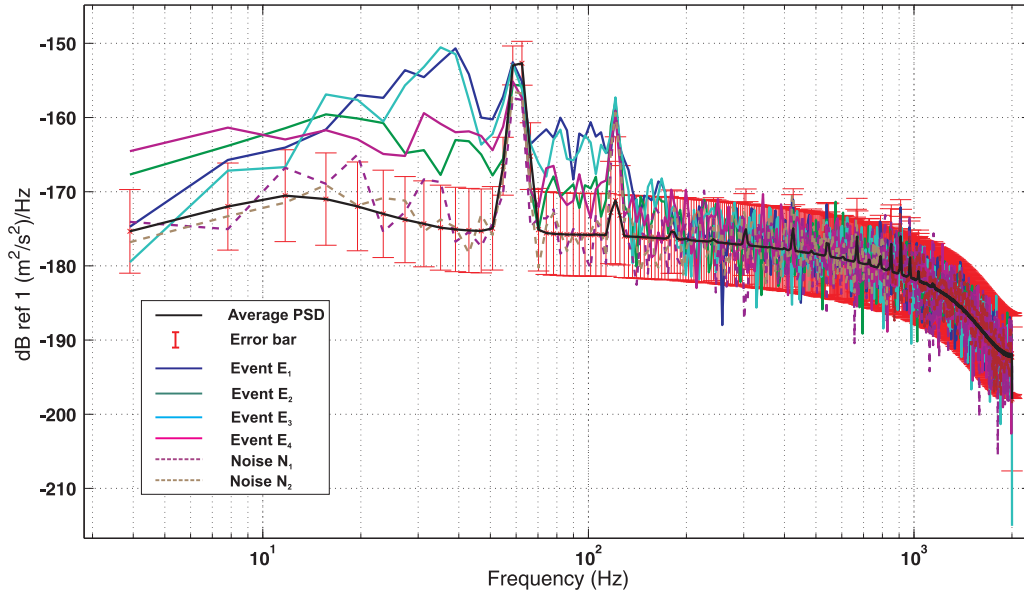


Figure 3.2: The average PSD curve (black) along with its standard deviations at each frequency (red bars), and the PSD estimates for four microseismic events E_1 – E_4 denoted by red boxes and two sample noise recordings N_1 – N_2 denoted by green boxes in the zoom-in view in Figure 3.1.

Figure 3.3a shows the time-frequency representation of the calculated $u_t(f)$ (equation 3.8). Figure 3.3b shows the thresholding function $\Gamma_t(f)$ (equation 3.9) in the frequency band of $[0, 150]$ Hz where the microseismic events are more evident. Figures 3.4a and b show

the calculated STA/LTA ratios and PSD criterion using the parameters listed in Table 3.1, respectively. The detection thresholds are plotted as red dashed lines in each figure.

The PSD method is applied to the raw data in Figure 3.1 and the STA/LTA technique is applied to the same data filtered with two narrow notch filters implemented at the frequencies of 60 and 120 Hz. The total number of triggered events by the PSD technique is 897, which is more than 2 times the total number of events triggered by the STA/LTA method that is 412 events. All the events triggered by both techniques are manually inspected in order to separate the false alarms (false positives) from the true positives (real events), and to statistically compare the performance of the two detection algorithms. In addition to microseismic events, any other coherent features recorded along the borehole array that may be of interest to an interpreter, such as low-frequency signals within regional events (small earthquakes) or long-period long-duration (LPLD) events (Das and Zoback, 2013; Caffagni et al., 2015), are also considered as true positives. Here, we refer to all these types of real events as 'master events'.

The first two rows in Table 3.2 compare the number of master events (microseismic or regional events), false alarms, and missed events in the two detection methods when applied to the corresponding data. Here, since all the master events detected by the STA/LTA method are also detected via the PSD technique, the latter is assumed to have detected all the master events present in the data, and is considered as the reference standard (zero missed events). Out of 897 events detected by the PSD method only 8 are false alarms and the rest are master events, of which 796 are identified as microseismic events and 93 as coherent signals mainly related to regional events (small earthquakes and their aftershocks) (Caffagni et al., 2015), as shown, for instance, in Figure 3.5. The STA/LTA method, on the other hand, has detected 399 master events, consisting of 364 microseismic events and 35 coherent signals related to regional events, which only account for approximately 44.8% of the total number of master events (that are assumed to have all been detected by the PSD method). There are a total number of 490 events that are missed by the STA/LTA method but detected by the PSD technique. Moreover, out of 412 events triggered by the STA/LTA algorithm 13 are false alarms, which are more than the number of false alarms in the PSD method. Therefore, the ratio of detected events over false triggers is improved significantly in the PSD method when compared to the STA/LTA technique.

Figures 3.6b and e show two raw segments of the vertical component data each including a potential weak microseismic event in the middle, which are obscured by the background noise. Therefore, they are not detectable by the STA/LTA technique even when applied to the data filtered with notch filters at the frequencies of 60 and 120 Hz. On the other hand, the modified PSD detection method has successfully detected these events due to their anomalous PSD estimate over some frequency band compared to the average noise

Table 3.2: The number of master events, false alarms, and missed events in the PSD method when applied to the raw data shown in Figure 3.1 (first row) and the STA/LTA method when applied to the same data filtered with two narrow notch filters at the frequencies of 60 and 120 Hz (second row). The third row presents similar variables for the STA/LTA method when applied to the same data filtered in the frequency band of [5, 55] Hz. Compared to the STA/LTA method, the PSD method not only detects more events but also provides less false alarms and missed events. Bandpassing the data over the frequency band deduced from the PSD method improves the performance of STA/LTA method.

	Master events			
	Microseismic events	Other coherent signals	False alarms	Missed events
PSD method (raw data)	796	93	8	0
STA/LTA method (notch-filtered data)	364	35	13	490
STA/LTA method (filtered data)	475	79	9	335

PSD, as indicated by the time-frequency representations of the above-unity PSD misfit ratios (equation 3.9) at the corresponding times shown in Figures 3.6a and d, respectively. In order to ensure these are indeed microseismic events they are band-passed over their dominant frequency band, [5, 55] Hz, deduced from their time-frequency representations at the times of their existence. Figures 3.6c and f show the corresponding band-passed Z-component time series at all the geophone levels (RCV1 is the shallowest receiver and so on). The apparent velocities associated with these events are estimated to be around 3280 and 3340 m/s, respectively, which are similar to the available average sonic P-wave velocity in the formations surrounding the monitoring well (Eaton et al., 2014). Therefore, their apparent velocities and their coherencies at all geophone levels confirm that they are microseismic events. The times at which these detections are made via the PSD method on the shallowest receiver are denoted by red arrows. Filtering the data over the frequency range of [5, 55] Hz causes these events to stand out of the background noise. Therefore, when applied to the data filtered in this frequency range, the STA/LTA method succeeds in detecting these two events.

These two events have PSD criteria that are larger by 2 and 1.8 times the standard deviation of the noise model within this frequency range, respectively. Assuming a Gaussian probability distribution, this quantifies to probabilities only from 2.27 to 3.6% that these are due to random noise fluctuations (equation 3.12).

The time-frequency representation of the measured PSD ratios for the whole 1-hr long segment (Figures 3.3a and b) shows that the frequency band over which the microseismic events are significantly dominant with respect to the noise is [5, 55] Hz. The detected microseis-

mic events have mostly PSD ratios between 2–8 in this frequency range that translate into 2.27–6.18E-14% probability that they are due to noise (equation 3.12). This can also help in designing suitable band-pass filters in order to better identify and analyze microseismic events.

The third row in Table 3.2 provides the number of master events, false alarms, and missed events in the STA/LTA method when applied to the data filtered in the frequency range of [5, 55] Hz deduced from the PSD technique. The performance of the STA/LTA method has been significantly improved when implemented to the data filtered over this frequency range. The number of detected master events has increased from 412 to 554, while the number of false alarms and missed events has reduced from 13 to 9 and from 490 to 335, respectively. The pronounced increase of number of detected coherent signals is mainly due to the fact that the dominant frequency band of the regional events that encompass most of these types of signals is [2, 25] Hz. Therefore these events are enhanced significantly and stand out clearly after applying the optimal filter, resulting in a higher number of detected coherent signals. Despite improvements in the STA/LTA method after applying an optimal band-pass filter to the data, the number of detected master events only account for approximately 62.3% of the total number of master events detected by the PSD technique when applied to the raw data. Also the PSD technique still provides a marginally lower number of false alarms and a smaller number of missed events. Therefore, the PSD technique remains as the superior event detection algorithm although implemented on the unfiltered data.

Figure 3.7 shows an example of a weak event that has been detected by the PSD method but is missed by the STA/LTA method applied to both the data filtered using notch filters at the frequencies of 60 and 120 Hz and the data band-passed in the frequency range of [5, 55] Hz. The comparable amplitude of the event with the background noise, even when the data is band-passed between 5 and 55 Hz, causes the STA/LTA method to fail in detecting this event. However, the elevated spectral content of the event with respect to that of the background noise makes the PSD method succeed in detecting this weak event. An apparent velocity of 3450 m/s and coherency of the waveforms along the receiver array confirm that this is an event.

3.5 Discussions

Our suggested event detection method uses a similar number of parameters as in the STA/LTA technique, namely a sliding window of pre-determined length and a detection threshold. As the PSD technique is based on the time-frequency representations, a trade-off between temporal and spectral resolutions should be considered when choosing the window length (Tary et al., 2015). The window length should be large enough to adequately account

for long-period components of the signals and small enough to be able to make a distinction between closely-spaced events. In the PSD method, one could choose an absolute pre-set threshold for triggering (equation 3.10 or 3.11) or a statistical one, in the sense that an event is triggered at any specific time once its likelihood to be due to noise only is less than a pre-selected value (equation 3.12).

The PSD method can also be utilized for designing a more suitable band-pass filter for further microseismic data analyses whereas the STA/LTA method usually requires band-passed data prior to event detection. The PSD algorithm is also insensitive to variations in the signal frequency content. However, it does assume stationary background noise conditions (Vaezi and van der Baan, 2014).

Both the STA/LTA and PSD techniques can be applied in a multi-channel strategy in which a voting scheme is used to trigger events (Trnkoczy, 2002). This way an event is declared once the total number of votes (weights) exceeds a given pre-set value. The spectral characteristics of the two horizontal channels may be significantly different from that of the vertical channel. Therefore, it is suggested that the PSD method is first applied separately to different components before combining the votes from different channels.

Both methods are incoherent (with respect to the background noise) energy detectors, meaning that triggered events may not correspond to microseismic events but other incoherent signals or even incoherent noise (e.g., spikes, bursts) which represent locally incoherent amplitudes (or energy or envelope) in the STA/LTA method or display sufficiently elevated spectral content over a frequency range in the PSD method. Therefore, a manual quality control is required to ensure that the declared events are indeed microseismic events as well as discard the false triggers. The reduced number of false alarms for the PSD method is important since it reduces the time spent on manual quality control.

Although the PSD method outperforms the STA/LTA method in detecting a higher number of weaker events, there are situations in which the PSD method may lead to false positives. An example of such situations is the occurrence of transient or time-varying noise which cannot be captured by the stationary background noise assumption. These can be caused by diurnal variations in the energy levels or originate from ambient noise sources (e.g. traffic, etc.). Electric noise (spikes in the signal) also lies in this category (Figures 3.8a–c). A possible remedy for the case of diurnal variations is to analyze the daily and nightly data separately by calculating separate average PSDs for each case and, therefore, setting different PSD ratio thresholds, respectively. Another example where the PSD method may result in false event declarations is when a local energy increase either related or unrelated to microseismic activities is detected on one receiver which may not be consistent with the records on other receivers in the array, or it is observed on a single receiver only (Figures 3.8d–f). As the events are visually inspected using the array records, such detections due to locally

elevated spectral energy levels only on an individual receiver are deemed false alarms as well. Furthermore, unusually large noise fluctuations are also undesired for the PSD method.

Among the 8 false alarms detected by the PSD method applied to our 1-hr long data set one is related to a transient (burst) noise and seven are related to features such as microseismic events or non-stationary noise which are detected on a single receiver only. Figures 3.8a–c show the burst, where its high amplitude and anomalously strong spectral content, especially over the frequency range of [7, 200] Hz, causes it to be detected as an event via the PSD technique. However, the visual inspection using geophones at all levels (Figure 3.8c) shows that this feature appears almost instantaneously on all geophones with differing polarities that can be due to instrument glitches or of other sources. Therefore, it is discarded as a false alarm during the manual quality control.

Figures 3.8d–f show an example where the PSD method detects an event when applied to the data on receiver 1. However, the manual quality control of this feature on geophone array shows no coherency along the array but only some local non-stationary increase in the energy level on other geophones. Therefore, this feature is also considered as a false alarm.

In this chapter we focused on event detection. We did not investigate how suitable the PSD technique is for onset picking. Onset-time picking and event detection are two different concepts. The former includes specifying the exact arrival time of the events, whereas the latter only quantifies the likelihood of the presence of events. When its parameters are well set, the STA/LTA technique seems to better determine the onset times, while the PSD method works best in identifying the presence of an event. On the other hand, the PSD method is likely to perform better in detection of emerging events where the gradual amplitude increase often makes the STA/LTA method fail. This can be explained by the fact that the PSD method is insensitive to the phase of the event, that is, an event can be detected as long as its spectral content is statistically large enough compared with the average PSD estimate, no matter whether the event is a minimum-, maximum-, or a zero-phase event (that is, has a front-loaded, end-loaded, or symmetric waveform). The STA/LTA method, on the other hand, is generally a minimum-phase event detector (that is, with most energy at the start of the arrival). One possible scheme to ensure superior performance is thus to start with the PSD technique for triggering, use the detected frequency range for band-pass filtering, and then employ the STA/LTA or another picking method to detect the arrival onsets.

The PSD technique also provides useful information for event classification or identification since it explicitly reveals the signal frequency content. Figure 3.9 shows the ‘discriminating frequencies’ for each of the 889 master events detected by the PSD method. The discriminating frequency of an event is here defined as the frequency at which the normalized PSD ($u_t(f)$ in equation 3.8) has its maximum value at the corresponding time of the event. Three

different event subsets associated with three distinct ranges of discriminating frequencies can roughly be identified; low-frequency events at the frequencies below 20 Hz which are mostly related to regional events (Figure 3.5), intermediate-frequency microseismic events in the frequency range of [20, 55] Hz which include the majority of the detected master events, and high-frequency microseismic events at the frequencies above 55 Hz. Therefore, we propose that the PSD method can further be used for event cluster analysis and phase identification (Shumway, 2003; Fagan et al., 2013; Anderson et al., 2010; Langer et al., 2006; Scarpetta et al., 2005). Note that the short-wavelength step-wise fluctuations observed in the discriminating frequencies are approximately equal to 4 Hz, which is the frequency step in the PSD technique, as we have used 0.25 s-long moving windows.

3.6 Conclusions

The PSD technique outperforms the STA/LTA method by detecting a higher number of weak microseismic events that are obscured by the background noise. When applied to the unfiltered data, the PSD method not only detects approximately 55.2% more master events than the STA/LTA method applied to the data filtered by notch filters at the frequencies of 60 and 120 Hz, but also reduces the number of false alarms and missed events. The PSD method has the advantage over the STA/LTA method that no prior band-pass filtering is required to enhance the SNR and also permits detection of signals with characteristically different frequency contents if the background noise spectrum is stationary. Even if the STA/LTA technique is applied to optimally filtered data, the PSD method still detects approximately 37.7% more master events with a similar number of false alarms. Therefore, the PSD method remains as the superior event detection algorithm to the STA/LTA technique.

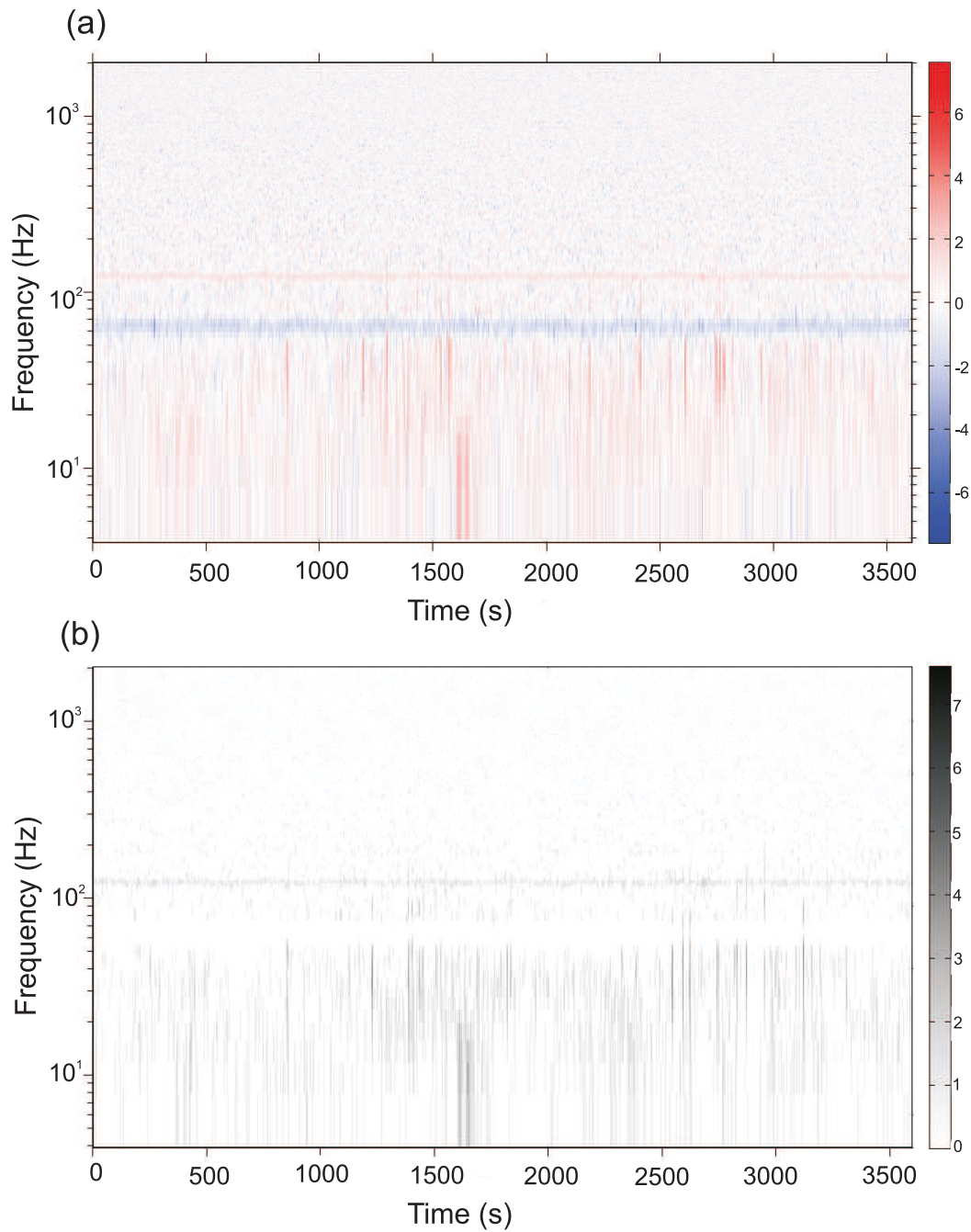


Figure 3.3: (a) The time-frequency representation of raw PSD ratios calculated using equation 3.8. (b) The same as (a) for PSD ratios calculated using equation 3.9. The microseismic events appear dominantly at the frequencies below 120 Hz. 120-Hz line is the first overtone of the removed 60-Hz electric noise.

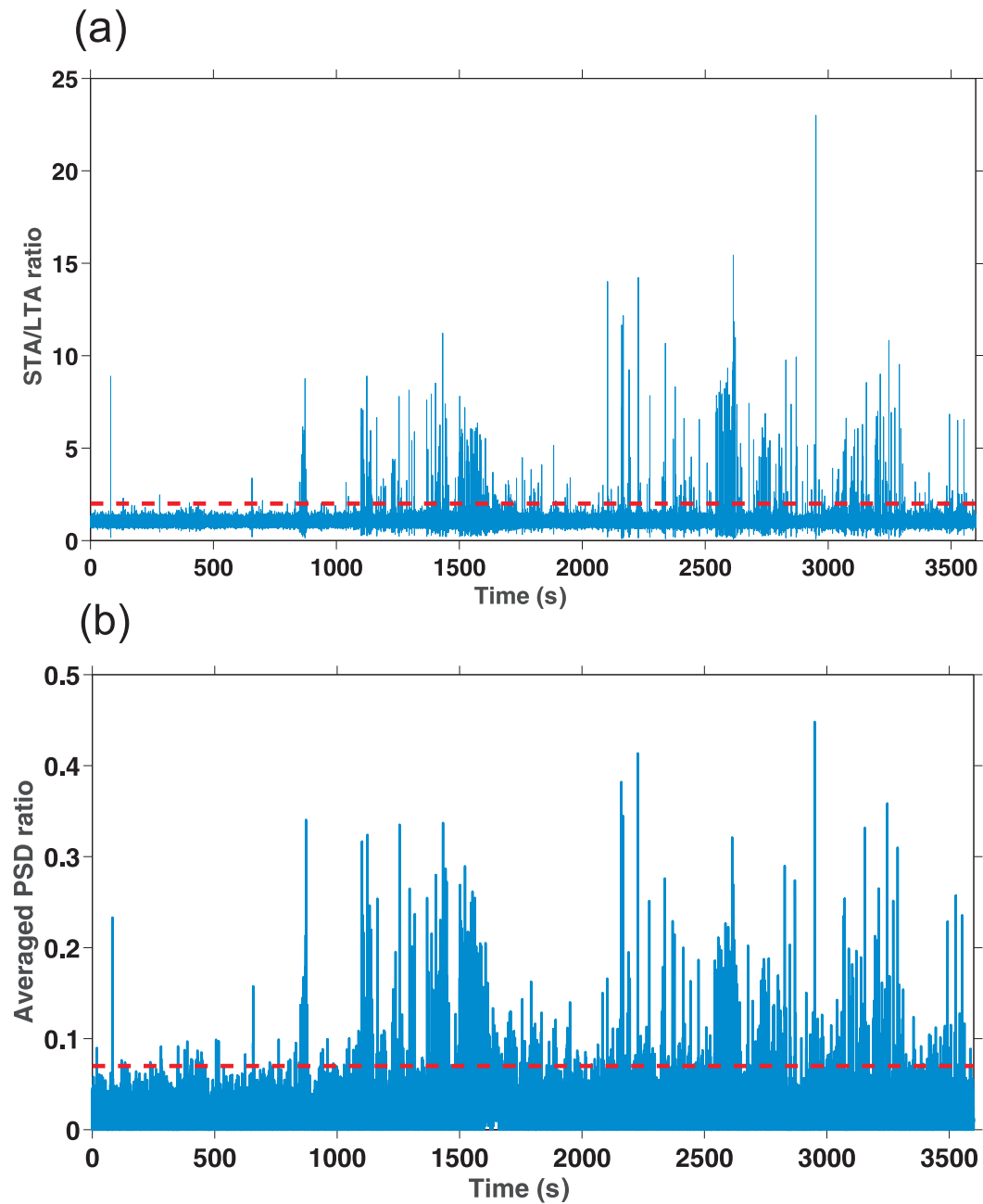


Figure 3.4: (a) The STA/LTA ratio calculated using the parameters listed in Table 3.1. (b) The PSD detection criterion calculated by equation 3.10 using the parameters listed in Table 3.1. The red dashed lines represent the detection threshold for each method.

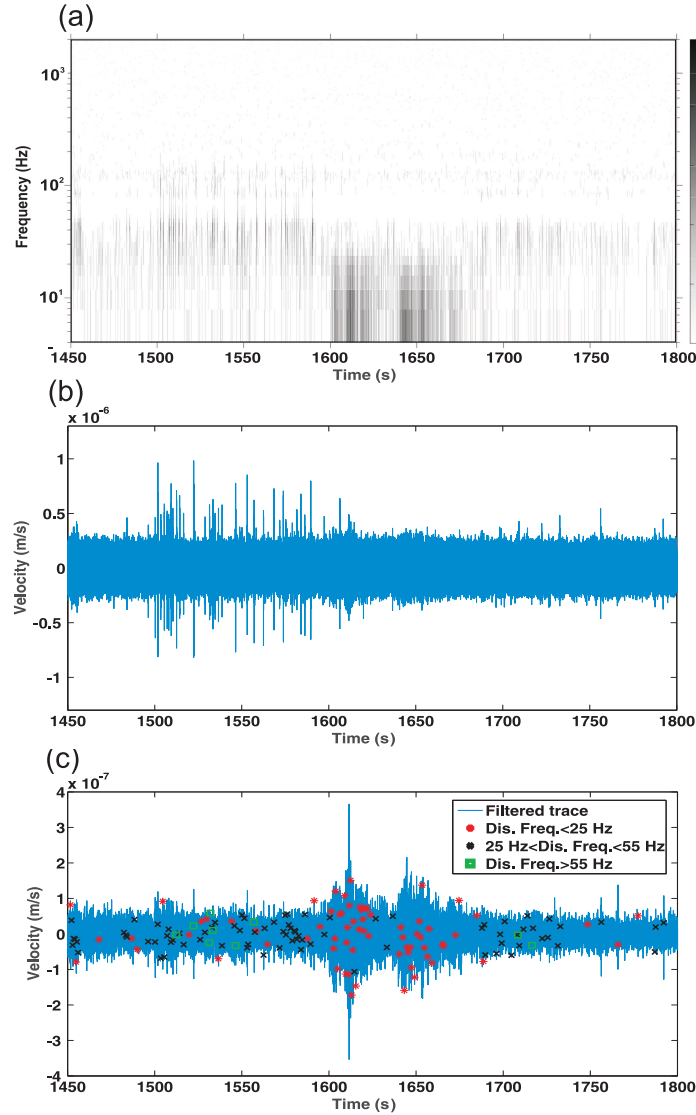


Figure 3.5: (a) The time-frequency representation of the above-unity PSD misfit ratios (equation 3.9) around some low-frequency signals that are detected by the PSD method. These signals are interpreted to arise mostly from small regional earthquakes observed in the data. (b) The associated raw data. (c) The same data after applying a band-pass filter over the frequency range of [2, 25] Hz. The master events detected by the PSD method at the time of appearance of these regional earthquakes are dominated by those of discriminating frequencies (Dis. Freq.) below 25 Hz (red stars). The detected events of discriminating frequencies in the range of [25, 55] Hz and above 55 Hz are mostly observed before and after these earthquakes and are denoted by black crosses and green squares, respectively. Compared with the STA/LTA method, the PSD method is significantly more sensitive to the coherent signal portions of length 0.25s within such events and detects a greater number of such signals (93 coherent events). This is because their PSDs are sufficiently stronger than the average PSD over their dominant frequency range. The STA/LTA, however, is only sensitive to abrupt amplitude changes and detects only 35 energetic signal among these events.

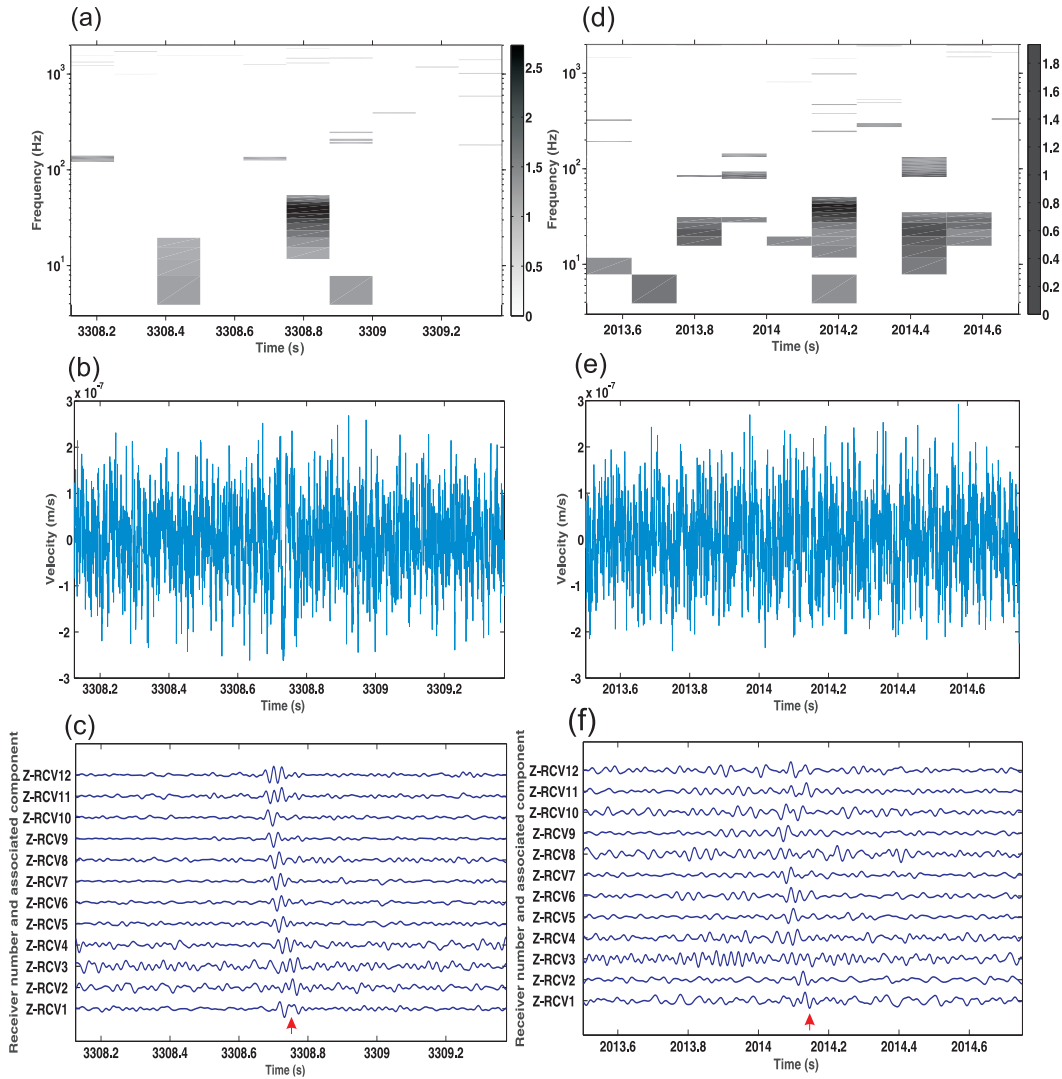


Figure 3.6: (a) and (d) The time-frequency representation of the above-unity PSD misfit ratios (equation 3.9) in the proximity of two events detected by PSD method and missed by the STA/LTA method when the latter is applied to the data filtered with notch filters at the frequencies of 60 and 120 Hz. These events are also detected by the STA/LTA method applied to the data band-passed over $[5, 55]$ Hz. The events are detected to be in the middle of these time windows. (b) and (e) The corresponding raw (unfiltered) waveforms of these two events on receiver 1. (c) and (f) The corresponding filtered time series over the frequency range of $[5, 55]$ Hz at all geophone levels. The red arrows show the detection times obtained by the PSD technique.

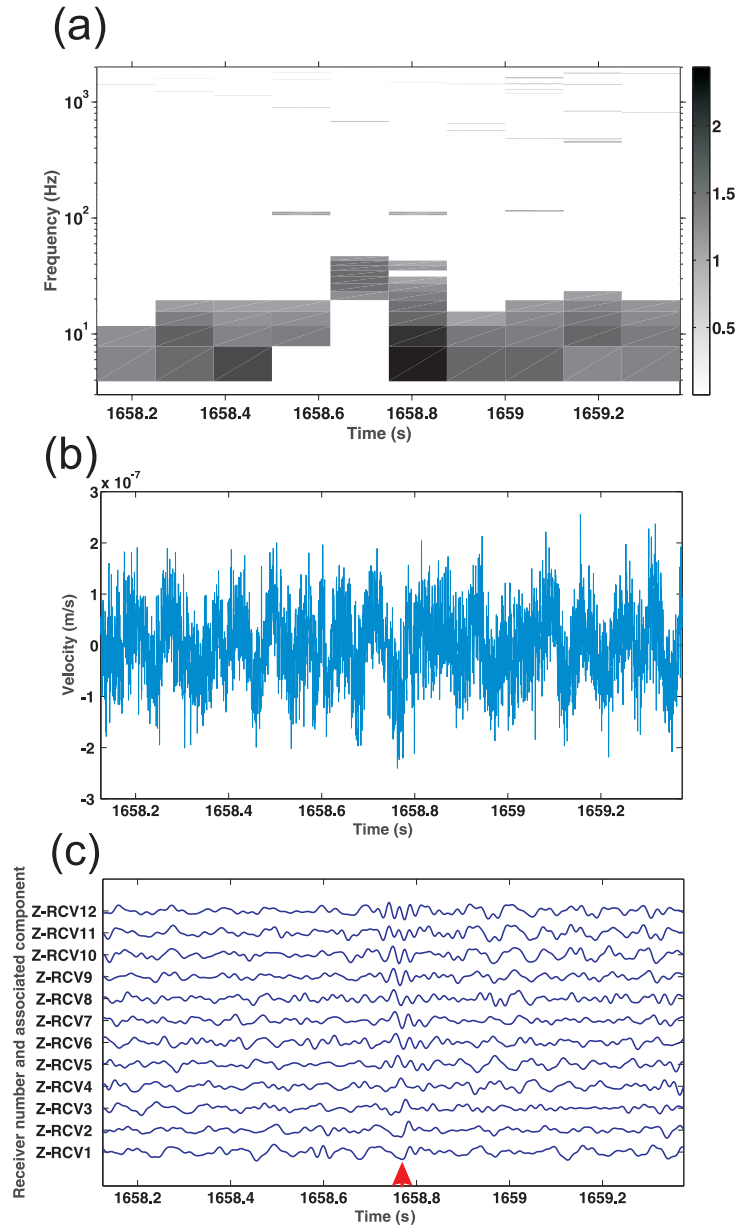


Figure 3.7: (a) The time-frequency representation of the above-unity PSD misfit ratios (equation 3.9) in the proximity of an event detected by PSD method and missed by the STA/LTA method, no matter whether the latter is applied to the data filtered with notch filters at the frequencies of 60 and 120 Hz or to the data filtered over the frequency range of $[5, 55]$ Hz. The event is detected to be in the middle of this time window. (b) The corresponding raw (unfiltered) waveform of this event on receiver 1. (c) The corresponding filtered time series over the frequency range of $[5, 55]$ Hz at all geophone levels. The red arrow shows the event detection time obtained by the PSD technique.

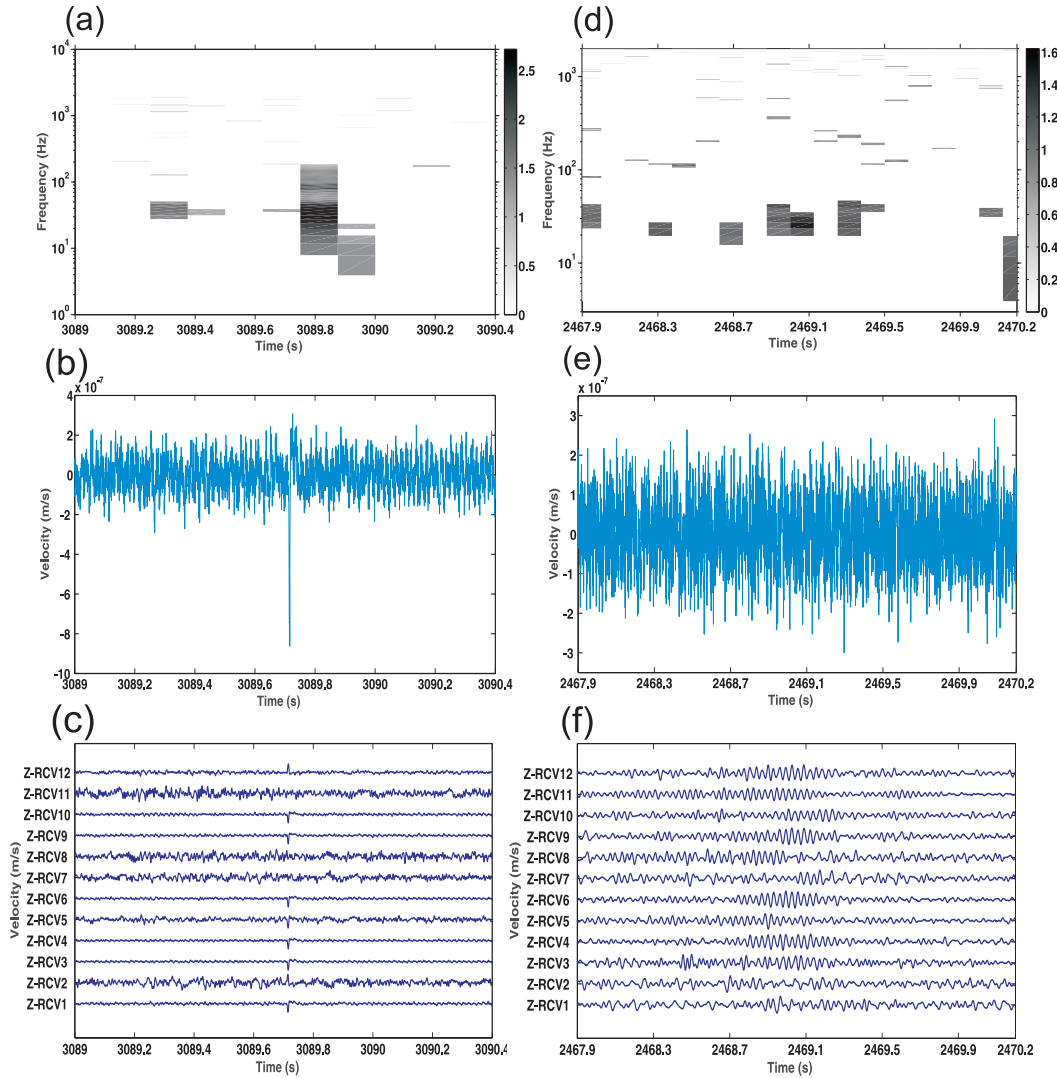


Figure 3.8: (a)–(c) Time-frequency representation of the PSD ratios, associated raw data on receiver 1, and the corresponding time series filtered between 7 and 200 Hz on all geophones, respectively, for a spiky noise feature. The PSD technique picks up this false alarm due to its coherent nature. (d)–(f) Time-frequency representation of the PSD ratios, associated raw data on receiver 1, and the corresponding time series filtered between 10 and 50 Hz on all geophones, respectively, for a second false alarm. Manual inspection on all geophone levels and lack of coherency along the array records suggests that this feature is most likely related to a local non-stationary energy variation as opposed to a microseismic event.

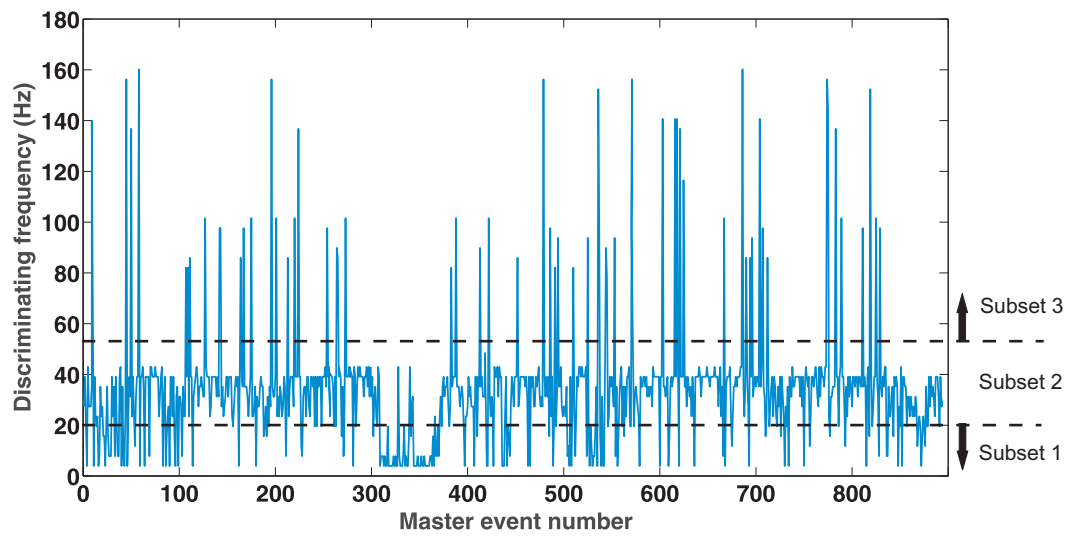


Figure 3.9: The discriminating frequencies corresponding to each master event detected by the PSD technique. The events can be categorized into three different event subsets based on the value of their discriminating frequencies, subsets 1 to 3, associated with events with discriminating frequency below 20 Hz, between 20 and 55 Hz, and above 55 Hz, respectively.

CHAPTER 4

Interferometric assessment of clamping quality of borehole geophones¹

Borehole arrays are often preferred over surface installations for hydraulic-fracture monitoring of deep experiments due to proximity to the treatment zone. Borehole geophone strings are typically clamped to the observation wellbore wall using electromechanical or magnetic devices in order for them to be in close contact with the surrounding formations and record the background noise and propagating wavefields related to the microseismic experiments. This contact needs to be maintained throughout the recording time. We have used seismic interferometry to assess the clamping quality of borehole geophone arrays. We suggest that the characteristics of the retrieved crosscorrelation functions between a reference receiver and other receivers in an array are indicative of the clamping quality of the former geophone to the borehole wall. We have also defined the concept of *separation frequency* or *emergence frequency* as the frequency below which direct body waves propagating along the receiver line are clearly observed on the crosscorrelation gathers. The crosscorrelation gathers associated with poorly clamped geophones show predominantly tube waves or incoherent waveforms. Body waves only emerge below very low separation frequencies. The crosscorrelation gathers of relatively better-coupled geophones, on the other hand, have higher separation frequencies. We have applied this method to four different borehole microseismic data sets, labeled here as A, B, C, and D, of which the data set D was previously known to suffer from some clamping issues. The data sets B and C with inferred better coupling had separation frequencies of approximately 60 Hz, whereas the other two data sets are characterized by lower separation frequencies, 15 Hz for the data set A and 20 Hz

¹A version of this chapter has been published as Vaezi, Y., and van der Baan, M., 2015, Interferometric assessment of clamping quality of borehole geophones, *Geophysics*, **80**(6), WC89–WC98, doi: 10.1190/geo2015-0193.1.

for the data set D, suggesting relatively poorer coupling.

4.1 Introduction

Hydraulic-fracture mapping remains to be the most common and notable use of microseismic monitoring in oil and gas industry. It involves the acquisition of continuous seismic data for the purpose of detecting and locating microseismic events induced by fracture treatments using 3C borehole and/or surface instruments (van der Baan et al., 2013). It provides information on fracture growth and propagation, thereby allowing operators to optimize stimulations, well spacing, the overall field development and also avoid geohazards (Warpinski, 2009).

Due to proximity to the treatment zone, borehole installations are often preferred over surface counterparts for hydraulic-fracture monitoring of deep experiments. This is because, first, seismic waves emitted from microseismic events suffer much less from intrinsic attenuation and geometrical spreading; second, the level of interface waves, which can mask weaker and distant microseismic events, is considerably lower with respect to surface recordings. Therefore, the chance of detecting a greater number of microseismic events is higher. However, geophones deployed in the observation well must be clamped properly to the side of the wellbore wall in order for their recorded time series to directly represent true ground motion. In the industry, 6 to 12 geophones are typically installed with an equidistant spacing and are secured in place with an electromechanical or magnetic device that has a clamping force to weight ratio of at least 10 (St-Onge et al., 2013). The deeper the borehole array is deployed, the lower the control on the clamping quality, especially for deviated boreholes if the array is installed on the bending section of the wellbore. If a geophone is detached from the borehole wall and is hanging inside the wellbore it will most likely record only tube waves propagating inside the wellbore fluid, instrument self-noise, high-frequency waves traveling within the wellbore casing, or the high-amplitude constituents of noise wavefields and signals traveling in the surrounding formations. Therefore, the detached geophones can no longer be used for analysis of seismic background noise or monitoring of hydraulic fracture treatments.

Seismic interferometry in passive seismic experiments refers to a technique for retrieving coherent part of noise which is deeply buried under local seemingly incoherent noise. It retrieves the coherent part of noise propagating between two receivers by crosscorrelating their noise records. For regional-scale networks of widely separated stations on the Earth's surface, applying seismic interferometry to long noise records at every station pair in the array retrieves the corresponding inter-receiver Green's function or impulse response, dominated commonly by slowly attenuated surface (Rayleigh) waves, assuming that the noise-source distribution is spatially homogeneous around the stations (Lobkis and Weaver, 2001; Derode

et al., 2003b; Shapiro and Campillo, 2004; Snieder, 2004; Wapenaar, 2004). The surface-wave dispersion curves estimated from these noise correlation functions can consequently be inverted for 2D and 3D velocity structures.

Body waves may also be extracted from seismic interferometry of closely-spaced receivers (Roux et al., 2005; Draganov et al., 2007; Gerstoft et al., 2008; Zhang et al., 2010; Ruigrok et al., 2011). Miyazawa et al. (2008) extracted P- and S-waves from noise crosscorrelation on a vertical array deployed for monitoring steam injection into an oil reservoir. Grechka and Zhao (2012) retrieved body waves and the inferred corresponding formation velocity models nearby the wellbore from correlation of noise records at borehole geophones in different single and crosswell acquisition geometries in microseismic monitoring experiments and for both horizontal and vertical observation wells. Their velocity estimates are comparable to the existing velocity models obtained from well logs.

Following discussions with Vladimir Grechka, we explore if we can evaluate clamping quality of borehole geophones based on the characteristics and types of waves retrieved by seismic interferometry. We propose that if the crosscorrelation functions are dominated by tube waves across a large range of frequencies then the coupling quality is less than desirable as the geophone array may be hanging inside the wellbore so that it records mostly tube waves. On the other hand, detection of dominant P- and S-waves at a large range of frequencies in the correlation gathers confirms that the geophones are well clamped to the wellbore.

Our working hypothesis is that before the start of the hydraulic fracture treatments both body and surface waves mostly originate from anthropogenic and environmental sources at the surface (Bonnetoy-Claudet et al., 2006). Conversion of these body waves and surface waves at the wellhead or wellbore joints can generate interface (tube) waves (Lamb, 1898; White, 1965; Hardage, 1981; Daley et al., 2003). Seismic interferometry retrieves predominantly waves traveling between receivers, as explained by the stationary-phase approximation (Snieder, 2004). It thus emphasizes both body waves and tube waves traveling along the borehole. The tube waves travel within the wellbore fluid and will be retrieved by seismic interferometry irrespective of the geophone clamping quality. Since the tube waves arise from external converted body and surface waves, we postulate that the amplitudes of the body waves outside of the borehole are stronger than those of the tube waves within the borehole. Well-coupled receivers will thus record both external body waves and internal tube waves. At low frequencies all media become effectively homogeneous (Backus, 1962; Burridge et al., 1994; van der Baan, 2001). Even poorly coupled receivers will thus detect the external body waves at some low frequency. We define the term *separation frequency* or *emergence frequency* as the frequency below which the body waves become observable on the crosscorrelation gathers. We suggest that a high separation frequency indicates better geophone clamping quality.

4.2 Methodology

The data processing steps involved in this method are summarized in Figure 4.1. Our approach for generation of crosscorrelation functions is similar to the scheme proposed by Bensen et al. (2007). In the first step, the mean and the linear trends are removed from the recorded time series at each station in the borehole array. The series are also corrected for the instrument response to increase the bandwidth over which the crosscorrelation functions are calculated. As crosscorrelation is a linear process, a Welch method is adopted for calculation of crosscorrelation functions for which a sliding window time length and percentage of overlap between successive windows is defined (Seats et al., 2012). The window length is set to optimize a trade-off between the fluctuations associated with a short time window and costly numerical computation resulting from a long time window. The window should also be long enough to assure the emergence of signals of the Green's function in the single-time window crosscorrelation functions. The window length is limited to emphasize waves traveling along the receiver line as opposed to those emerging from different angles due to wave scattering or reflections. A time-window length similar to the duration of the dominating coherent disturbing signals (e.g., teleseismic surface waves for surface recordings and tube waves for borehole arrays) is expected to provide reliable results (Groos et al., 2012). The crosscorrelation functions converge faster and are more robust using short-duration overlapping time windows than with long, non-overlapping time windows (Seats et al., 2012).

Applying a band-pass filter to each window determines the bandwidth for each crosscorrelation function. This is especially advantageous if the underlying signals and/or noise are characterized by different frequency bands. Next, individual windows are normalized in the time domain to reduce the effect of earthquakes, non-stationary noise sources, and instrumental irregularities on the crosscorrelation functions (Bensen et al., 2007). The most common and effective temporal normalization methods are running absolute mean normalization and 1-bit (replacing the waveforms with their sign) normalization (Larose et al., 2004; Bensen et al., 2007). We use 1-bit normalization which theoretically limits the recorded noise to only the dominant arrivals in it at every time sample. Therefore, it helps emphasize all waves traveling between receivers over those arriving from other directions due to wave scattering or reflections. Spectral whitening is necessary to increase the resulting crosscorrelation functions' bandwidth, prevent spectral peaks to overwhelm the crosscorrelation functions, and therefore equalize the large differences in spectral amplitudes of the signals contributing to the seismic noise in the analyzed frequency range (Bensen et al., 2007; Groos et al., 2012). It involves dividing the frequency spectrum of each window by a smooth version of the spectrum. A regularization parameter is used to prevent dividing by zero at zero frequencies. In the next step a reference geophone is selected. The normalized

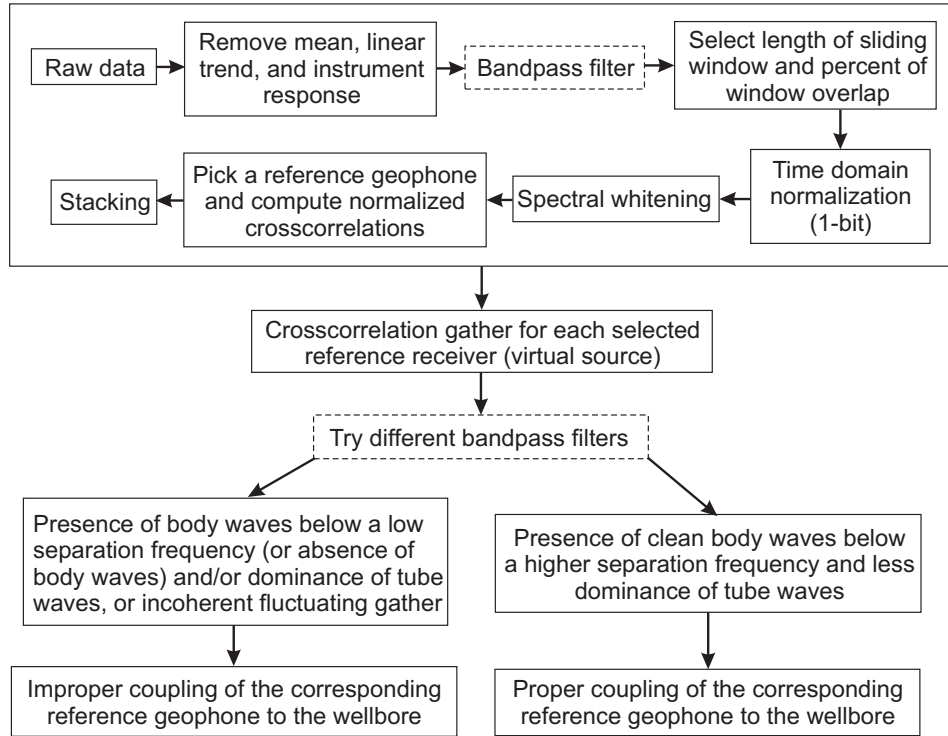


Figure 4.1: The processing scheme for generation of crosscorrelation functions and following steps for assessment of clamping quality of borehole geophones. The dashed boxes indicate that only one of these steps is implemented at a time.

crosscorrelations (crosscorrelations divided by the geometric mean of the autocorrelation functions at lag zero) are calculated between this receiver and all other receivers in the array.

Several single-time window crosscorrelation functions are then stacked to obtain a final crosscorrelation function with enhanced SNR. The final crosscorrelation function calculated between the reference receiver and all other receivers in the array simulates a response that would have been measured at each of the latter receivers if there were a source at the position of the reference receiver. This is commonly called a virtual source (Bakulin and Calvert, 2006).

The above processing scheme can be applied to every component and every reference receiver. If ignored prior to temporal normalization, different band-pass filters can be applied to the resulting correlation gather, which is what we did in the examples provided here. We suggest that if the gather is dominated across a large range of frequencies by only tube waves traveling within the borehole fluid, the coupling of the toolstring is not properly performed. However, some low-frequency direct body waves can still be retrieved because they

can still be sensed by a hanging receiver in the wellbore. Moreover, lack of coherency in the correlation gather of a reference receiver is interpreted as bad coupling. On the other hand, emergence of meaningful and "clean" body waves throughout the correlation gather for quite a wide bandwidth confirms that the borehole array has maintained its attachment to the wellbore wall. We refer to the frequency below which body waves propagating along the receiver line become observable on the crosscorrelation functions as the separation frequency or emergence frequency. We suggest that the value of the emergence frequency is directly proportional to coupling quality: poorly clamped borehole arrays show lower emergence frequencies than the well-clamped arrays.

4.3 Examples

We have applied this procedure to pre-frac recordings of four different borehole microseismic experiments, A, B, C, and D. The first two data sets were acquired to monitor multistage fracture treatments taking place at two horizontal wells for the purpose of increasing the formation permeability of two tight gas reservoirs. Data set A comes from a geophone array consisting of six 3C 4.5-Hz receivers deployed in a deviated well (Eaton et al., 2013). The data were sampled at 2000 Hz. The array is installed in the bending portion of the observation well where the deviation angles are less than 20 degrees (Figures 4.2a and b). Data set B (Eaton et al., 2014) is from an array in a vertical observation well composed of 12 3C receivers (Figures 4.2c and d). The geophones have a natural frequency of 15 Hz and the recordings were sampled at 4000 Hz.

Data set C is a proprietary data set. It was acquired by 12 3C geophones deployed in a vertical borehole (Figures 4.2e and f) for the purpose of monitoring two hydraulic fracturing stages in a tight gas reservoir from the Cardium formation in the foreland basin of the Western Canada Sedimentary Basin (Tary et al., 2014). The geophones have a natural frequency of 15 Hz and the data were sampled at 4000 Hz.

The sensor array in data set D consists of two sets of 4.5-Hz geophones and force balance accelerometers (FBAs) at the top of the array followed by an array of eight conventional 15-Hz geophones, of which seven are quad-element geophones and one is dual-element geophone at the bottom. The second FBA was disabled and was not taken into account in the calculations. Other than 30 min of recorded data, relative northing and easting, depths of geophones and their orientations no other information about data set D was available. Figure 4.2g shows the relative positions of the geophones in this data set. Table 4.1 provides a summary of the properties of each data set.

The correlation functions calculated between the vertical component of the shallowest receiver and that of all other receivers in the array for data sets A, B, and C are shown in

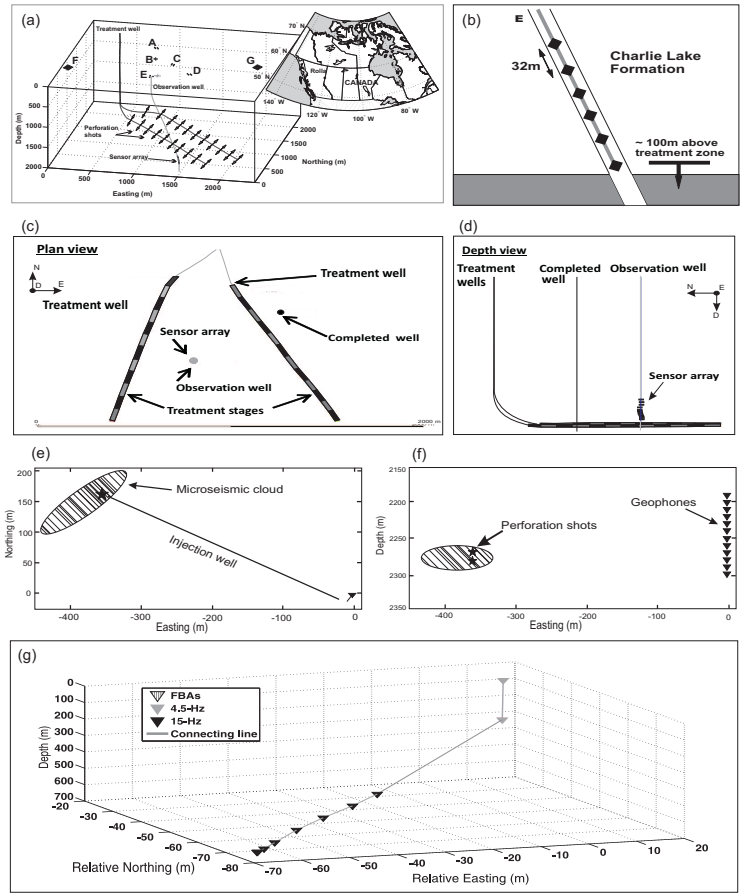


Figure 4.2: (a) The 3D view of the acquisition geometry of data set A and (b) its cross section showing borehole toolstring of six 3C geophones in the deviated observation well (modified after Eaton et al. (2013)). (c) The plan and (d) depth view of the acquisition geometry of data set B with the vertical borehole array consisting of 12 3C geophones (reproduced from Eaton et al. (2014)). (e) Map view and (f) cross section of the experimental setup of data set C (reproduced from Tary et al. (2014)). (g) The 3D view of the borehole array geometry of the experiment D consisting of two FBAs, two 4.5-Hz geophones, and eight 15-Hz geophones. The gray line is only a connecting line and does not represent the monitoring well geometry. The FBAs and 4.5-Hz geophones are closely spaced and cannot be distinguished in this figure.

Table 4.1: Summary of data set properties

Data set	Number of receivers	Type of receivers	Sampling frequency (Hz)	Monitoring well orientation	Inferred relative clamping quality
A	6	4.5-Hz	2000	slightly deviated	low
B	12	15-Hz	4000	vertical	high
C	12	15-Hz	4000	vertical	high
D	12	4.5-Hz,15-Hz,and FBA	4000	deviated	low

Figures 4.3, 4.4, and 4.5, respectively. Sliding time windows of 15-, 5-, and 5-s length overlapping by 50% are used to generate the crosscorrelation functions in each case, respectively.

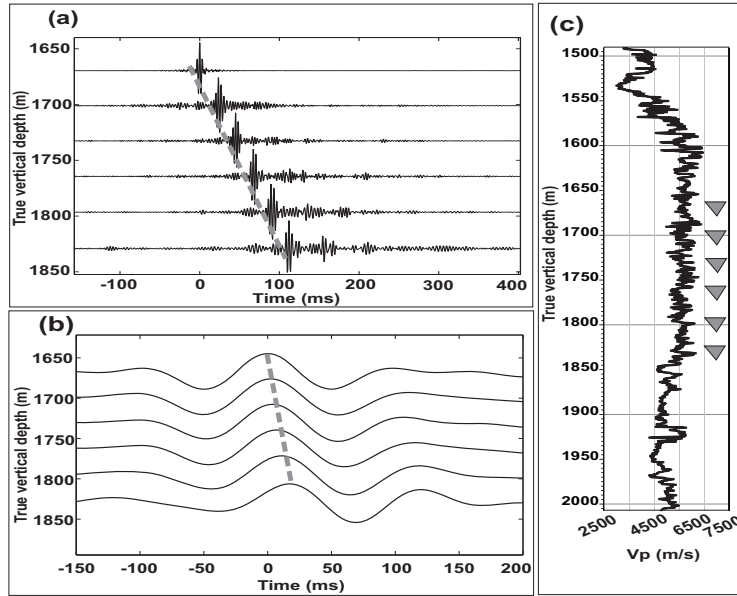


Figure 4.3: (a) The averaged crosscorrelation functions between the vertical component of the shallowest receiver and all other receivers in the borehole array of data set A after a band-pass filter with corner frequencies of [180, 200, 400, 440] Hz. The moveout velocity of the retrieved coherent and high-amplitude waveforms is approximately 1500 m/s. This suggests that these waveforms are most probably tube waves propagating down the array and within the borehole fluid. (b) Corresponding result for frequencies of [1, 5, 10, 15] Hz. The moveout velocity is 6200 m/s. (c) The sonic velocity log for P-waves. The high velocities suggest that the waveforms in (b) may represent a P-wave traveling down the array (Vaezi and van der Baan, 2014).

In the situation where noise sources are homogeneously distributed around the receivers, seismic interferometry is expected to result in a time-symmetric crosscorrelation function (Stehly et al., 2006). A one-sided crosscorrelation function can be generated if the noise sources are predominantly located on one side of the receiver pairs (Shapiro and Campillo, 2004). The crosscorrelation functions for data set A are dominated by one-sided tube waves at most of their bandwidth. Figure 4.3a shows the result after being band-pass filtered using a filter with corner frequencies of [180, 200, 400, 440] Hz. The best-fitting line through the coherent arrivals (dashed line) in this figure represents a velocity of about 1500 m/s implying that these waveforms are related to tube waves traveling down the array. Figure 4.3b shows the crosscorrelation functions after being band-pass filtered using a narrow filter with corner frequencies of [1, 5, 10, 15] Hz. The best-fitting line through these waveforms

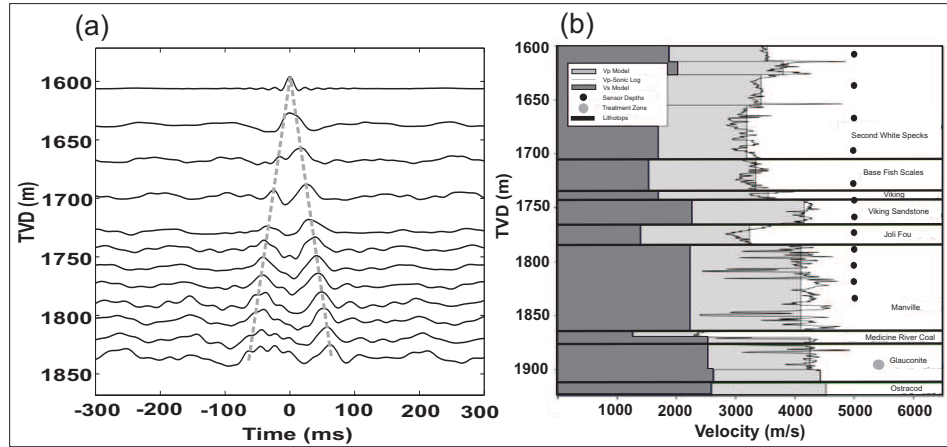


Figure 4.4: (a) Similar to Figure 4.3a but for data set B after a 60-Hz low-pass filter. The time-symmetric responses (red dashed lines) represent a moveout velocity of around 3800 m/s. (b) The P- and S-wave velocity models from sonic logs and after calibration. Velocity similarities suggest that the waveforms in (a) are upward and downward propagating P-waves. P- and S-wave velocity models are shown in light and dark gray, respectively. The continuous black line denotes the sonic P-wave velocity log. The black dots show the geophone positions and the red dot signifies the treatment zone. The formation tops are outlined by green lines.

shows a moveout velocity of nearly 6200 m/s, which is slightly greater than the average P-wave velocity obtained from sonic log (Figure 4.3c), which is about 5800 m/s. Such high velocities are due to the presence of large bodies of anhydrites, limestone, and dolomite in the formation hosting the array. The velocity discrepancy can be partially due to the fact that the velocity estimated from the retrieved crosscorrelation functions is an apparent velocity (Sheriff and Geldart, 1995; Das and Zoback, 2011), which is equal or higher than the expected (average) direct P-wave velocity through the formation. Apparent velocity increases with increasing angle between the wave propagation direction and the line of receivers. Knowing the velocities, we determined the angle of arrival of the wavefront using the relation $\cos \theta = \text{formation velocity} / \text{apparent velocity}$, where θ is the angle of arrival of the wavefront. This angle is calculated to be approximately 21° . Similar results are obtained for all other reference geophones in the array. These observations can be explained by the geophone array being detached from the wellbore wall. It is possible that coupling is not optimal or even absent due to deployment in the bending sections of the wellbore, which provide less stability for the receivers. Vaezi and van der Baan (2014) postulated that relatively high instrument noise in addition to the distance of the observation well from the individual perforations was responsible for the relatively low number of detected microseismic events in this data set. Clamping issues could provide an alternative explanation.

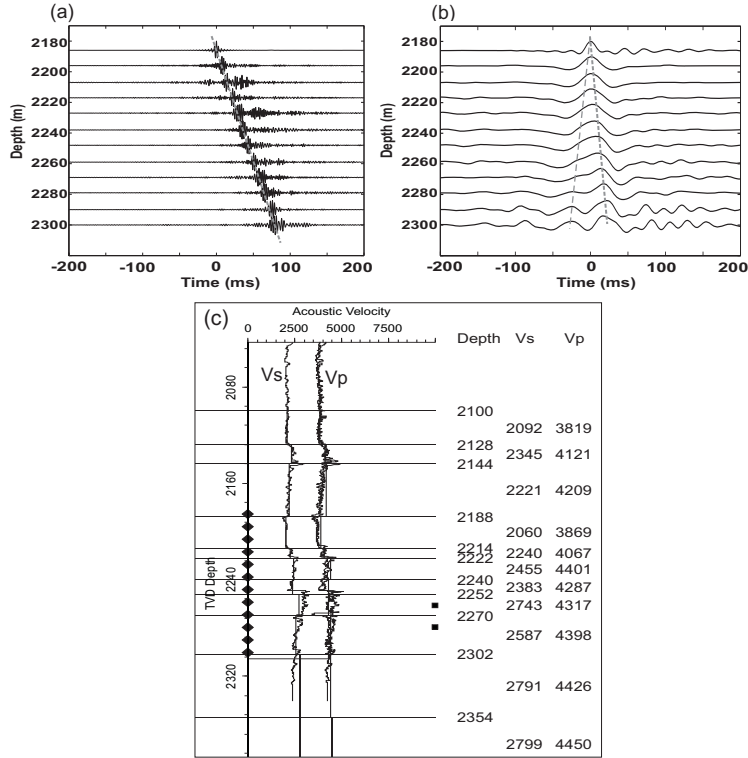


Figure 4.5: (a) The averaged crosscorrelation functions between the vertical component of the shallowest receiver and all other receivers in the borehole array of data set C after a band-pass filter with corner frequencies of [220, 240, 460, 480] Hz and calculated using the time series recorded before the fracture treatments. The moveout velocity of the retrieved coherent and high-amplitude waveforms is approximately 1500 m/s. This suggests that these waveforms are most probably tube waves propagating down the array and within the borehole fluid. (b) Corresponding result after applying a 60-Hz low-pass filter. The moveout velocity is 4300 m/s. (c) The sonic velocity log for P- and S-waves. The squares and the diamonds represent the treatment zones and geophone depths, respectively. The velocity similarities suggest that the waveforms in (b) may represent a P-wave traveling down the array.

Figure 4.4a, on the other hand, shows the emergence of nearly time-symmetric crosscorrelation functions for data set B. Due to presence of significant 60-Hz electric noise and its overtones in the raw data and the crosscorrelation functions, the results are low-passed below 60 Hz. The best-fitting line through these clean waveforms shows a moveout velocity of approximately 3800 m/s. A comparison of this velocity with the velocity model calculated from the sonic log (Figure 4.4b) confirms that these waveforms are upward and downward propagating direct P-waves traveling within the formation adjacent to the wellbore. The individual crosscorrelation functions correlated well with one another.

The crosscorrelation functions for data set C are also dominated by downgoing tube waves across a large range of frequencies with approximate moveout velocity of 1500 m/s (Figure 4.5a). However, when filtered below 60 Hz, a clear presence of coherent waveforms with best-fitting moveout velocity of approximately 4300 m/s is observed. Again a comparison of this velocity with the sonic velocities near the wellbore (Figure 4.5c) confirms that these waveforms are upward and downward propagating direct P-waves traveling within the formation adjacent to the wellbore.

Therefore, compared to the crosscorrelation functions of data set A, the crosscorrelation functions of data sets B and C demonstrate a broader frequency range across which clear body waves (P-waves here) are present (Table 4.1). In other words, they show a higher emergence frequency. Given these observations we suggest that the borehole arrays in data sets B and C are better clamped than in data set A.

Well-parallel (generally vertical) components typically have better coupling than the well-perpendicular (mostly horizontal) ones due to their larger contact area with the borehole wall. One can also compute the crosscorrelation functions for the horizontal components to try to assess their clamping as they experience more rotations and instability. The crosscorrelation functions can also be calculated for every reference receiver in the array in order to better identify the incoherently behaving geophones due to their bad clamping. Receivers with coupling issues will generate lower emergence frequencies and generally lower-quality body-wave retrievals than their better coupled counterparts.

We applied the technique to data set D with known geophone clamping issues (Figure 4.2g). Sliding time windows of 1-s length overlapping by 50% are used to generate the crosscorrelation functions for this data set. Figures 4.6a–c show the crosscorrelation functions calculated between each component of the shallowest receiver (an FBA) and the corresponding components of the other receivers in the frequency range of [200, 500] Hz, which is the dominant frequency interval of the resulting crosscorrelation functions. These crosscorrelation functions are dominated by downgoing tube waves with a moveout velocity of nearly 1400 m/s as denoted by the dashed lines. Figures 4.6d to f show similar crosscorrelation functions when low-pass filtered below 25 Hz. Again no clear presence of direct body waves is observed, which confirms that the shallowest receiver is undergoing clamping issues. Similar observations are made for all the FBAs and 4.5-Hz receivers in the array.

Similarly, the crosscorrelation functions for the deeper 15-Hz geophones are calculated. Figures 4.7a–c show the crosscorrelation functions for different components of the 4th receiver (the shallowest 15-Hz geophone) in the dominant frequency range of [50, 500] Hz. They are dominated by tube waves propagating in the upward and downward directions with moveout velocity of nearly 1400 m/s as indicated by dashed lines. The illumination is still one-sided, as can be seen from the fact that above the virtual source, the tube waves are re-

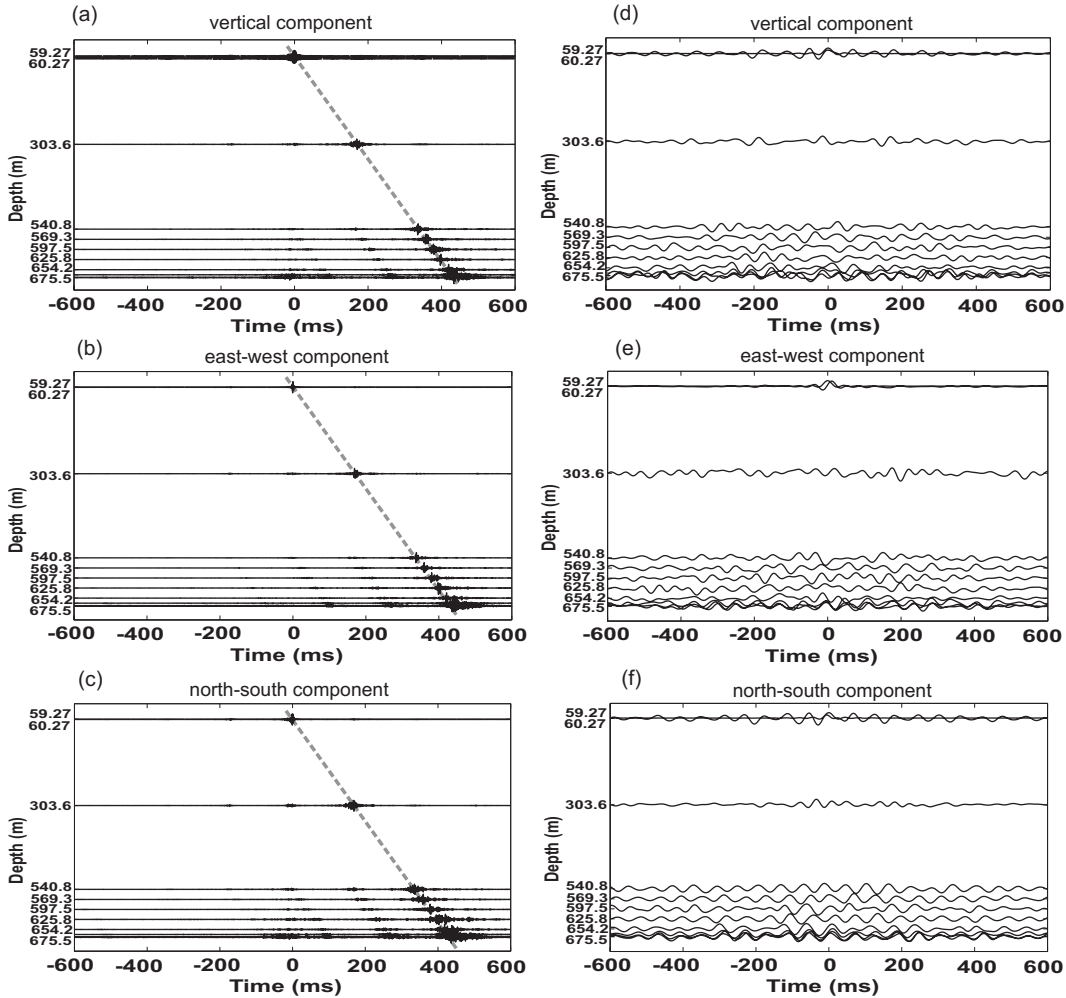


Figure 4.6: (a)–(c) The crosscorrelation functions calculated between different components of the shallowest receiver and the corresponding components at other receivers of the array in data set D filtered in the dominant frequency range of [200, 500] Hz. The results are dominated by downgoing tube waves as denoted by dashed lines of moveout velocity of approximately 1400 m/s. (d)–(f) Similar results for the frequencies below 25 Hz. No clear body waves are observed indicative of improper clamping at this reference receiver location.

trieved only at negative times. Figures 4.7d–f show similar crosscorrelation functions when low-pass filtered below 25 Hz. They show some indications of retrieved direct P-waves with a moveout velocity of approximately 3800 m/s. Although this suggests that the 4th receiver is relatively better clamped to the borehole than the shallowest receiver, the very low emergence frequency still indicates poor coupling. The retrieved direct P-waves are clearer on

the vertical component than on the horizontal components implying better clamping of the vertical component over the horizontal ones.

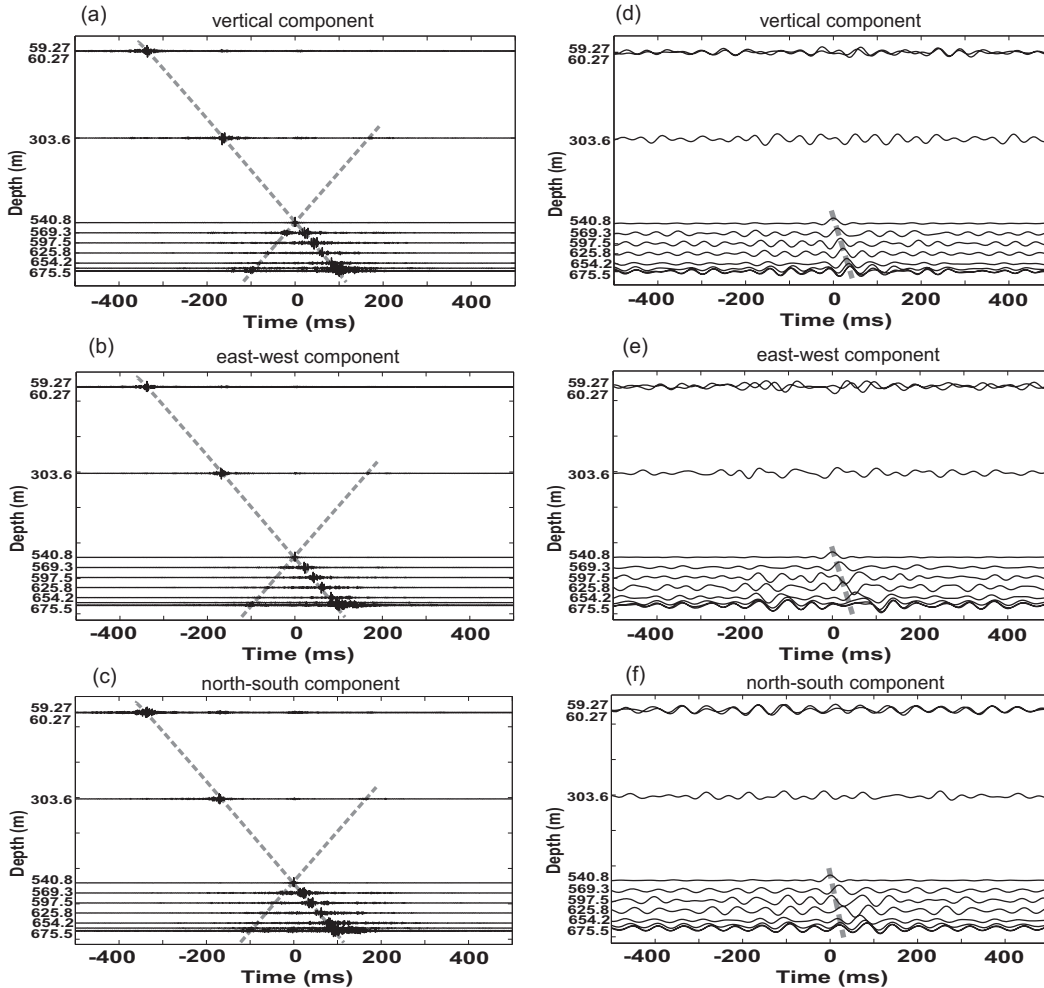


Figure 4.7: (a)–(c) The crosscorrelation functions calculated between different components of the 4th receiver and the corresponding components at other receivers of the array in data set D filtered in the dominant frequency range of [50, 500] Hz. The results are dominated by two-sided tube waves of moveout velocity of nearly 1400 m/s as denoted by dashed lines. (d)–(f) Similar results for the frequencies below 25 Hz. Although this suggests that the 4th receiver is relatively better clamped to the borehole than the shallowest receiver, the very low emergence frequency indicates still bad coupling.

4.4 Discussions

The observations made from four different data sets and the comparison of the results with the available information confirm our working hypothesis that the emergence frequency indeed works as a quality indicator for assessing geophone coupling. The body waves retrieved via seismic interferometry in these four examples are predominantly P-waves. The lack of S-wave retrievals may be explained by the fact that S-wave attenuation is generally larger than P-wave attenuation. S-waves may only appear at even lower frequencies due to their attenuation from the surface to the receivers. Miyazawa et al. (2008) retrieved both P- and S-waves using borehole seismic interferometry, but this was in a much shallower setting. In addition, we applied crosscorrelation to vertical geophones thereby emphasizing P-waves. Also the depth of a receiver array can play an important role in the amount of body-wave attenuation (Carter et al., 1991; Stephen et al., 1994) and thereby the magnitude of the separation frequency. The effect of deployment depth can also be investigated in further studies of data sets acquired at different depths.

We have also tested representing the crosscorrelation functions in the frequency-slowness (f - p) domain in order to find the dominant range of frequencies for each type of waves more reliably, which can further be used for more suitable band-pass filtering of the crosscorrelation functions. Our approach for generating an f - p representation for a crosscorrelation gather is via τ - p transform (McMechan and Yedlin, 1981; van der Baan, 2009): The crosscorrelation gather is first converted into the τ - p domain and a Fourier transform is then computed along the time dimension thus leading to the velocity (or slowness) spectrum representation. Because of the limited number of traces, the crosscorrelation functions of our four data sets did not result in clear and robust f - p representations. However, we suggest that this method can significantly help once a high number of borehole geophones are available.

Because seismic interferometry is most sensitive to waves traveling between receivers and the source of the external body waves is postulated to be at the surface, the proposed methodology is most promising for assessing coupling quality in both vertical and deviated boreholes. However, Grechka and Zhao (2012) did retrieve body waves for horizontal wells. Thus, the suggested method may hold promise for any borehole orientation.

The interferometric approach for geophone-clamping assessment is currently a relative measure: coupling is better with increasing emergence frequencies. Note that the intensity of tube waves observed on the data can be influenced by the borehole fluid (usually water) and its level in addition to the coupling quality; a higher level of the borehole fluid leads to stronger tube waves (Galperin, 1985). For the crosscorrelation functions, the 1-bit normalization might play a role here as well because it favors preservation of the dominant arrivals

in the noise. Therefore, the amount of the tube waves retrieved by our seismic interferometry technique may give some insight into the fluid level inside the borehole. Moreover, in addition to microseismic data, this method can potentially be applied to VSP data as well.

An important factor for this method is the amount of data required to compute the cross-correlation functions reliably and the consistency of the results using data before, during, and after the hydraulic fracturing treatment. Tests indicate that conclusions on coupling were maintained even if only 2-min data segments were used taken prior to the start of the hydraulic fracturing treatment. Longer segments led to enhanced body-wave retrieval but did not change the conclusions. Little change was detected for segments longer than 5 min.

Results may depend somewhat on the sliding time window length and overlap percentage, the time and frequency normalizations, the distribution of sources around the receivers, and the degree of scattering. For instance, 1-bit normalization favors the retrieval of the dominant arrivals. Nonetheless, this indicates that 5–15 min of passive recordings are likely to be sufficient to assess coupling quality before start of the hydraulic fracturing treatments.

In our case, no changes in coupling quality were detected before, during, and after the hydraulic fracturing treatment in multi-day data sets A, B, and C. De Meersman et al. (2009), using the complex, multi-trace polarization analysis approach of De Meersman et al. (2006), detected rotations in borehole geophones over time, most likely due to coupling issues. We suggest that the seismic interferometry method may also be used to detect such changes by comparing if the polarizations of the retrieved body waves change over time for the two horizontal components.

4.5 Conclusions

We suggest that, based on the seismic interferometry technique, the crosscorrelation gathers of improperly clamped geophones are dominated by tube waves and show very low to non-existing frequencies below which body waves become observable. On the other hand, the crosscorrelation functions associated with relatively better clamped geophones yield a relatively broad frequency range within which retrieved direct body waves are observed. We have applied this technique to four borehole microseismic data sets, A, B, C, and D, of which the data set D was previously known to have some clamping issues reported by the data acquisition company. Compared with the data sets A and D, emergence of body waves over relatively broad frequency range in data sets B and C indicate that the latter borehole arrays have better coupling. For data set D, very low or absent frequencies below which body waves become observable confirm the coupling issues for this data set as noted by the acquisition company.

Tests indicate that conclusions on coupling were maintained even if only 2-min data segments were used taken prior to the start of the hydraulic fracturing treatment. Longer segments led to enhanced body-wave retrievals but did not change the conclusions.

CHAPTER 5

Passive image interferometry for microseismic time-lapse analysis; application to wastewater disposal monitoring

There is an increasing need to obtain comprehensive knowledge about the subsurface and its temporal changes for exploitation of natural resources, storage of waste, or subsurface construction. It is valuable to observe changes of elastic properties like seismic velocity, in particular if the actual spatial perturbation is not known, for instance such as for wastewater disposal wells. Injection and movement of fluids in geologic formations cause changes in seismic velocities and attenuation, resulting in changes in seismic wave scattering and propagation. The changes in seismic velocities in the proximity of the injection well can be associated with changes in fluid saturation, increase in pore pressure, or the opening or enlargement of cracks due to the injection process. The injection process can also induce stress variations beyond the fluid front within the surrounding formations also leading to changes in elastic properties of the rocks.

One of the most common methods for long-term monitoring of reservoirs, CO₂ storage sites, or geothermal energy production is acquiring and analyzing active seismic data, which are costly and not applicable everywhere. Passive methods based on ambient seismic noise receive much attention recently and might, in general, present a more cost effective approach to accomplish the important task of long-term monitoring compared with active seismic time-lapse experiments. We investigate the possibility of passive monitoring of a wastewater disposal well and its surroundings located in British Columbia using ambient seismic noise, which is continuously recorded contrary to active reflection seismic data. We are especially interested in seismic velocity variations induced by reduction of injection pressure in an effort to mitigate the elevated level of seismicity, which is caused most likely due to the injection of large volumes of waste fluid. We use the method of passive image interferometry to

estimate the relative velocity variations from the time shifts measured between consecutive crosscorrelation functions for each station pair in a surface array composed of 5 broadband seismometers. Preliminary results show that among the station-pair paths that are analyzed some represent clear changes of velocities during the period of time of interest when the injection pressures were reduced. The probable driving mechanisms responsible for the velocity increase or decrease coincident with injection pressure changes are reduced pore pressures or lowered poroelastic stresses beyond the injection wellbore, respectively. As opposed to injection pressures, hydrologic data and noise energy trends do not seem to directly correlate with the estimated relative velocity variations.

5.1 Introduction

Passive imaging techniques that use ambient-noise data are based on reconstructions of the Green's function by crosscorrelation of data acquired at two locations, which provides the expression of the wave propagation from a virtual source at one station as recorded at the second one (Weaver and Lobkis, 2001; Shapiro and Campillo, 2004; Wapenaar, 2004; Snieder, 2007). This property has been extensively used to perform noise-based surface wave tomography at observation scales that range from hundreds of kilometers (Shapiro et al., 2005; Yao et al., 2006) down to a few kilometers (Roux et al., 2011). Vaezi and van der Baan (2015) used a similar property to assess the clamping quality of borehole geophones in microseismic experiments. Campillo and Paul (2003) showed that empirical Green's functions can also be obtained from crosscorrelation of the diffuse part of multiply scattered seismic coda. However, these properties hold when the distribution of noise sources is isotropic and/or when a diffuse wavefield is achieved by scattering from random heterogeneities.

For some geophysical applications, such as monitoring of changes in hydrocarbon reservoirs, volcanoes, or fault zones, the major goal is to detect temporal variations in the Earth structure. In addition to surface wave tomography, passive processing based on seismic-noise (auto) crosscorrelation is of growing interest for the monitoring of temporal changes in complex structures, such as volcanoes or fault zones at the geophysical scale (Sabra et al., 2006; Sens-Schönfelder and Wegler, 2006; Brenguier et al., 2008a, 2011; Hadziioannou et al., 2009). The recent passive monitoring investigations find their roots in the early work of Poupinet et al. (1984), who proposed the measurement of small velocity variations using the direct arrivals of earthquake multiplets. This technique, which was originally called the doublet technique in seismology, computes the time delay for two similar signals that originate from the same location and that are acquired at different times at the same position. Time delay is computed by estimating the phase shift in the frequency domain using short time windows centered on the coda of the recorded signals. Indeed, small velocity

changes that have no detectable influence on the direct arrivals are amplified by multiple scattering and can thus be readily observed in the coda. Later on, coda wave interferometry revisited the doublet technique, from repetitive sources (earthquake doublets or repeated artificial seismic sources) in geophysics at higher frequencies and on smaller scales (Snieder et al., 2002; Grêt et al., 2005; Snieder, 2006). To estimate the accuracy of the inferred velocity variations, these techniques use the correlation coefficient, which provides a measure of the similarity of the two time-windowed signals.

The major challenge of coda wave interferometry is that it requires a repeatable seismic source to obtain similar waveforms of the multiple scattered waves in the two seismograms before and after the medium perturbation. Repeated artificial seismic sources as used by Nishimura et al. (2000) and Wegler et al. (2006) are expensive. Repeated earthquakes with almost identical source positions and mechanisms, on the other hand, are rare and there is no control on their occurrence. As a result, although the above studies using coda wave interferometry could detect small changes in the seismic velocity, in general the temporal resolution of the changes is poor and irregular.

The physical and mechanical properties of a stimulated rock mass change in response to the engineering and geotechnical activities associated with mining, hydrocarbon production, hydraulic fracturing, waste storage, CO₂ capture and storage, and heat and water extraction or water injection. Fluid injections can result in changes in the local stress field that can trigger instabilities that lead to increased seismic risk in areas characterized by little or no natural seismicity (Giardini, 2009; Ellsworth, 2013). Monitoring methods applied in reservoir management are mainly based on microseismicity (Shapiro, 2008). The properties of induced seismicity can provide estimates of hydraulic rock properties and local and regional stress fields and real-time assessments of seismic hazard (Shapiro et al., 2007, 2011; Bachmann et al., 2011). However, once a reservoir has matured and percolation networks are established, the induced seismicity greatly decreases, or it ceases altogether, and seismologists can no longer study the reservoir response (Schoenball et al., 2014). This includes aseismic deformation that can indicate potentially unwanted leakage and the corresponding contamination of aquifers (Rutqvist, 2012). For a constant assessment of reservoir properties, it is therefore important to develop and apply tools that perform independently of the spatiotemporally variable seismicity (Julian and Foulger, 2010).

The new idea that arose from passive interferometry after 2005 was to replace the use of repetitive sources by the computation of the seismic-noise correlation function between two sensors. Using this method, the elastic Green's function between two seismometers is constructed as a first step using the crosscorrelation of seismic noise recorded at the two sensors. Then, in a second step, the Green's functions obtained for different times are treated as similar earthquakes and coda wave interferometry is used to extract a temporal variation

in seismic velocity. The technique of passive imaging with noise is well suited to monitor temporal variations of the Earth structure: First, noise data are continuously available, whereas the usually used repeating earthquakes occur in an uncontrolled quasi-random manner. Secondly, the apparent source position corresponding to one receiver position does not change with time. Therefore, in contrast to similar earthquakes, where source positions and source mechanisms are only approximately identical, Green's functions recovered from noise are reproducible even in the late coda. The new technique of combining Green's function retrieval with coda wave interferometry was named "passive image interferometry" (Sens-Schönfelder and Wegler, 2006), because interferometric methods are applied to passive images. Therefore, ambient noise interferometry is also suitable for detecting the temporal change of subsurface structure at high temporal-spatial resolution because ambient noise is recorded at all times and places.

Through laboratory experiments (Hadziioannou et al., 2009), it has even been shown that the monitoring of relative velocity variations through the collection of crosscorrelation functions is possible, even when the exact Green's function is not retrieved from the correlation process. In other words, the requirements to perform passive monitoring are less restrictive than for noise-based tomography. Therefore, noise-based monitoring only requires a stable source distribution in contrast to a complete directional coverage, which is needed for the full convergence towards the Green's function. In reality, the wavefield is not fully diffuse and noise distribution is strongly azimuthally-dependent. These would result in amplitude asymmetries between the acausal and causal parts of the crosscorrelation functions and phase errors in the extracted ballistic waves (Stehly et al., 2006; Yang and Ritzwoller, 2008). Though the resulting velocity bias may be negligible in noise-based surface wave tomography (Tsai, 2009), the apparent phase shift due to a time-varying, nonisotropic noise field can be falsely attributed to the change in subsurface elastic properties. Given the commonly uneven distribution of noise sources, such biased effect can be mitigated by using the coda waves, which have much smaller phase errors owing to long range correlation of more diffuse, multiply-scattered wavefields (Froment et al., 2010). With increasing lapse time, the later coda arrivals which scatter more times and travel longer paths would accrue more observable phase shifts for reliably detecting small temporal velocity changes. In seismological contexts, these principles have been applied to resolve relative velocity changes between $O(0.01\%)$ and (1%) associated with volcanic activity (Brennguier et al., 2008b; Obermann et al., 2013a; Rivet et al., 2014; Duputel et al., 2009), rapid (Wegler and Sens-Schönfelder, 2007; Brennguier et al., 2008a; Wegler et al., 2009; Hobiger et al., 2012; Froment et al., 2013) and slow (Rivet et al., 2011) slip on earthquake faults, water content in the shallow crust (Sens-Schönfelder and Wegler, 2006; Meier et al., 2010; Froment et al., 2013; Hillers et al., 2014), thermal processes (Sens-Schönfelder and Larose, 2008; Richter et al., 2014; Hillers et al., 2015a), and tidal-induced deformation (Hillers et al., 2015b).

Here, we investigate the potential application of the passive image interferometry method to detect, resolve, and monitor long-term velocity variations due to changes in the scattering and mechanical rock properties caused by injection of large volumes of wastewater into a disposal well in northeast British Columbia, Canada. Of particular interest are the perturbations associated with the period when the injection pressure and rate were reduced to mitigate high rates of seismicity and induced earthquakes. The estimated velocity variations ($\frac{\delta(v)}{v}$) are compared with the pumping curves and also with nearby environmental data of wind speed, rainfall, snowfall depth, and atmospheric temperature to clarify the causes of the observed velocity changes. Preliminary results show different behaviors at different station pairs including both sudden decrease or increase of seismic velocities coincident with the time of reduced fluid injection rates and pressures into the reservoir.

5.2 Data set

The data set is the result of a monitoring effort of seismic activity surrounding a disposal well, targeting a porous member of a formation at a depth of approximately 3.2 km, located in northeast British Columbia. The exact locations, injection well identifier, formation names, and the years during which the data were recorded are not mentioned due to confidentiality reasons. The data span over nearly 11 months, starting from late March of the first year (year 1) until early March of the second year (year 2). The formation is of high porosity (and associated permeability) and is often structurally enhanced by faulting. As such, the high porosity/permeability make the formation an ideal candidate for wastewater disposal at well locations exhausted of their primary resource. The increased pore pressure in the rock surrounding injectors may, however, create fault reactivation when favorably oriented and critically stressed faults are nearby.

A seismograph network has been recording seismicity, thought to be related to disposal activities since the start of this project. The low sensitivity and location accuracy of this network, however, is currently insufficient to enable a more precise analysis of event behavior and local structures. With the correlation between increased seismic activity and increased wellhead injection pressure over time a permanent and dense 10 km-radius array of stations surrounding the well (Figure 5.1) was deployed in March of year 1 with the intention of acquiring higher precision seismic data, enabling a more quantitative analysis of event behavior, correlation to injection activity as well as to the structural features in the region. The monitoring array became operational on March 20, year 1, and has detected 103 events of magnitude 1.5 or greater as of February 28, year 2. The efforts to improve the accuracy of the monitoring resulted in better confidence of event distributions and inferred fluid movement. The array consists of five 3C broadband seismometers (G004, G006, G007,

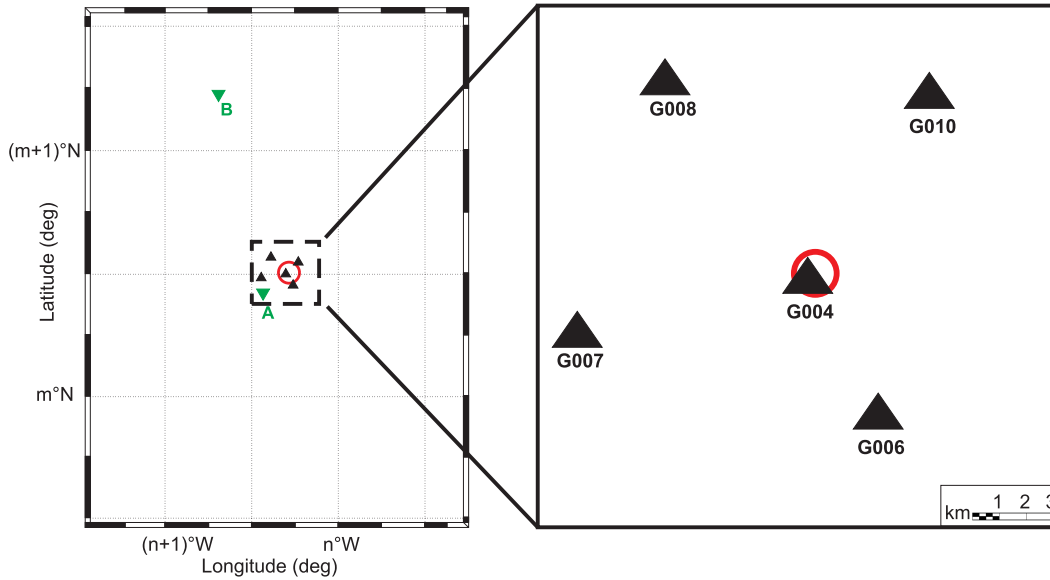


Figure 5.1: (Left) Map showing the location of the study area, as indicated by the black dashed rectangle. The black triangles represent the 5 surface broadband seismometers deployed around a disposal well (red circle). Green triangles denote the location of two climate stations (A and B). (Right) A closer view of the network distribution around the disposal well.

G008, and G010) with natural periods of 20 s distributed around the disposal well and deployed at a depth of 6 m to ensure environmental stability. The sampling frequency of each seismometer is 200 Hz. The central sensor (G004) is located near the wellhead location.

As part of the mitigation efforts, the injection rates and wellhead pressures were reduced by approximately 40% and 10%, respectively, on September 10, year 1 (Figure 5.2a), which resulted in a significant reduction of seismicity in the following months (Figure 5.2b). Figure 5.2b shows that after reducing the injection pressures there is a decreasing trend in both the total number of events and their magnitudes in the following four months. Also, the last three-month period (January-March, year 2) has a fewer number of events compared to any other three-month period.

In this study, we investigate the use of the passive image interferometry method to monitor seismic velocity variations during fluid injection, with particular interest in the period centered around the time when the injection pressure and rate were reduced significantly. We analyze 11 months of vertical-component noise records during the period from late March, year 1 to early March, year 2, which were recorded continuously at the 5 surface broadband stations during fluid injection.

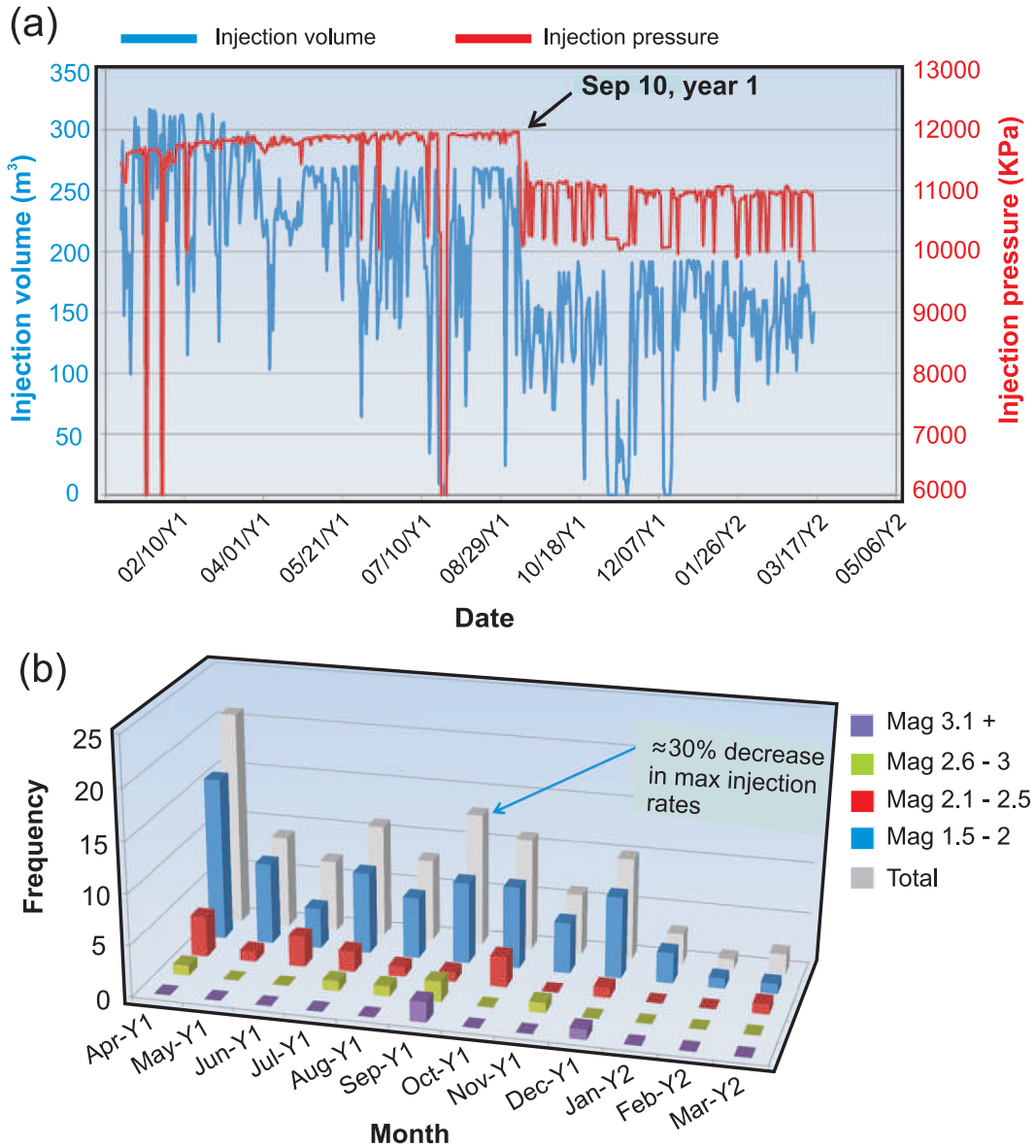


Figure 5.2: (a) Injection pressure and injection volume curves. Y1 and Y2 stand for year 1 and year 2, respectively. September 10, year 1, marks the date when the injection parameters are reduced considerably to reduce seismicity. (b) Monthly event magnitude statistics for the passive monitoring array.

5.3 Crosscorrelation functions

Monitoring the seismic velocity with ambient noise is conducted in two steps. The first step involves extracting the Green's function between two stations by computing the crosscorrelation function of the ambient noise observed at these stations. The second step involves measuring the time delay and the velocity change by comparing two crosscorrelation functions for different time periods. In fact, the retrieved Green's function corresponds to the time derivative of the crosscorrelation function (Gerstoft et al., 2006; Larose et al., 2006). Therefore, it differs from the crosscorrelation function only by a phase shift and a frequency proportionality factor. Since the aim of the method is to detect velocity variations in the reconstructed waveform, it is unnecessary to compute the time derivative of the crosscorrelation function which would enhance high frequencies and may introduce spurious noise (Sabra et al., 2005c).

The quality of noise crosscorrelation functions depends on the data processing choices. Noise preprocessing aims to make wavefield properties more compatible with the characteristics of the theoretically ideal situation of a broadband, equipartitioned state from which estimates of the Green's function can be constructed. Practitioners homogenize the frequency content of the ambient seismic wavefield and attenuate the influence of source-related transients using a range of frequency- and time-domain normalizations (e.g., Bensen et al. (2007)). Having tested different combinations of common preprocessing steps on our data set, we conclude that the following approach provides the most stable and robust crosscorrelation functions: The hourly Z-component data segments at each station are detrended, demeaned, cosine-tapered, and corrected for instrument response to increase the bandwidth over which the crosscorrelation functions are calculated. In order to diminish contamination due to outliers such as earthquake signals and instrumental noise due to data transfer errors, we removed large-amplitude outliers. The daily average level of ambient noise at a seismic station is assumed to be the mean of the RMS amplitude of all 1-hr segments within the day. Any segments including amplitudes larger than 30 times the corresponding daily RMS amplitude are discarded from the analysis. The resulting time series are then spectrally whitened over the broad frequency range of 20 s–10 Hz by setting the spectral amplitudes to 1 for the frequency pass-band between 0.1 and 8 Hz with the amplitudes gradually diminishing to zero at the stop-bands, following a Hanning taper. This means that the time-domain amplitude information is destroyed, but phase information is retained. The whitening procedure also removes power differences between recordings and hence, near-receiver amplitude effects are removed this way. Spectral whitening is necessary to increase the bandwidth of the resulting crosscorrelation functions, prevent spectral peaks to overwhelm the crosscorrelation functions, and therefore equalize the large differences in spectral amplitudes of the signals contributing to the seismic noise in the analyzed frequency range (Bensen et al.,

2007; Groos et al., 2012). Next, we apply temporal normalization to the time series to reduce the effect of earthquakes, non-stationary noise sources, and instrumental irregularities that are not discarded in the previous procedure using RMS amplitude screening of the crosscorrelation functions (Bensen et al., 2007). We use sign-preserving 1-bit clipping for temporal normalization. Crosscorrelation was performed pairwise between the common 1-hr segments for the stations. The hourly crosscorrelation functions were scaled by an estimate of the total power, and they were averaged for daily Green's function estimates. Different band-pass filters are then applied to the resulting daily crosscorrelation functions, which characterize different noise excitation patterns. The velocity variations are then examined in these frequency ranges.

In order to reduce the effect of the noise created at the wellhead, station G004 is excluded from this analysis and the crosscorrelation functions are only calculated for every possible station-pair combinations between the rest of the receivers. For such a relatively dense array of receivers, the inter-receiver distance can act as a limiting factor for the reconstruction of stable Green's functions, especially at lower frequencies. The maximum inter-receiver distance in this array is ~ 15 km between stations G007 and G010. Retrieval of reliable Green's function between two receivers require at least a distance of one wavelength λ between them. Assuming a Rayleigh wave velocity of $v = 2$ km/s (roughly estimated from Figure 5.4b), the maximum low-bound frequency f that can be considered for this high-bound inter-receiver distance is $f = v/\lambda = \sim 0.13$ Hz. Therefore, the crosscorrelation functions calculated between different station pairs are analyzed at the frequencies above 0.2 Hz, that is high enough for the station pair G008–G010, which has the shortest inter-station distance of (~ 10 km) among all analyzed pairs. We are interested in the velocity changes happening at depth. Higher frequency components have a shallower penetration depth compared with the lower frequencies. Therefore, only frequencies up to 2 Hz are considered here. Thus, the frequency intervals over which the crosscorrelation functions are studied are generally limited to ranges that lie within the [0.2, 2]-Hz band.

We calculated spectrograms at different stations to investigate the spectral content of the noise field and its stationarity. Figures 5.3a and b show the daily averaged spectrograms of the vertical component data at stations G006 and G008, respectively, over the entire frequency range of [0, 100] Hz. The spectrograms for other receivers are very similar to these figures. The high-frequency noise (>1 Hz), shows clear seasonal variations with low and high amplitudes during winter and summer seasons, respectively. This trend is particularly evident at station G006, as it is close to a few main roads that generate more noise during the summer time due to more traffic. The low-frequency noise below 0.3 Hz, which is dominated by the second microseismic peak at approximately 0.2 Hz, exhibits the opposite behavior, with high and low intensity during winter and summer seasons, respectively, which is likely due to changes in noise directivity due in response to the seasonal hemispherical shift of

storms.

The noise at the frequency range of $[0.3, 0.8]$ Hz shows the least periodic changes and shifts of peak frequencies. Temporal variations affect the overall amplitude but not the shape of the spectrum significantly. Figures 5.3c and d show the corresponding amplitudes averaged over a frequency band of $[0.3, 0.8]$ Hz. These figures show no significant differences in the variation of the observed ground motions at these stations for almost the entire study period. We therefore expect that the noise sources are excited to a variable degree but their spatial pattern remains fairly stable over time. For monitoring purposes this spectral stability is more important than the higher amplitudes in the microseism band since frequency shifts can introduce artifacts in measurements of velocity variations (Zhan et al., 2013). In other words, this frequency range does not include the ocean microseisms (at 7- and 14-s periods) which usually represent strong annual periodicity, frequency shifts, and well-known changes in the directionality of the noise. Moreover, noise source changes due to traffic and human activities are considerably lower in this frequency band. Also this frequency range is low enough to have adequate sensitivity to variations at depths at the proximity of the reservoir. Despite these observations, in the next section we analyze the velocity variations at different frequency intervals between 0.1 and 2 Hz in order to ensure which frequency range results in most stable estimations of relative velocity variations.

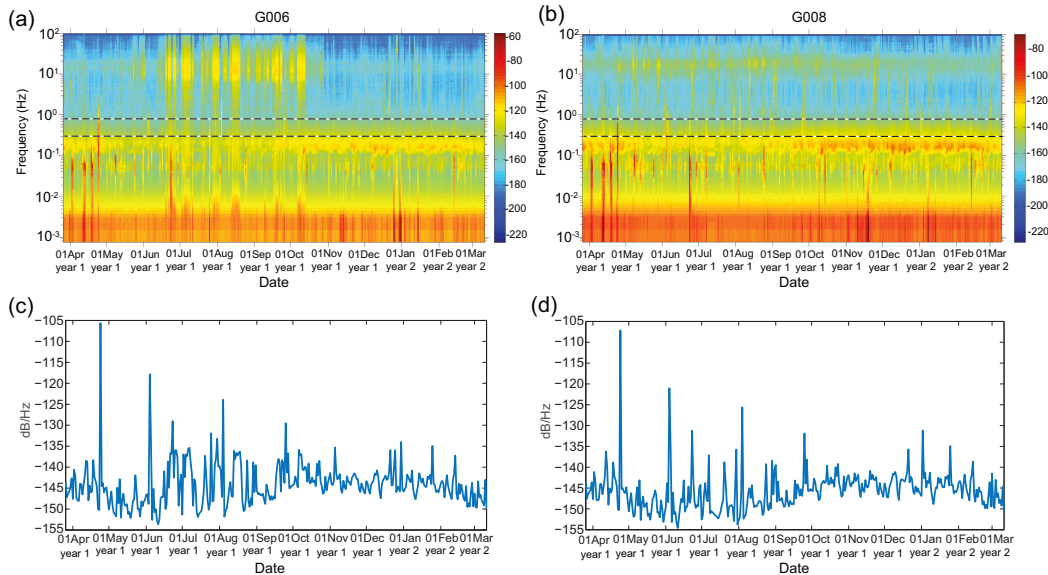


Figure 5.3: (a) and (b) Daily averaged ambient noise spectrogram for stations G006 and G008, respectively. The black dashed lines represent the studied frequency band of $[0.3, 0.8]$ Hz. (c) and (d) The corresponding amplitudes averaged over the frequency band of $[0.3, 0.8]$ Hz.

Accurate measures of velocity variation ($\frac{\delta(v)}{v}$) between a "reference" state and any similar "current" state can be estimated by the time shift measured between their associated cross-correlation functions (section 5.4), calculated over a lapse time that includes sufficiently energetic coda waves (section 5.1) (lapse time refers to the time along the crosscorrelation functions). Here, the reference crosscorrelation function trace (φ^{ref}) is calculated as the stack of all daily crosscorrelation functions in the frequency range of interest. The individual daily crosscorrelation functions are considered as the current traces (φ^{curr}) for each day. This relation between the reference and current traces is based on the assumption that a pure spatially homogeneous velocity variation will lead to an identical stretched or dilated version of the reference waveform by a constant factor. However, this assumption is always going to be violated due to distortions caused by changes in the structural and scattering properties of the Earth's crust, change of sources, or simply because the current correlations are not fully converged to the local Green's functions due to limited duration of the ambient noise being correlated.

The large number of traces involved in the stacking process leads to a reference trace with a high SNR. However, measuring accurate phase variations between the reference and current traces requires a good SNR at the current state too. Since the coda waves strongly contribute to the accuracy of phase variation measurements, the challenge is therefore to obtain a good SNR on this part of the current crosscorrelation functions, that is classically of much lower amplitudes than the direct waves. Indeed, the SNR of the coda waves used to measure $\frac{\delta(v)}{v}$ scales as the square root of the duration of the noise correlated (Sabra et al., 2005c; Larose et al., 2008). Getting a higher temporal resolution requires the use of correlations computed from shorter durations of data. Coda waves are then reconstructed with lower SNR, and the coherency between the reference correlation and the signal (the correlation at a given date) is lower. This implies that the error on the $\frac{\delta(v)}{v}$ measurements increases. That is why, in an effort to improve the SNR and stabilize the crosscorrelation functions, and also to reduce the degree of fluctuations in the velocity variation estimations, we stacked the daily crosscorrelation functions with a moving average window of 31 days, which is shifted 1 day at a time. Therefore, the new 31-day stacked crosscorrelation functions are going to be considered as the current waveforms. However, this approach reduces the temporal resolution. There is an obvious trade-off between the temporal resolution and the precision of the velocity change measurements (Hadziioannou et al., 2011). Different filtering strategies have been applied to crosscorrelation functions to increase the SNR without affecting the temporal resolution, suppress fluctuations, and to mute the biasing of wavefield components (Baig et al., 2009; Stehly et al., 2011), although their application has not become standard.

Figure 5.4 shows an example to clarify how this analysis works. Figure 5.4a shows the resulting 31-day stacked crosscorrelation functions in the frequency range of [0.3, 0.8] Hz calculated for the station pair G006–G008. Seasonal intensity variations are evident within

the direct arrivals but are significantly weaker in the coda part of the crosscorrelation functions. The seismic coda on both the causal and acausal sides of the crosscorrelation functions represent a great level of coherency up to correlation times of nearly 94 s. Figure 5.4b shows the normalized reference crosscorrelation function filtered in the frequency range of $[0.3, 0.8]$ Hz, calculated as a result of stacking all the 31-day stacked crosscorrelation functions. A good level of symmetry between the causal and acausal parts of the reference crosscorrelation function implies an adequately homogeneous distribution of noise sources around the stations at this frequency range. The maximum value of the envelope function calculated for positive amplitudes of the reference crosscorrelation functions (red curve in Figure 5.4b) appears at a lapse time of 7.5 s. Considering an inter-station distance of 15 km between sensors G006 and G008, this represents a Rayleigh wave velocity of ~ 2 km/s. Assuming the relationship suggested by Lowrie (2007), the penetration depth of the Rayleigh waves is approximately 0.4λ . This will translate into a maximum penetration depth of ~ 2.7 km at the lowest frequency of the selected band.

Although the reference stack shows that coda waves have sufficiently high amplitudes above the noise level up to lapse time of 94 s, we consider the lapse-time interval of 15–70 s for the purpose of estimating relative velocity variations (shaded area in Figure 5.4b). The reason behind giving preference to this interval is that the scattered coda waves have sufficient energy in this lapse-time range, considering that arrivals with energy above an asymptotic background level are associated with strong multiply-scattered phases, in contrast to the relatively incoherent noise that dominates the waveforms in the tail. Also, in order to attenuate the effects of temporal variations in the distribution of the noise sources, we ignored the direct waves (before lapse time 20 s), which are highly sensitive to azimuthal distribution of the noise intensity (e.g., Froment et al. (2010)).

5.4 Measurement of the velocity variations

In order to obtain stable estimations of relative velocity variations a grid search approach is undertaken. In this approach, different combinations of frequency and lapse-time intervals are investigated for the crosscorrelation functions calculated for each station pair at both their causal and acausal sides. The frequency band and the lapse-time interval that result in the most stable estimations are selected.

We use two different methods to estimate the time shifts and consequently the relative velocity variations between a reference trace and each current trace (31-day stacked crosscorrelation functions) at each lapse-time and frequency interval at either causal and acausal parts of the reconstructed crosscorrelation functions. These two methods are the time-domain "stretching" technique (Lobkis and Weaver, 2003; Sens-Schönfelder and Wegler, 2006) and

the frequency-domain "doublet" (Poupinet et al., 1984) or "moving window cross-spectral" technique (Brennguier et al., 2008a,b; Clarke et al., 2011). These two techniques use waveform correlation (Knapp and Carter, 1976) and coherence (Carter, 1978) for time-shift measurements, respectively.

These methods perform differently in the presence of possible wavefield fluctuations. Theoretical and laboratory studies have shown that the stretching method is more stable to fluctuations in noise than the doublet technique (Hadziioannou et al., 2009). However, Zhan et al. (2013) have demonstrated that the temporal variability of noise frequency content at different time scales may cause apparent velocity changes if the stretching method is used. In this work, we apply both methods to diagnose the possible bias in the results introduced by the methodology.

The stretching method, which has some similarity with the dynamic time warping technique (Herrera et al., 2014; Herrera and van der Baan, 2014), is based on the concept that a spatially homogeneous velocity variation in the medium will result in a stretching or compression of the time axis by a factor of $t \rightarrow t(1 - \varepsilon)$, when compared to the reference trace. For this method, coda waveforms at each datum (current trace φ^{curr}) are dilated by a negative or positive factor ε that optimizes the similarity (correlation $CC(\varepsilon)$) between the distorted waveform and the reference signal (φ^{ref}):

$$CC(\varepsilon) = \frac{\int_{t_1}^{t_2} \varphi^{curr}[t(1 - \varepsilon)]\varphi^{ref}[t]dt}{\sqrt{\int_{t_1}^{t_2} (\varphi^{curr})^2[t(1 - \varepsilon)]dt \int_{t_1}^{t_2} (\varphi^{ref})^2[t]dt}}, \quad (5.1)$$

where t_1 and t_2 are the start and end time of the coda used. The dimensionless coefficient $\varepsilon = \frac{\delta(v)}{v} = -\frac{\delta(t)}{t}$ is referred to as the apparent velocity change and $CC = \max(CC(\varepsilon))$ as waveform correlation.

One drawback is that this amounts to assuming a linear behavior for δt versus t , equivalent to a homogeneous relative velocity change $\varepsilon = \frac{\delta(v)}{v}$. Sometimes, this is not the case in complex media. However, this technique also has a noticeable advantage: the whole coda is processed at once, which is found to generally result in a more stable, and thus more precise, estimation of ε . In particular, Hadziioannou et al. (2009) showed from laboratory experiments that the stretching technique is more adapted to data with low SNR. Another interesting feature of the stretching technique is that it provides the remnant correlation CC . This correlation indicates if noise sources are stable or changing over the period of observation of interest: $CC \sim 1$ means absolutely stable sources, $CC \ll 1$ means that the source locations are changing. CC also indicates the quality of the ε estimation.

The precision with which a dilation coefficient ε is retrieved depends on the strength of correlation between two signals. Weaver et al. (2011) derived an expression to predict the

fluctuations in dilation coefficient due to e.g. changes in the noise source, in the case where the velocity in the medium has not changed. The goal is to evaluate the precision with which wave speed changes can be evaluated. To do this, they consider the case in which two waveforms differ only by noise so that the actual relative dilation, without noise, is zero. They then look for the apparent (nonzero in general) value of ε at which the corresponding CC in equation 5.1 achieves its maximum. Equation 5.2 gives the RMS of this apparent, and erroneous, relative dilation:

$$rms(\varepsilon) = \frac{\sqrt{1 - CC^2}}{2CC} \sqrt{\frac{6\sqrt{\frac{\pi}{2}}T}{\omega_c^2(t_2^3 - t_1^3)}}, \quad (5.2)$$

where T is inverse of frequency bandwidth and $\omega_c = 2\pi f$ is the central frequency. For the parameters selected in Figure 5.4 this leads to an $rms(\varepsilon)$ evaluated by

$$rms(\varepsilon) = 2.4 \times 10^{-3} \frac{\sqrt{1 - CC^2}}{2CC}. \quad (5.3)$$

If the dilation measured exceeds this RMS value, we can conclude that it is indeed due to a velocity change in the medium and not loss of coherence in the crosscorrelation function.

The doublet technique was first developed by Poupinet et al. (1984). It is also known as cross-spectral moving window technique (Frechet et al., 1989). Similar to the stretching technique, the doublet method also requires the computation of a reference crosscorrelation function. Then, the cross spectrum between the current and reference crosscorrelation functions for a series of overlapping time windows is computed and the spectral phase shift at different frequencies is measured. For each small time window, the time delay between the current and the reference crosscorrelation function can be found by a weighted linear regression of the phase of the cross spectrum within the frequency range of interest. By repeating this procedure for all the small time windows considered, the time delay as a function of time along the crosscorrelation function can be estimated. Then, the resulting velocity perturbation can be obtained as the slope of a linear regression applied to the time-delay measurements. This procedure assumes that the seismic-wave propagation velocity is perturbed homogeneously within the studied media. The computational details of the doublet technique are fully described in Clarke et al. (2011). The key parameter in this analysis is the Fourier transform window length, which is the time window over which the time delay is measured. On the one hand, large time windows include more data, thus averaging down the fluctuations of time shifts due to noise. This results in more accurate measurements. On the other hand, the approximation that the time shift is constant within the given time window is getting more erroneous when the window length is increased. The choice of the window length is therefore a trade-off between time shift

accuracy and the time resolution between two consecutive measurements. This processing found remarkable applications in seismology, including recent developments in ambient noise seismology (Brennguier et al., 2008a,b). The average velocity-change errors for the doublet method are computed using the estimates of Clarke et al. (2011).

5.5 Results

As an example, Figure 5.5 shows the apparent relative velocity variations estimated using both the stretching and doublet methods calculated for the crosscorrelation functions of the station pair G006–G008 filtered at the frequency range of [0.3, 0.8] Hz and over the lapse-time interval of [15, 70] s (Figure 5.4), along with their associated errors and coherency measurements. We used 90% overlapping, 10-s long lag-time windows for the doublet method. The $\frac{\delta(v)}{v}$ estimates from both methods are very similar. For the doublet technique, the similarity (coherency) estimate (Clarke et al., 2011) is associated with the two original waveforms that have not been corrected for the potential travelttime change, and is therefore generally lower. The coherency measures of greater than 0.75, low error values compared with the relative velocity changes themselves, and consistency of results obtained with the two techniques are indicative of robust estimates, because they perform differently in the presence of noise fluctuations (Hadziioannou et al., 2009; Zhan et al., 2013; Hillers et al., 2015a,b; Knapp and Carter, 1976).

However, the similarity of the results from the two techniques rarely happens for other frequency ranges and lapse-time intervals at most of the station pairs. Tests show that the doublet method provides much stabler estimations than the stretching technique. This is shown in an example in Figure 5.6. For each technique, the relative velocity variations calculated for several consecutive time windows of 50-s length at the causal part of the crosscorrelation functions and at the frequency range of [0.3, 0.8] Hz are averaged. The first time window starts at a lapse time equal to 10 s. A moving step of 2 s is considered between consecutive analysis windows. The standard deviations at each date are also calculated from estimations at different lapse-time windows. Figure 5.6a and b show the results obtained by the stretching and doublet methods, respectively. The black curves show the mean velocity variation estimation and the gray areas show the associated standard deviations. Smaller standard deviations suggest that generally the results from the doublet technique are significantly stabler than those obtained by the stretching method. Similar observations are made for frequency ranges other than [0.3, 0.8] Hz. Thus, we only use the doublet technique for velocity variation estimations in this data set hereafter. Note that in the doublet method, small standard deviations compared with the average estimate suggests that different time windows result in similar velocity variation estimations. Therefore, we

consider the mean values as a good representative estimation of velocity variations at each frequency range.

Another observation is that the velocity variations for some of the station pairs seem to show somewhat opposite behaviors between the causal and acausal estimates, which suggests that the causal and acausal parts of the crosscorrelation functions shift in the same direction in time. It is not clear what can cause such behavior. However, a clock error between the stations can explain this (Gouédard et al., 2014; Sens-Schönfelder, 2008; Stehly et al., 2007). Figures 5.7 and 5.8 show two such examples for the velocity variations estimated for the station pairs G006–G008 and G008–G10, respectively, in the frequency range of [0.3, 0.8] Hz. This is more evident in the later part of the Figure 5.8. In fact, all the station pairs that include the receiver G010 suffer more from this behavior when compared with other station pairs. This is due to the significant shift of the crosscorrelation functions on January 10, year 2 for these station pairs. Figure 5.9 shows the crosscorrelation functions used to estimate the velocity variations plotted in Figure 5.8. A closer view in the bottom figure shows a clear and sudden shift of the crosscorrelation functions at both the causal and acausal parts towards the negative lags on January 10, year 2, which is denoted by a black arrow.

With our grid search approach, we have also analyzed the crosscorrelation functions at different frequency bands in order to find the best representative frequency range with the most stable velocity variation estimates that are more likely to show the effect of the injection pressure changes. The frequency ranges that are considered include [0.1, 0.4] Hz, [0.2, 0.5] Hz, [0.3, 0.8] Hz, [0.4, 0.9] Hz, [0.5, 1] Hz, and [0.7, 2] Hz. Figure 5.10 compares the relative velocity variations estimated from the acausal part of the crosscorrelation functions for the station pair G007–G010 for three different frequency ranges [0.1, 0.4] Hz, [0.3, 0.8] Hz, and [0.7, 2] Hz. Note that the results measured for the dates after the strong sudden shift on January 10, year 2, have been removed for clarity. This figure shows that at lower frequencies of [0.1, 0.4] Hz the estimated velocity variations show a large degree of fluctuations and therefore large standard deviations. The use of a longer smoothing window than 31 days could have reduced these fluctuations. However, this would have led to lowered resolutions too. The result from the frequency range of [0.3, 0.8] Hz, on the other hand, shows more stable behavior and lower errors and seems to highlight some identifiable velocity changes at around September 10, year 1, that is when the injection pressures were reduced significantly and are more of interest in this study. The results from the higher frequencies of [0.7, 2] Hz are also stable but they hardly show any amount of variations that can be attributed to the injection pressure changes in the reservoir. This can be explained by the shallower depth of penetrations of the Rayleigh waves at these frequencies compared with the depth where the direct effects of pressure changes can reach to. Therefore, mainly the frequency range of [0.3, 0.8] Hz is considered for the analysis of the velocity variations hereafter.

Figures 5.11a–f show the relative velocity variations estimated for different station pairs using the doublet method at the frequency range of $[0.3, 0.8]$ Hz from the causal part of the crosscorrelation functions. Each curve represents the mean value of the velocity variations measured over the several selected lapse-time windows in the codas. Note that for the station pairs that include receiver G010, the velocity variation measurements for the dates after January 10, year 2, have been removed for clarity. Also, the average value is subtracted from measurements at each station pair so that the fluctuations occur around zero variation. The station pairs G006–G008, G007–G008, and G008–G010 show more identifiable velocity changes than other pairs at around September 10, year 1, which is the time when the injection pressures were significantly reduced in the reservoir. The results from the acausal part (not shown) are rather different and in some cases they show opposite behavior with respect to the ones from the causal part of the crosscorrelation functions. However, station pairs G006–G008, G007–G008, and G008–G010 seem to show more velocity variations than in the other pairs in the acausal part as well.

Two broad categories can be responsible for the derived seismic velocity variations. The results can reflect changes in material properties, or may be induced by changes in wavefield properties including source-related fluctuations that bias the measurements. In order to investigate this, the observed velocity variations are compared with the environmental observables including wind speed, temperature, rainfall, and snow depth (Figure 5.11g and h), as variations in meteorological conditions may cause changes in the mechanical properties of the Earth’s crust. The velocity variations are also compared with the measured noise energy (Figure 5.11i) and pumping curves including injection pressure and injection rate variations (Figure 5.11j). The temperature and wind speed data are collected from climate station A (Figure 5.1) near the study area (~ 11.6 km from the wellhead location), and the rainfall and snow depth are extracted from the station B (Figure 5.1), which is located at ~ 86.4 km toward northeast of the wellhead location. The noise energy is a proxy for source variability and estimated from the average of daily RMS amplitudes at all the considered stations calculated in the frequency range of $[0.3, 0.8]$ Hz.

The observed velocity variations cannot be attributed to seasonal variability as one expects to observe relatively higher velocities during the northern hemisphere winter months when compared with the summer months. We could not recognize clear seasonal signals such as annual or semiannual variations. There are studies showing the effect of the rainfall on reducing the velocities (Sens-Schönfelder and Wegler, 2006) and snow loading on increasing the velocities (Hotovec-Ellis et al., 2014). However, no such relationships are observed here. Also no clear relationship between the velocity variation and the estimated noise energy, wind speed, and temperature data can be established.

However, the velocity variations from the station pairs G006–G008, G007–G008, and G008–

G010 seem to show some correlations with the pumping parameters, especially injection pressure (Figure 5.11j). Although some station pairs show different behaviors in velocity variations in terms of whether velocities increase or decrease near September 10th, especially between causal and acausal parts, still the fact that there is some clear and sharp velocity variations around this time suggests that injection pressure changes may be responsible for such variations. Different interpretations can be provided for either velocity increase or decrease coincident with injection pressure changes on September 10th. A velocity decrease can be explained by stress variations in the surrounding formations further away from the injection point due to poroelasticity effects (Figure 5.12). An increased pore pressures in the proximity of the well can push the grains close together in areas beyond the injection point, leading to crack closure and pore space reduction, therefore, causing the seismic velocity to increase in these areas (Figure 5.12b). A sudden reduction in the injection pressures will lead to sharp stress relief in these regions and cracks re-opening, hence, velocity reductions (Figure 5.12c). As the injection process continues the seismic velocities start to rise back up again (Figure 5.12d). However, the reduced resolution due to using 31-day moving stacks hinders observing exact one-to-one relationships between the injection pressure and the apparent seismic velocity variations.

On the other hand, a velocity increase may be explained by the fact that reduced injection pressures will lead to reduced pore pressures. This results in higher effective stress levels that can in turn result in increased velocities. However, the speed with which the pore pressure changes can diffuse through the medium challenges this interpretation. The pore pressure diffusion can take months or even years to be felt at large distances from the injection well (Keranen et al., 2014), especially for the station pairs that do not cross the area surrounding the wellbore, including G008–G010 that shows velocity increases.

Note that both the stretching and doublet methods assume homogeneous velocity variations between the stations. Therefore, they are more sensitive to global velocity changes than very local variations. This might be why the observed velocity variations mainly show a causal relationship with stress variations on a large scale as opposed to local pore pressure changes nearby the injection point. In this case, recording a large number of microseismic events in the proximity of stations G006 and G008 suggests that a large area between these stations might be affected by effective stress variations, which in turn affect the likelihood of triggering shear slippage and larger magnitude events.

5.6 Discussions

Here we have used 31-day sub-stacks of crosscorrelation functions to obtain high-SNR current traces, and therefore, reduce fluctuations in the velocity variation estimations. This

need for long averages might be problematic though if we would like to follow short-term variations in addition to the long-term ones, especially for the lower frequencies. Baig et al. (2009) introduced an adaptive filter calculated based on the S transform for improving the SNR of the noise correlations, thereby increasing the temporal resolutions.

In general, crosscorrelation means to correlate the signals of two distinct stations. In this case, the first station acts as a virtual source and the Green's function describes waves leaving the first station, traveling around and finally arriving at the second station. A crosscorrelation function thus includes both direct waves and singly- or multiply-scattered waves. Waves traveling from the second station to the first station are measured in negative times. In the limit as the two stations are coincident, the cross-correlogram becomes the auto-correlogram for a single station that yields the seismic response for a coincident source and receiver position. An autocorrelation function does not exhibit direct waves, but only singly- and multiply-scattered waves. There are similar studies that also use autocorrelation functions to estimate relative velocity variations (Sens-Schönfelder and Wegler, 2006; Ugalde et al., 2014). As modern seismic sensors have three independent components, it is also possible to combine autocorrelations and crosscorrelations by crosscorrelating the different sensor components, as was for example applied by Wegler et al. (2009) or more recently by Zhao et al. (2012). It is possible to improve this method by whitening the signals spectrally before crosscorrelating the different sensor components. This improved processing technique is called single-station crosscorrelation by Hobiger et al. (2014).

According to theory (Gouédard et al., 2008; Froment et al., 2010; Paul et al., 2005), we expect any strongly directive and varying part of the noise field to influence the Green's function reconstruction negatively, and thus alter the $\frac{\delta(v)}{v}$ measurements. In order to establish if any such strong moving sources exist around the array, the structure and evolution of the ambient noise field can be investigated with plane-wave beamforming applied to the recorded data (Roux, 2009) or azimuthal analysis applied to the crosscorrelation functions (Stehly et al., 2006). The latter method may not be very effective here due to limited number of sensors. The directionality of the noise can also be investigated with the single-station approach introduced by Gassenmeier et al. (2015), which is based on the estimation of propagation direction of the Rayleigh waves in the ambient noise field using the coherence of horizontal and vertical ground motion.

Although the sensors in this study are synchronized by GPS systems, observation of opposite behaviors in the relative velocity variations between the causal and acausal parts of the crosscorrelation functions can be due to clock errors, which can lead to shifting of the crosscorrelation functions at both sides towards similar direction in time. Apart from this that the velocities are increased or decreased, the fact that large velocity variations are observed for some station pairs around September 10th suggests that these changes can be

due to physical changes in the subsurface, including stress or pore pressure variations caused by injection pressure changes.

Different combination of station pairs can be analyzed to investigate spatial dependency of the coherency and velocity variations. Although the sensor array in this study comprises 5 seismometers only, to further study the material responses, we can still invert the relative velocity variations ε and coherency CC measurements to image the medium changes and therefore, localize changes horizontally, and also constrain the depth of the changes. The spatial dependency can be used to constrain the extent of the medium changes in the horizontal plane with an inversion procedure based on probabilistic approaches (Obermann et al., 2013a, 2014), where ε and coherency CC are related to local medium perturbations using the sensitivity kernels introduced by Pacheco and Snieder (2005), Larose et al. (2010), and Planès (2013). Figure 5.11 shows that the station pairs that cross the areas toward the northern and western sides of the injection well represent more velocity variations than other pairs. This can be explained by higher permeabilities or stress communications towards these areas.

For the vertical direction, following the assumption that the coda waves are dominated by Rayleigh waves, several studies have used the frequency-dependent depth sensitivity of Rayleigh waves to estimate the depth of the velocity changes (Rivet et al., 2011; Mainsant et al., 2012). Obermann et al. (2013b) showed that the depth sensitivity in the early time windows of the coda is dominated by surface waves and in later time windows dominated by body waves, which leads to the possibility to discriminate between changes close to the surface and changes at depth. Lowrie (2007) estimate an approximate maximum penetration depth of 0.4λ for surface waves, where λ is the wavelength. Assuming a Rayleigh wave velocity of 2 km/s in the region and the considered frequency band of [0.3, 0.8] Hz, it yields an approximate penetration depth range of [1.0, 2.6] km. Although we analyzed even lower frequencies that are more sensitive to the medium at the reservoir level, high level of fluctuations in the estimated velocity variations hinders us from studying these changes further. These fluctuations can be reduced using a longer smoothing window length than 31 days, but this will reduce the resolution of the analysis and therefore has limited application in this study.

5.7 Conclusions

We have investigated the potential application of passive image interferometry method to monitor relative velocity variations in a wastewater disposal well. A grid search approach with a parameter space including different frequency ranges, different station pairs, and

several lapse-time windows in the coda, was considered in this study to provide a comprehensive analysis of the velocity variations. There are differing behaviors observed for different station pairs and between estimates from the causal and acausal parts of the cross-correlation functions. However, the fact that clear velocity changes are observed for some station pairs that are coincident with the time when the injection pressures were reduced significantly suggest that the latter may have caused some physical changes in the medium to have resulted in such changes in the velocities. Poroelastic stress changes and pore pressure variations can be responsible for the observed velocity variations, depending on whether velocities increase or decrease.

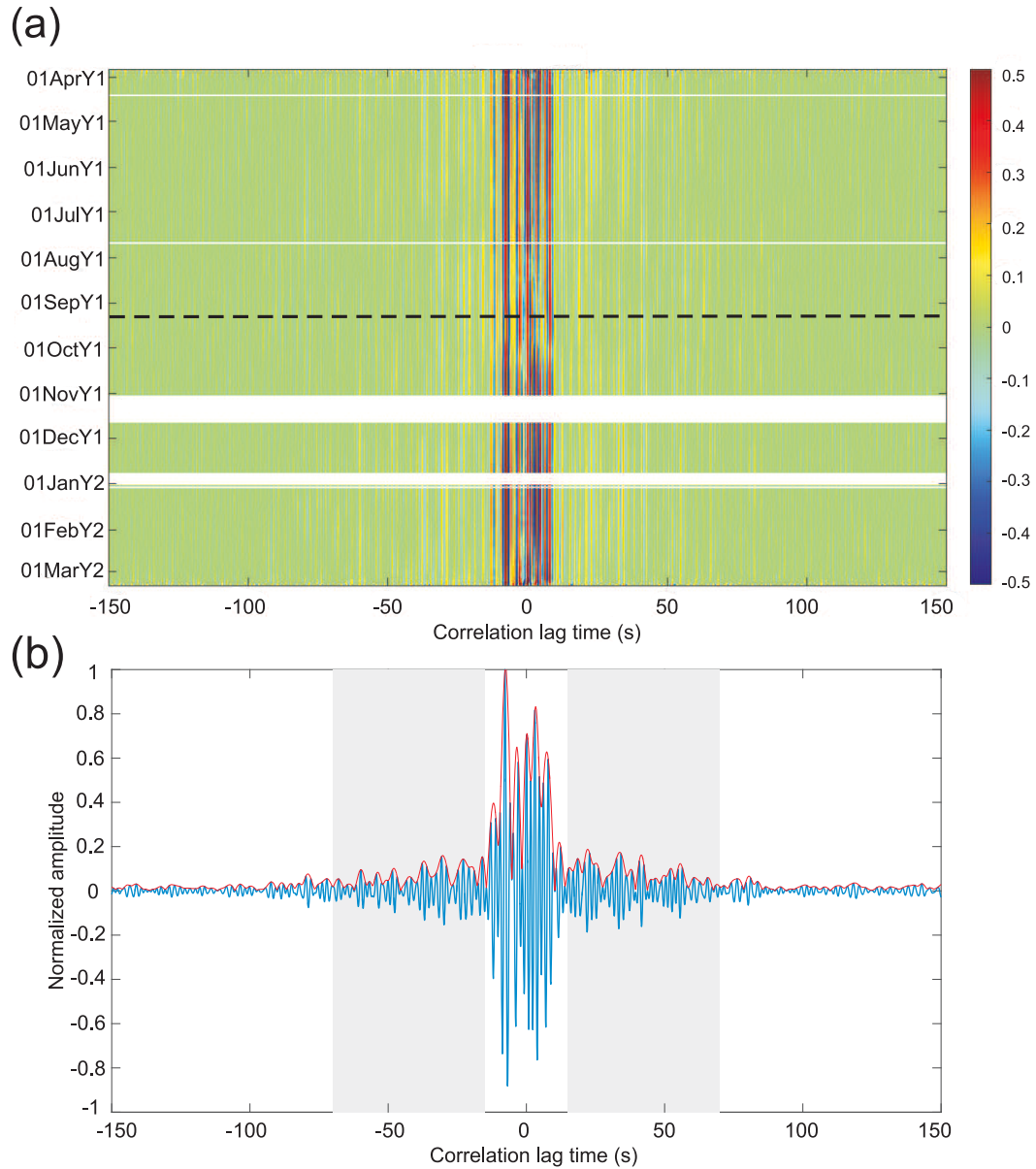


Figure 5.4: (a) 31-day stacked crosscorrelation functions filtered in the $[0.3, 0.8]$ Hz frequency band computed between stations G006 and G008, separated by ~ 15 km. The amplitudes are normalized. Low-quality crosscorrelation functions are discarded from the analysis (white areas). The black dashed line represents the time at which the injection pressure and rate were reduced significantly (Figure 5.2). (b) Reference correlation, which is the sum of all daily crosscorrelation functions in the frequency range of $[0.3, 0.8]$ Hz. Shaded areas are considered for velocity variation analysis. The red curve is the envelope function.

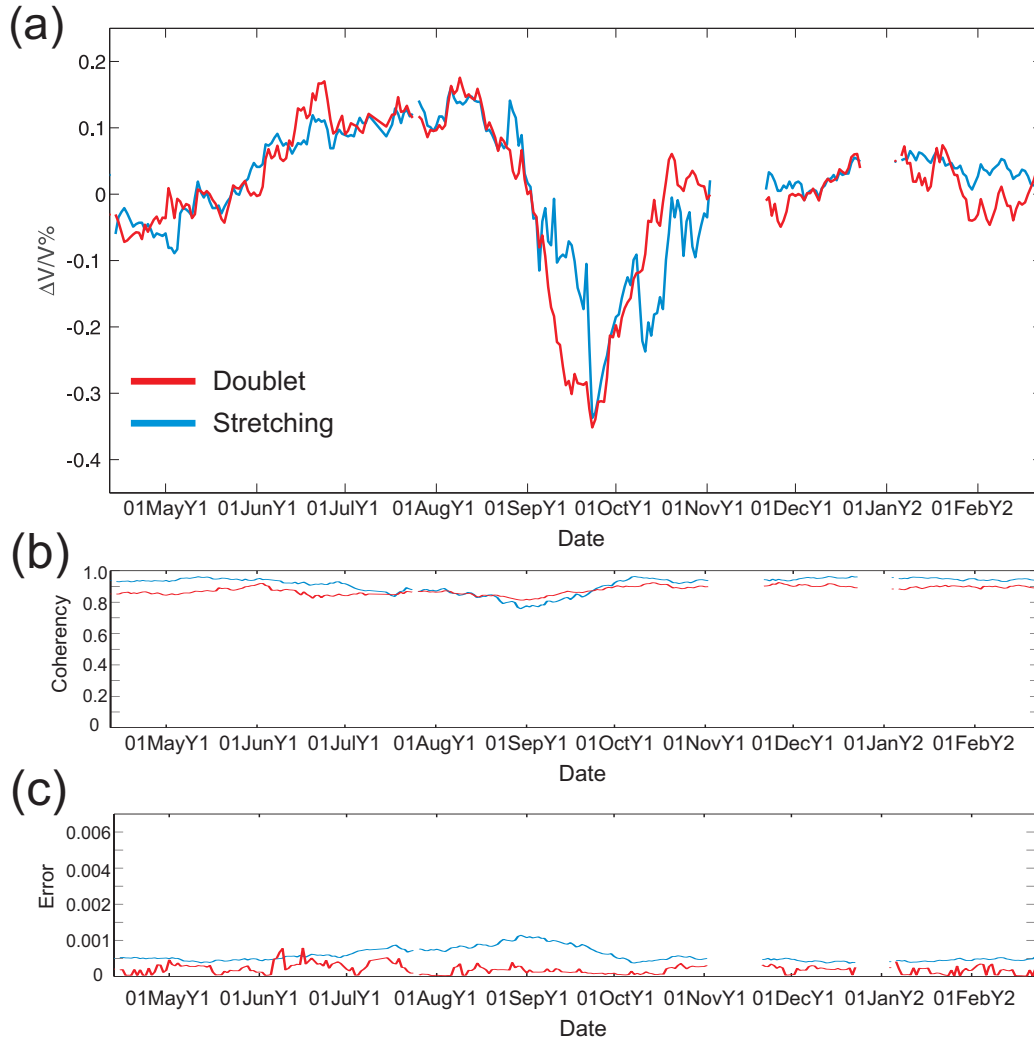


Figure 5.5: (a) Relative velocity variations calculated using stretching (blue) and doublet (red) methods in the frequency band of $[0.3, 0.8]$ Hz at the lapse-time interval of $[15, 70]$ s in the causal part of the crosscorrelation functions (Figure 5.4b). (b) and (c) The associated measured coherence and errors, respectively.

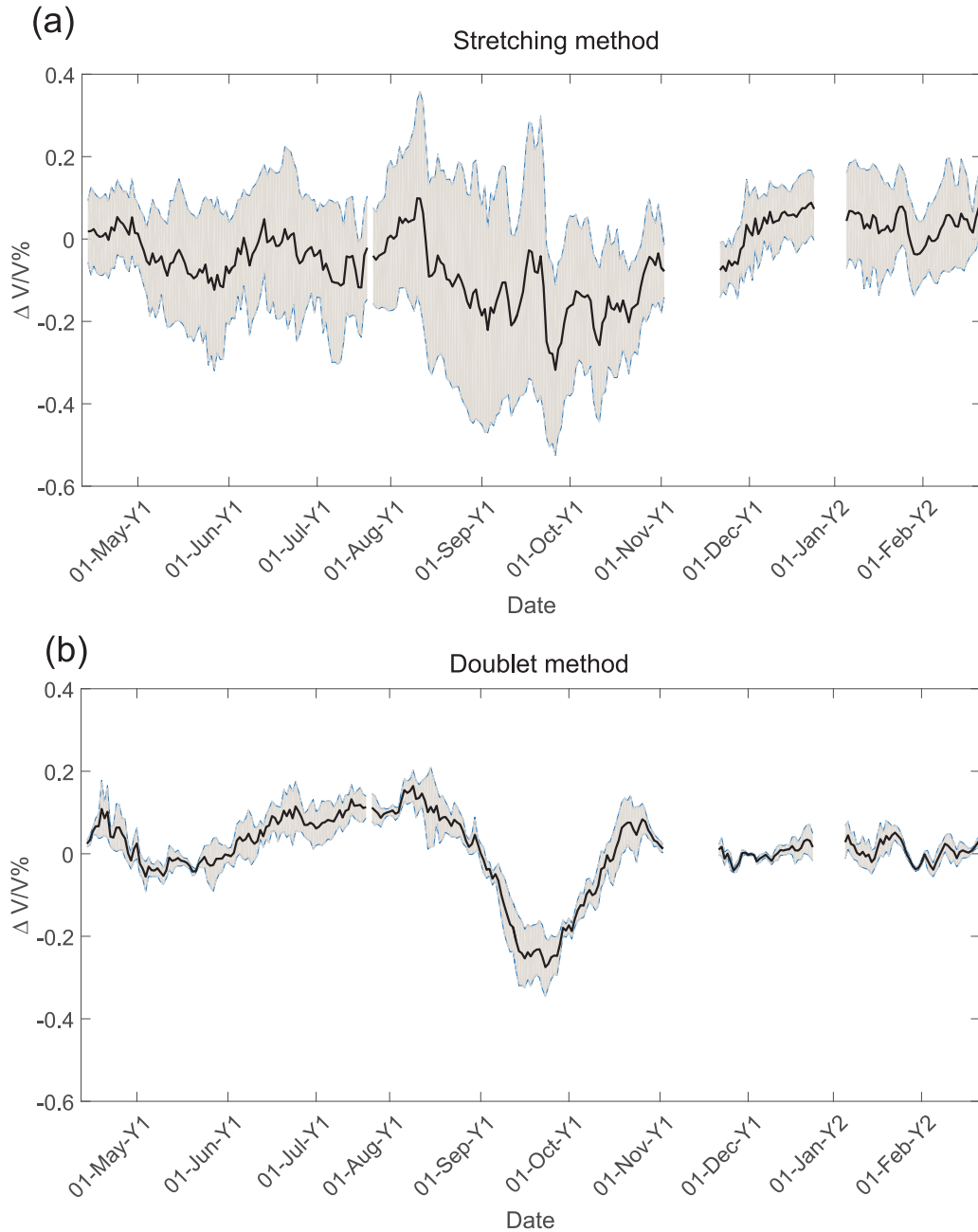


Figure 5.6: (a) The black curve is the mean of relative velocity variation estimated using the stretching technique over different 50-s long windows at the causal part of the crosscorrelation functions for the station pair G006–G008 in the frequency range of [0.3, 0.8] Hz. The gray areas depict the standard deviations of the estimations from different time windows. (b) Similar to (a) but calculated by the doublet method.

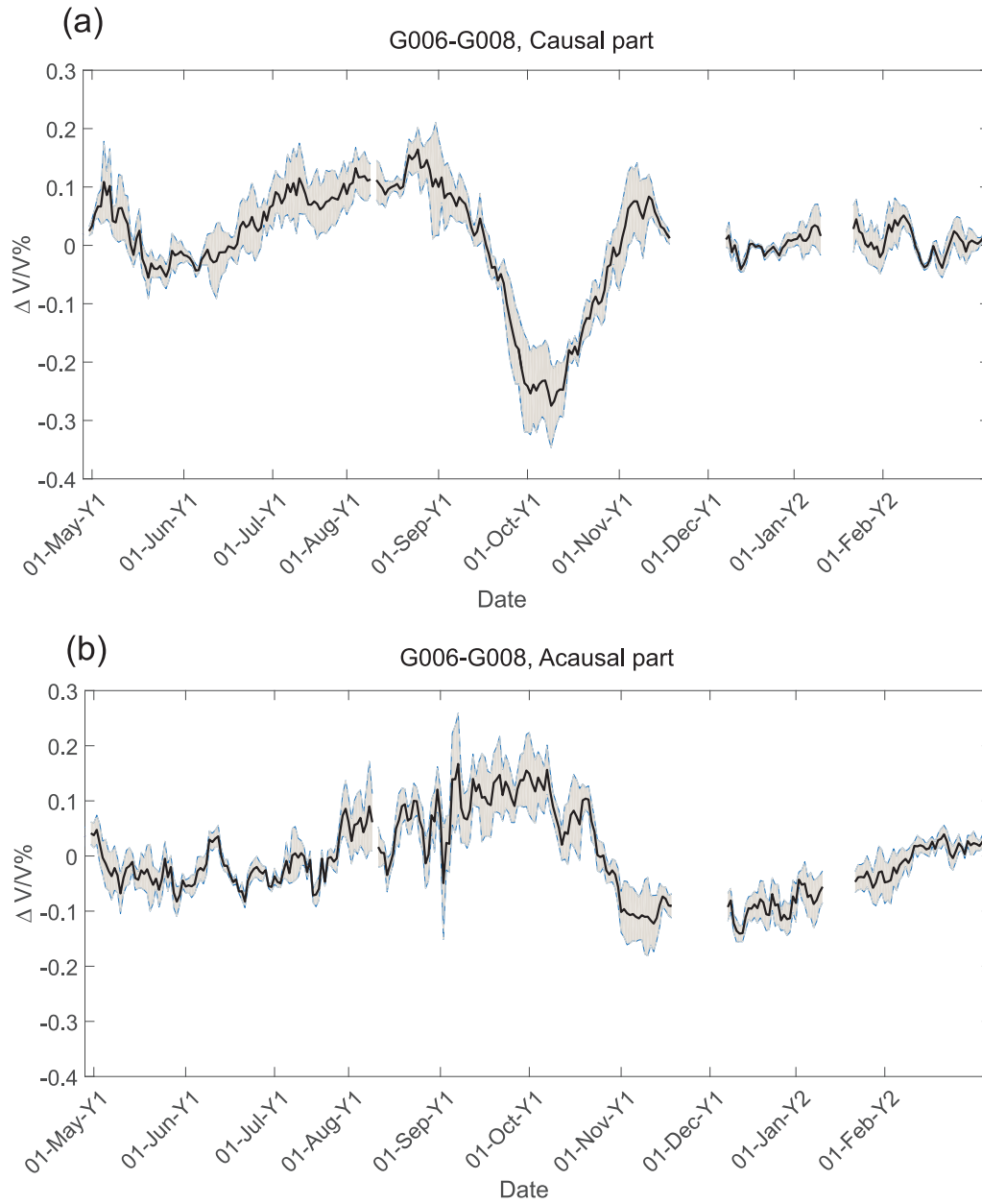


Figure 5.7: (a) The relative velocity variation estimated using the doublet technique from the causal part of the crosscorrelation functions for the station pair G006–G008 in the frequency range of [0.3, 0.8] Hz. (b) Similar to (a) but calculated from the acausal side of the crosscorrelation functions.

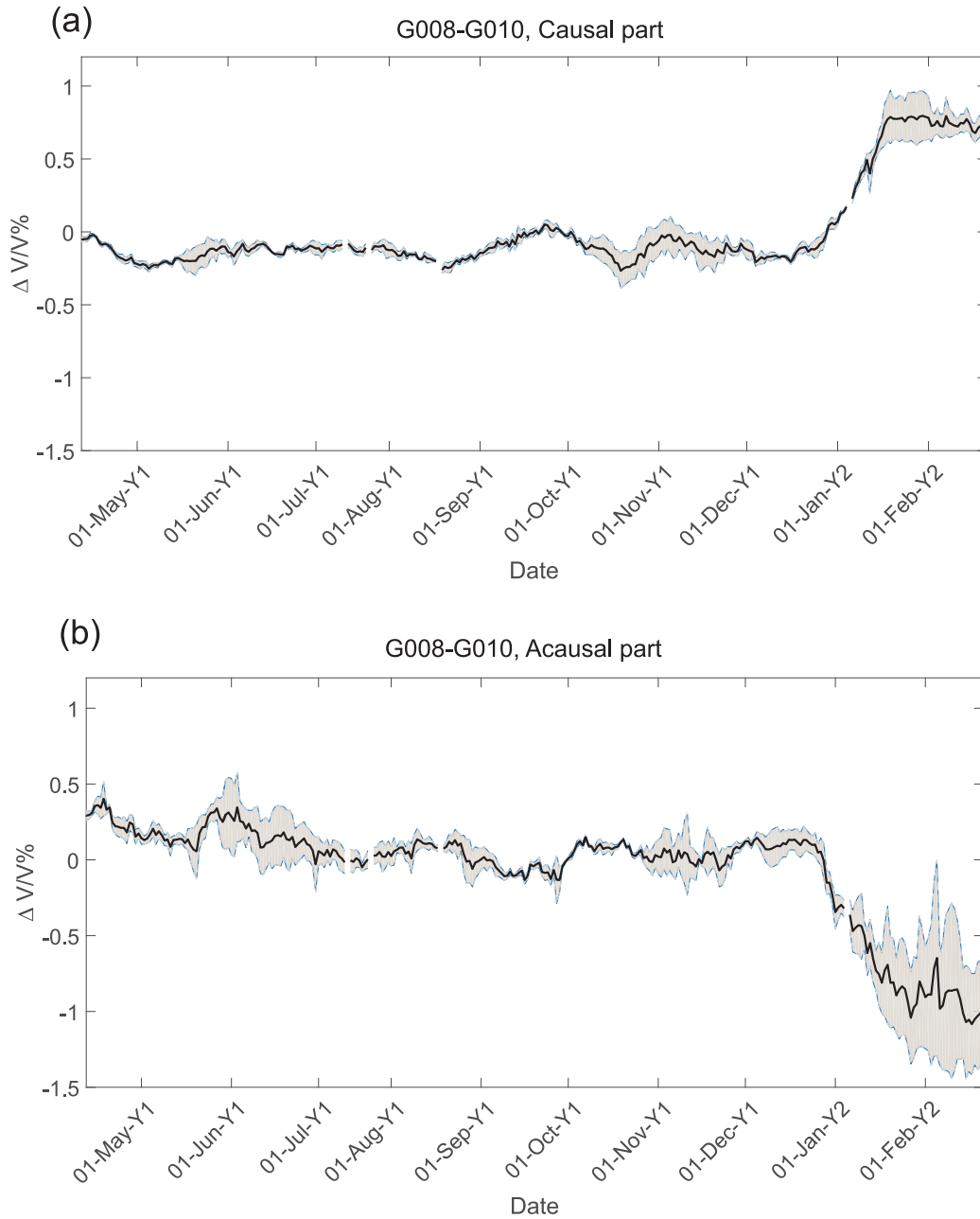


Figure 5.8: (a) The relative velocity variation estimated using the doublet technique for the causal part of the crosscorrelation functions for the station pair G008–G010 in the frequency range of [0.3, 0.8] Hz. (b) Similar to (a) but calculated from the acausal side of the crosscorrelation functions.

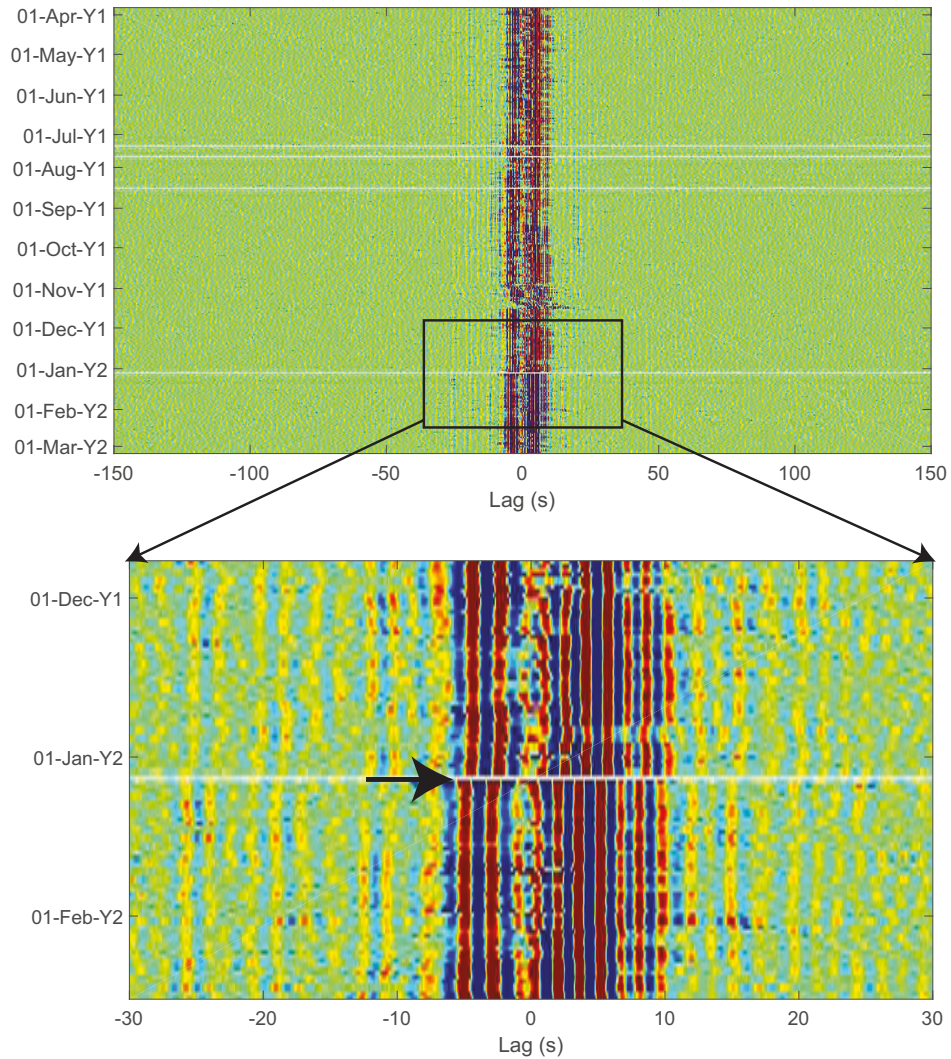


Figure 5.9: The sharp shift toward the negative lags in the crosscorrelation functions measured for the station pair G008–G010 in the frequency range of $[0.3, 0.8]$ Hz, which is responsible for the strong opposite behavior between the relative velocity variations for the causal and acausal parts shown in Figure 5.8. The top figure shows the entire crosscorrelation functions in the lag interval of $[-100, 100]$ s while the bottom figure depicts a zoom-in around January 10, year 2, that is when the sudden shift in crosscorrelation functions occurs. The black arrow points to this time.

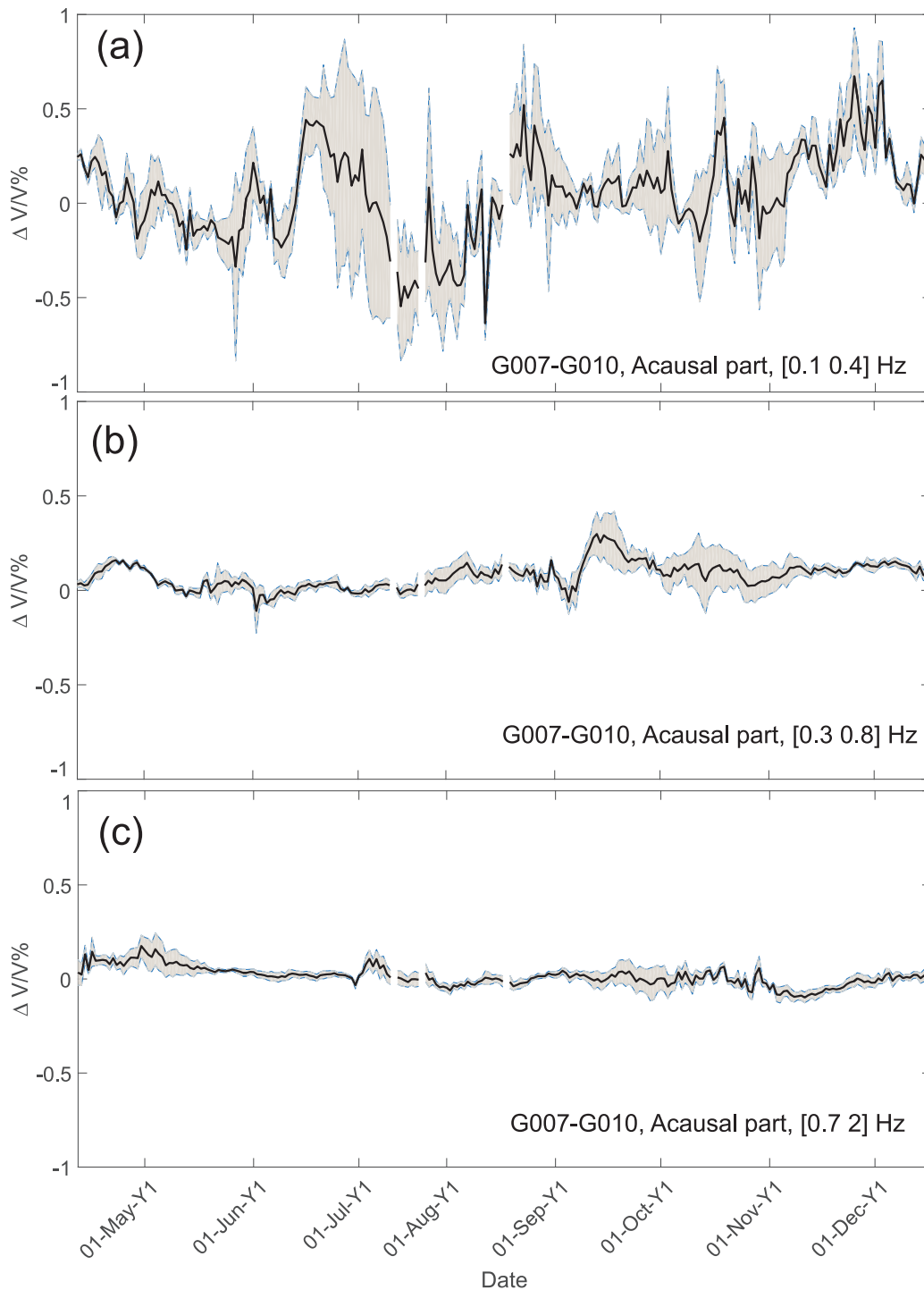


Figure 5.10: The relative velocity variations estimated from the acausal part of the crosscorrelation functions calculated for the station pair G007–G010 at the frequency range of (a) [0.1, 0.4] Hz, (b) [0.3, 0.8] Hz, and (c) [0.7, 2] Hz.

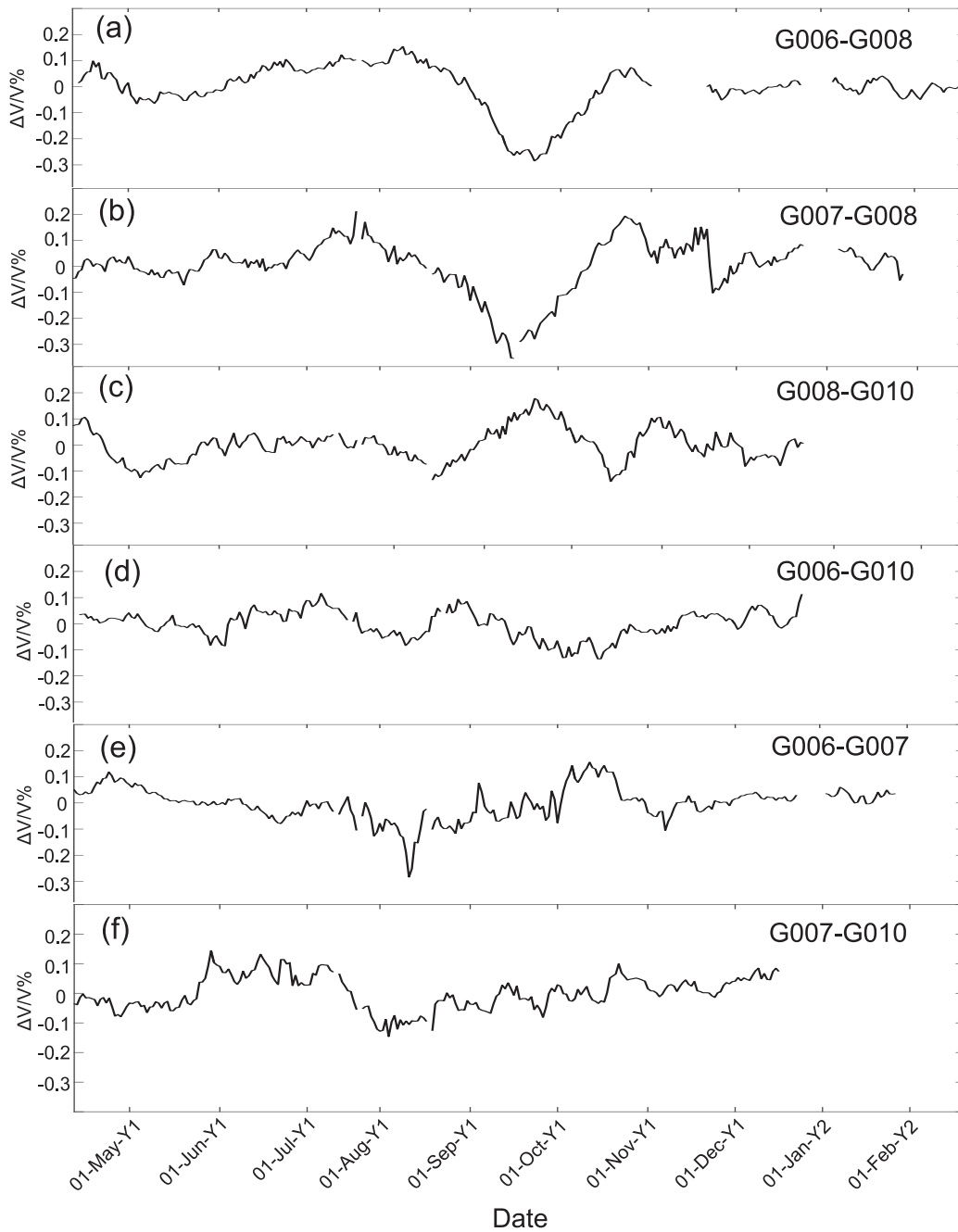


Figure 5.11: (a)–(f) The mean relative velocity variation from the causal part of the crosscorrelation functions measured using the doublet method at the frequency band of $[0.3, 0.8]$ Hz and for different station pairs including G006–G008, G007–G008, G008–G010, G006–G010, G006–G007, and G007–G010, respectively.

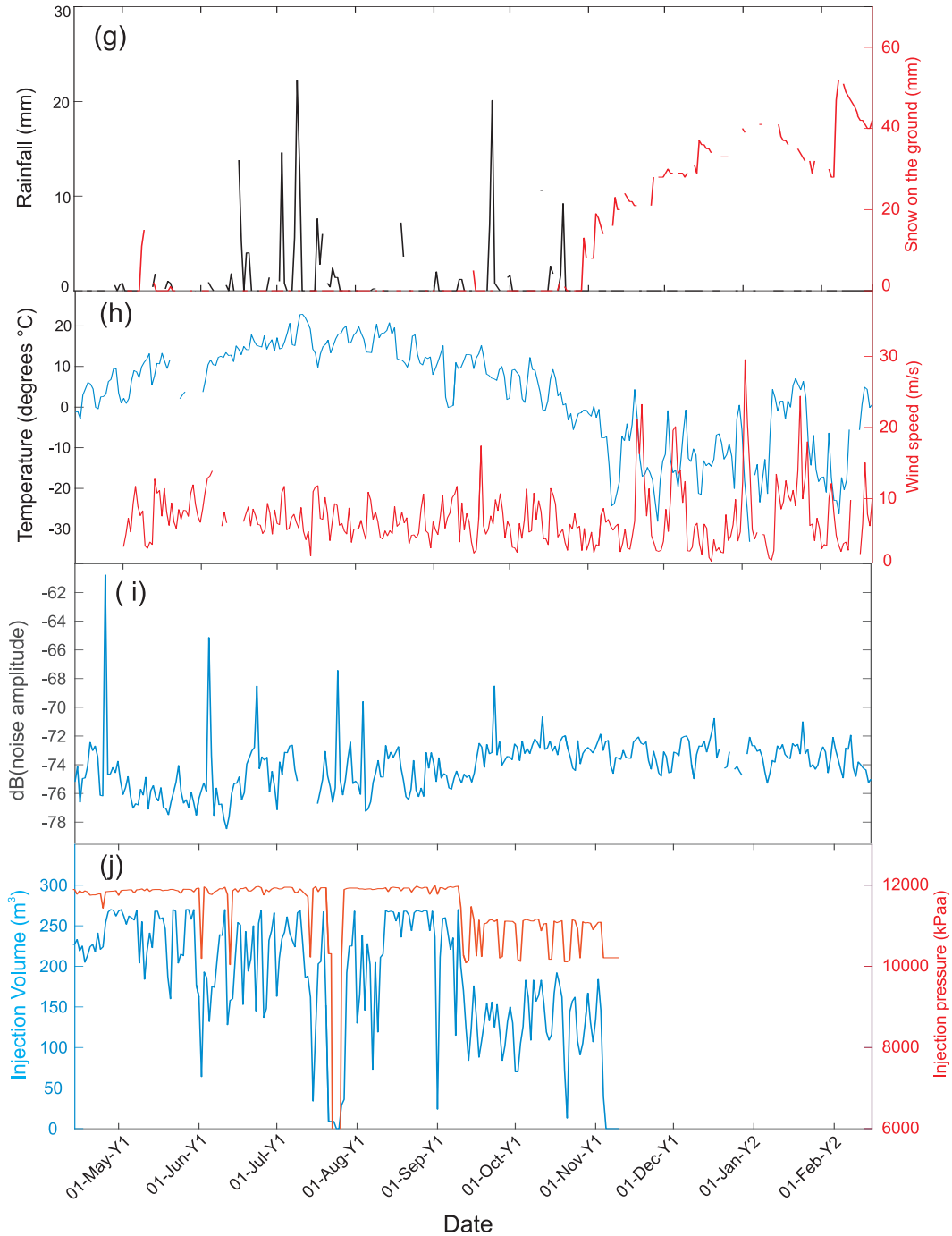


Figure 5.11 (cont.): (g) Daily rainfall (black) and snow depth (red) data from climate station B (Figure 5.1). (h) Daily temperature (black) and wind speed (red) data from climate station A (Figure 5.1). (i) Vertical-component daily RMS amplitude averaged between all stations in the frequency range of $[0.3, 0.8]$ Hz. (j) Fluid injection pressure (red) and injection volume (blue) curves.

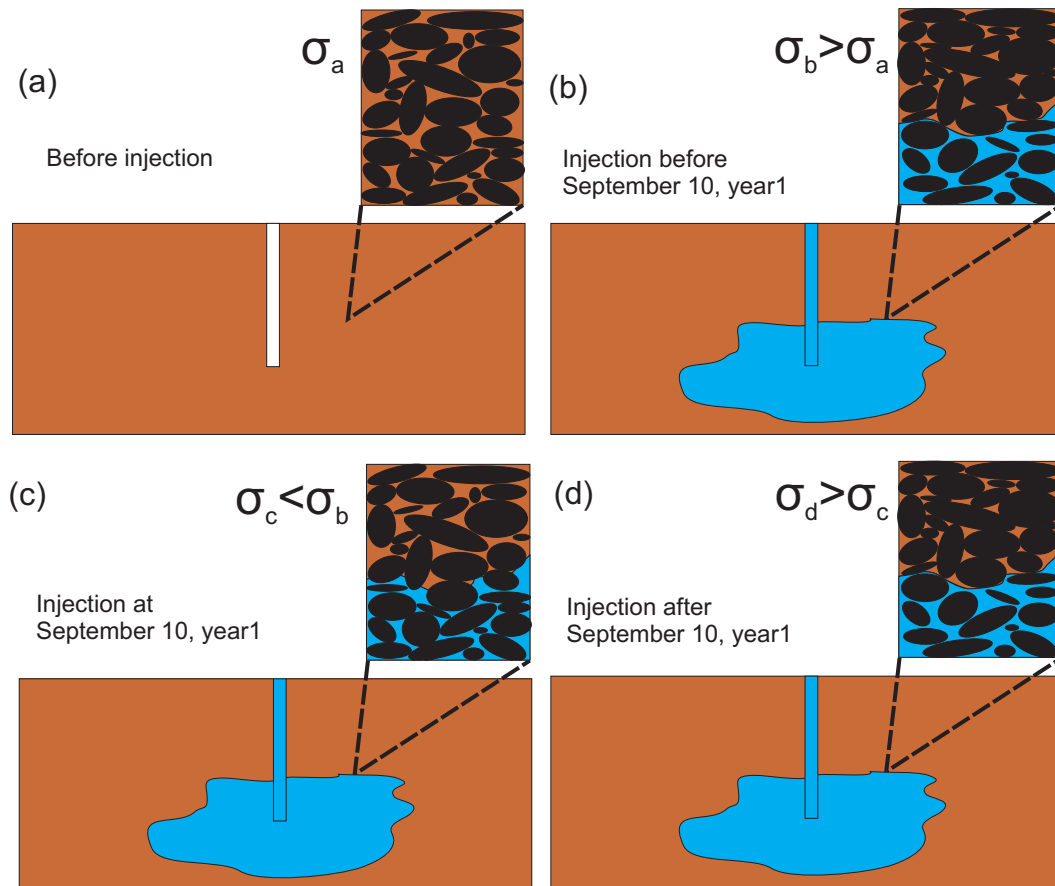


Figure 5.12: A schematic showing the stress variations beyond the injection point caused by different injection pressures during a time (b) when the injection pressures are increasing over time, (c) at and immediately after when injection pressures are reduced sharply, and (d) when the injection pressures are kept nearly constant or are increased again. (a) The ambient condition before the start of the fluid injection. The black ovals represent rock-constituting grains. The stress level beyond the injection point in each condition is represented by σ .

CHAPTER 6

Conclusions and suggested future research

6.1 Conclusions

Microseismic monitoring has gained significant importance as a tool to provide information on underground processes occurring during hydrocarbon production of unconventional reservoirs, wastewater disposal, geothermal energy production, CO₂ storage and sequestration, and mining operations. In addition to typical microseismic data analysis, several other existing and emerging new tools from different fields are being investigated and tested on microseismic data so that a more comprehensive understanding of the subsurface is acquired which can in turn lead to lower operational risks and even higher productions. Some of these techniques have proved very useful and have therefore become parts of the routine microseismic monitoring workflow. The main goal of this research was investigating the potential applications of seismic interferometry in microseismic monitoring. Seismic interferometry has already shown significant applications in exploration geophysics and global seismology.

The first application of seismic interferometry that we tested on a borehole microseismic dataset was to obtain information on seismic velocities at the geological formations surrounding the wellbore using the crosscorrelation functions calculated for different receiver pairs of the wellbore geophone array. We suggest that a possible reason for observing high-amplitude downgoing P-waves only in the low-frequency region is high levels of instrument self-noise with respect to the background noise. The shape of the instrument self-noise estimates obtained from the power spectral densities of the data and the very low number of weak microseismic events confirm that indeed the instrument noise floors might have been reached in this dataset. We conclude that selecting the proper instruments with appropriate sensitivities and self-noise levels is very important, particularly at deep quiet environments with very low background noise levels and at larger distances from the injection wells.

Although high levels of instrument self-noise in addition to large observational distances could explain the above-mentioned observations, the improper coupling of borehole geophones to the wellbore wall can also be considered as an alternative reason because a detached geophone hanging in the wellbore cannot record weak body waves traveling in the neighboring formations. Having tested the first application of seismic interferometry to several other borehole microseismic experiments we concluded that the characteristics of the reconstructed correlation functions can also be used to qualitatively assess the coupling of the wellbore geophones to the borehole wall. The fact that this technique requires only limited amount of data makes it a good indicator for geophone clamping monitoring in near real time. In addition to microseismic experiments it can also be used for testing coupling quality for vertical seismic profiles too.

Based on the idea that microseismic events typically show stronger spectral content over some frequency range than that of the background noise we introduced a new method for microseismic event detection using the power spectral density estimates. The following advantages make this technique superior over the common STA/LTA method for microseismic event detection: it detects a higher number of weak microseismic events with lower number of false alarms; it helps design more suitable bandpass filters; it performs better in detection of emergent events; and it provides useful information for event classification or identification.

We also investigated the potential application of passive image interferometry method to monitor relative velocity variations in a wastewater disposal well. There are differing behaviors observed for different station pairs and between estimates from the causal and acausal parts of the crosscorrelation functions. However, the fact that clear velocity changes are observed for some station pairs that are coincident with the time when the injection pressures were reduced significantly suggest that the latter may have caused some physical changes in the medium resulting in concomitant velocity variations. Poroelastic stress changes and pore pressure variations can be responsible for the observed velocity variations, depending on whether velocities increase or decrease.

6.2 Suggested future research

- Perform pore pressure diffusion modeling using parameters suitable for the wastewater disposal well in chapter 5 to verify that the pore pressure diffusion can indeed be the plausible cause of the observed relative velocity increases for some of the station pairs in this data set.
- Investigate the application of inter-source seismic interferometry for microseismic event

localization on real data for better constraints on the locations, as briefly mentioned in chapter 1.

- Use seismic interferometry to perform surface-wave tomographic inversion for some shallow microseismic experiments, such as for steam stimulation projects in heavy-oil production, as briefly mentioned in chapter 1.

Bibliography

- Ackerley, N., and Spriggs, N., 2012, Importance of Pre-Frack Site Surveys and Broadband Seismometers to Microseismic Monitoring, *Presented at CSEG Conference, GeoConvention 2012, Calgary, Canada*.
- Aki, K., 1957, Space and time spectra of stationary stochastic waves, with special reference to microtremors, *Bulletin of Earthquake Research Institute*, **35**, 415–456.
- Allen, R. V., 1978, Automatic earthquake recognition and timing from single traces, *Bulletin of the Seismological Society of America*, **68**, 1521-1532.
- Anderson, D. N., Randall, G. E., Whitaker, R. W., Arrowsmith, S. J., Arrowsmith, M. D., Fagan, D. K., Taylor, S. R., Selby, N. D., Schult, F. R., Kraft, G. D., and Walter, W. R., 2010, Seismic event identification, *WIREs Comp. Stat.*, **2**, 414–432, doi: 10.1002/wics.105.
- Andrews, L. C., 1997, *Special Functions of Mathematics for Engineers*, SPIE Press, doi: 10.1117/3.270709, eISBN: 9780819478467, p. 109-110.
- Bachmann, C. E., Wiemer, S., Woessner, J., and Hainzl, S., 2011, Statistical analysis of the induced Basel 2006 earthquake sequence: Introducing a probability-based monitoring approach for enhanced geothermal systems, *Geophysical Journal International*, **186**, 793–807, doi: 10.1111/j.1365-246X.2011.05068.x.
- Backus, G. E., 1962, Long-wave elastic anisotropy produced by horizontal layering, *Journal of Geophysical Research*, **67**, 4427-4440, doi: 10.1029/JZ067i011p04427.
- Baig, A. M., Campillo, M., and Brenguier, F., 2009, Denoising seismic noise correlations, *Journal of Geophysical Research*, **114**, B08310, doi: 10.1029/2008JB006085.
- Bakulin, A., and Calvert, R., 2004, Virtual source: New method for imaging and 4D below complex overburden, *SEG Technical Program Expanded Abstracts*, 2477–2480, doi: 10.1190/1.1845233.

- Bakulin, A., and Calvert, R., 2006, The virtual source method: Theory and case study, *Geophysics*, **71**(4), SI139SI150, doi: 10.1190/1.2216190.
- Bakulin, A., Mateeva, A., Mehta, K., Jorgensen, P., Ferrandis, J., Herhold, I.S., Lopez, J., 2007, Virtual source applications to imaging and reservoir monitoring, *The Leading Edge*, **26**(6), 732–740, doi: 10.1190/1.2748490.
- Bensen, G. D., Ritzwoller, M. H., Barmin, M. P., Levshin, A. L., Lin, F., Moschetti, M. P., Shapiro, N. M., and Yang, Y., 2007, Processing seismic ambient noise data to obtain reliable broad-band surface wave dispersion measurements, *Geophys. J. Int.*, **169**, 1239–1260, doi: 10.1111/j.1365-246X.2007.03374.x.
- Berger, J., Davis, P., and Ekström, G., 2004, Ambient Earth noise: A survey of the Global Seismographic Network, *J. Geophys. Res.*, **109**, 1-10, doi: 10.1029/2004jb003408.
- Bharadwaj, P., Schuster, G., Mallinson, I., and Dai, W., 2012, Theory of supervirtual refraction interferometry, *Geophys. J. Int.*, **188**, 263–273, doi: 10.1111/j.1365-246X.2011.05253.x.
- Bonnefoy-Claudet, S., Cotton, F. and Bard P.-Y., 2006, The nature of noise wavefield and its applications for site effects studies: A literature review, *Earth-Science Reviews*, **79**, 205–227, doi: 10.1016/j.earscirev.2006.07.004.
- Brenguier, F., Campillo, M., Hadziioannou, C., Shapiro, N. M., Nadeau, R. M., and Larose, E., 2008a, Postseismic relaxation along the San Andreas Fault at Parkfield from continuous seismological observation, *Science*, **321**, 1478–1481, doi: 10.1126/science.1160943.
- Brenguier, F., Shapiro, N. M., Campillo, M., Ferrazzini, V., Duputel, Z., Coutant, O., and Nercessian, A., 2008b, Towards forecasting volcanic eruptions using seismic noise, *Nature Geoscience*, **1**, 126–130, doi: 10.1038/ngeo104.
- Brenguier, F., Clarke, D., Aoki, Y., Shapiro, N. M., Campillo, M., and Ferrazzini, V., 2011, Monitoring volcanoes using seismic noise correlations, *Comptes Rendus Geoscience*, **343**, 633–638, doi: 10.1016/j.crte.2010.12 .010.
- Burridge, R., Lewicki, P., and Papanicolaou, G., 1994, Pulse stabilization in a strongly heterogeneous medium, *Wave Motion*, **20**, 177–195, doi: 10.1016/0165-2125(94)90041-8.
- Caffagni, E., Eaton, D., van der Baan, M., and Jones, J. P., 2015, Regional seismicity: A potential pitfall for identification of long-period long-duration events, *Geophysics*, **80**(1), A1–A5, doi: 10.1190/geo2014-0382.1.
- Campillo, M., and Paul, A., 2003, Long-Range Correlations in the Diffuse Seismic Coda, *Science*, **299**(5606), 547–549, doi: 10.1126/science.107855.

- Carter, G. C., 1978, Coherence and time delay estimation, *Proceedings of the IEEE*, **75**(2), 236–255, doi: 10.1109/PROC.1987.13723.
- Carter, J. A., Barstow, N., Pomeroy, P.W., Chael, E. P., and Leahy, P. J., 1991, High-frequency seismic noise as a function of depth, *Bulletin of the Seismological Society of America*, **81**, 1101–1114.
- Claerbout, J. F., 1968, Synthesis of a layered medium from its acoustic transmission response, *Geophysics*, **33**, 264–269, doi: 10.1190/1.1439927.
- Clarke, D., Zaccarelli, L., Shapiro, N. M., and Brenguier, F., 2011, Assessment of resolution and accuracy of the moving window cross spectral technique for monitoring crustal temporal variations using ambient seismic noise, *Geophysical Journal International*, **186**, 867–882, doi: 10.1111/j.1365-246X.2011.05074.x.
- Curtis, A., Gerstoft, P., Sato, H., Snieder, R., and Wapenaar, K., 2006, Seismic interferometry—turning noise into signal, *The Leading Edge*, **25**(9), 1082–1092, doi: 10.1190/1.2349814.
- Curtis, A., Nicolson, H., Halliday, D., Trampert, J., and Baptie, B., 2009, Virtual seismometers in the subsurface of the Earth from seismic interferometry, *Nature Geoscience*, **2**(10), 700–704, doi: 10.1038/ngeo615.
- Curtis, A., 2009, Source-receiver seismic interferometry, *SEG Technical Program Expanded Abstracts*, **28**(1), 3655–3659, doi: 10.1190/1.3255626.
- Curtis, A., and Halliday, D., 2010, Source-receiver wave field interferometry, *Physical Review E*, **81**(4), 046601, doi: 10.1103/PhysRevE.81.046601.
- Daley, T. M., Gritto, R., Majer, E. L., and West, P., 2003, Tube-wave suppression in single-well seismic acquisition, *Geophysics*, **68**, 863–869, doi: 10.1190/1.1581038.
- Das, I., and Zoback, M. D., 2011, Long period long duration seismic events during hydraulic fracture stimulation of a shale gas reservoir, *The Leading Edge*, **30**, 778–786, doi: 10.1190/1.3609093.
- Das, I., and Zoback, M. D., 2013, Long-period, long-duration seismic events during hydraulic stimulation of shale and tight-gas reservoirs – Part 1: Waveform characteristics, *Geophysics*, **78**(6), KS97–KS108, doi: 10.1190/geo2013-0164.1.
- De Meersman, K., van der Baan, M., and Kendall, J. M., 2006, Signal extraction and automated polarisation analysis of multi-component array data, *Bulletin of the Seismological Society of America*, **96**, 2415–2430.

- De Meersman, K., Kendall, J. M., and van der Baan, M., 2009, The 1998 Valhall microseismicity: An integrated study of relocated sources, seismic multiplets and S-wave splitting, *Geophysics*, **74**(5), B183–B195.
- Derode, A., Larose, E., Campillo, M., and Fink, M., 2003a, How to estimate the Green's function of a heterogeneous medium between two passive sensors? Application to acoustic waves, *Applied Physics Letters*, **83**(15), 3054–3056, doi: 10.1063/1.1617373.
- Derode, A., Larose, E., Tanter, M., de Rosny, J., Tourin, A., Campillo, M., and Fink, M., 2003b, Recovering the Green's function from field-field correlations in an open scattering medium (L), *The Journal of the Acoustical Society of America*, **113**(6), 2973–2976, doi: 10.1121/1.1570436.
- Dong, S., Sheng, J., and Schuster, G. T., 2006a, Theory and practice of refraction interferometry, *76th Annual International Meeting, SEG, Expanded Abstracts*, 3021–3025, doi: 10.1190/1.2370154.
- Dong, S., He, R., and Schuster, G. T., 2006b, Interferometric prediction and least squares subtraction of surface waves, *76th Annual International Meeting, SEG, Expanded Abstracts*, 2783–2786, doi: 10.1190/1.2370102.
- Draganov, D., Wapenaar, K., Mulder, W., Singer, J., and Verdel, A., 2007, Retrieval of reflections from seismic background noise measurements, *Geophysical Research Letters*, **34**, L04305, doi: 10.1029/2006GL028735.
- Duputel, Z., Ferrazzini, V., Brenguier, F., Shapiro, N., Campillo, M., and Nercessian, A., 2009, Real time monitoring of relative velocity changes using ambient seismic noise at the Piton de la Fournaise volcano (La Reunion) from January 2006 to June 2007, *Journal of Volcanology and Geothermal Research*, **184** (1-2, Sp. Iss. SI), 164–173, doi: 10.1016/j.jvolgeores.2008.11.024.
- Duvall, T. L., Jefferies, S. M., Harvey, J. W., and Pomerantz, M. A., 1993, Time-distance helioseismology, *Nature*, **362**(6419), 430–432, doi:10.1038/362430a0.
- Earle, P., and Shearer, P., 1994, Characterization of global seismograms using an automatic picking algorithm, *Bull. seism. Soc. Am.*, **84**(2), 366–376.
- Eaton, D. W., van der Baan, M., Tary, J-B., Birkelo, B., Spriggs, N., Cutten, S., Pike, K., 2013, Broadband microseismic observations from a Montney hydraulic fracture treatment, northeastern B.C., Canada, *CSEG Recorder*, 44–53.
- Eaton, D., Caffagni, E., Rafiq, A., van der Baan, M., Roche, V., and Matthews, L., 2014, Passive seismic monitoring and integrated geomechanical analysis of a tight-sand reser-

- voir during hydraulic-fracture treatment, flowback and production, Unconventional Resources Technology Conference, *Society of Petroleum Engineers*, doi: 10.15530/utrec-2014-1929223.
- Edwards, D. E., Barclay, J. E., Gibson, D. W., Kvill, G. E., and Halton, E., 2012, Triassic Strata of the Western Canada Sedimentary Basin, in *Geological Atlas of the Western Canada Sedimentary Basin*, pp. 259–276, *Alberta Geological Survey*.
- Eisner, L., Maxwell, S., Raymer, D., Williams, M., and Primiero, P., 2013, Signals, *The Leading Edge*, **32**, 868–868, doi: 10.1190/tle32080868.1.
- Ellsworth, W. L., 2013, Injection-induced earthquakes, *Science*, **341**(6142), doi: 10.1126/science.1225942.
- Ewing, W. M., Jardetzky, W. S., and Press, F., 1957, Elastic waves in layered media, *McGraw-Hill Book Company Inc.*, New York.
- Fagan, D., Van wijk, K., and Rutledge, J., 2013, Clustering revisited: A spectral analysis of microseismic events, *Geophysics*, **78**(2), 568–571, doi: 10.1190/GEO2012-0323.1.
- Frchet, J., Martel, L., Nikolla, L., and Poupinet, G., 1989, Application of the cross-spectral moving-window technique (CSMWT) to the seismic monitoring of forced fluid migration in a rock mass, *International Journal of Rock Mechanics and Mining Sciences*, **26**(3-4), 221–233, doi: 10.1016/0148-9062(89)91972-4.
- Froment, B., Campillo, M., Roux, P., Gouédard, P., Verdel, A., and Weaver, R. L., 2010, Estimation of the effect of nonisotropically distributed energy on the apparent arrival time in correlations, *Geophysics*, **75**, SA85–SA93, doi:10.1190/1.3483102.
- Froment, B., Campillo, M., Chen, J. H., and Liu, Q. Y., 2013, Deformation at depth associated with the 12 May 2008 Mw 7.9 Wenchuan earthquake from seismic ambient noise monitoring, *Geophysical Research Letters*, **40**, 78–82, doi: 10.1029/2012GL053995.
- Galetti, E., and Curtis, A., 2012, Generalised receiver functions and seismic interferometry, *Tectonophysics*, **532535**(0), 1–26, doi: 10.1016/j.tecto.2011.12.004.
- Galperin, E. I., 1985, Vertical seismic profiling and its exploration potential, *Springer Science & Business Media*.
- Garnier, J., and Papanicolaou, J., 2009, Passive sensor imaging using cross correlations of noisy signals in a scattering medium, *SIAM J. Imaging Sciences*, **2**(2), 396–437, doi: 10.1137/080723454.

- Gassenmeier, M., Sens-Schönfelder, C., Delatre, M., and Korn, M., 2015, Monitoring of environmental influences on seismic velocity at the geological storage site for CO₂ in Ketzin (Germany) with ambient seismic noise, *Geophysical Journal International*, **200**(1), 524–533, doi: 10.1093/gji/ggu413.
- Gerstoft, P., Sabra, K. G., Roux, P., Kuperman W. A., and Fehler, M. C., 2006, Green's functions extraction and surface wave tomography from microseisms in Southern California, *Geophysics*, **71**(4), SI23–SI31, doi: 10.1190/1.2210607.
- Gerstoft, P., Shearer, P. M., Harmon, N., and Zhang, J., 2008, Global P, PP, and PKP wave microseisms observed from distant storms, *Geophysical Research Letters*, **35**, L23307, doi: 10.1029/2008GL036111.
- Giardini, D., 2009, Geothermal quake risks must be faced, *Nature*, **462**, 848–849, doi: 10.1038/462848a.
- Goertz, A., Cieslik, K., Hauser, E., Watts, G., McCrossin, S., and Zbasnik, P., 2011, A combined borehole/surface broadband passive seismic survey over a gas storage field, *81st Annual International Meeting, SEG, Expanded Abstracts*, **30**, 1488–1492, doi: 10.1190/1.3627484.
- Goertz, A., Riahi, N., Kraft, T., and Lambert, M., 2012, Modeling detection thresholds of microseismic monitoring networks, *82nd Annual International Meeting, SEG, Expanded Abstracts*, **31**, 1–6, doi: 10.1190/segam2012-1069.1.
- Gouédard, P., Roux, P., Campillo, M., and Verdel, A., 2008, Convergence of the two-point correlation function toward the Green's function in the context of a seismic-prospecting data set, *Geophysics*, **73**(6), V47–V53, doi: 10.1190/1.2985822.
- Gouédard, P., Seher, T., McGuire, J. J., Collins, J. A., and van der Hilst, R. D., 2014, Correction of ocean-bottom seismometer instrumental clock errors using ambient seismic noise, *Bulletin of the Seismological Society of America*, **104**(3), 1276–1288, doi: 10.1785/0120130157.
- Grechka, V., and Zhao, Y., 2012, Microseismic interferometry, *The Leading Edge*, **31**, 1478–1483, doi: 10.1190/tle31121478.1.
- Grêt, A., Snieder, R., Aster, R. C., and Kyle, R., 2005, Monitoring rapid temporal change in a volcano with coda wave interferometry, *Geophysical Research Letters*, **32**, L06304, doi: 10.1029/2004GL021143.
- Grêt, A., Snieder, R., and Özbay, U., 2006a, Monitoring in situ stress changes in a mining environment with coda wave interferometry, *Geophysical Journal International*, **167**(2), 504–508, doi: 10.1111/j.1365-246X.2006.03097.x.

- Grêt, A., Snieder, R., Scales, J., 2006b, Time-lapse monitoring of rock properties with coda wave interferometry, *Journal of Geophysical Research*, **111**(B3), B03305, doi: 10.1029/2004JB003354.
- Groos, J. C., Bussat, S., and Ritter, J. R. R., 2012, Performance of different processing schemes in seismic noise cross-correlations, *Geophysical Journal International*, **188**, 498–512, doi: 10.1111/j.1365-246X.2011.05288.x.
- Hadziioannou, C., Larose, E., Coutant, O., Roux, P., and Campillo, M., 2009, Stability of monitoring weak changes in multiply scattering media with ambient noise correlation: Laboratory experiments, *Journal of the Acoustical Society of America*, **125**, 3688–3695, doi: 10.1121/1.3125345.
- Hadziioannou, C., Larose, E., Baig, A., Roux, P., and Campillo, M., 2011, Improving temporal resolution in ambient noise monitoring of seismic wave speed, *Journal of Geophysical Research*, **116**, B07304, doi:10.1029/2011JB008200.
- Halliday, D. F., Curtis, A., Robertsson, J. O., and van Manen, D.-J., 2007, Interferometric surface-wave isolation and removal, *Geophysics*, **72**(5), A69–A73, doi: 10.1190/1.2761967.
- Halliday, D., 2009, Surface wave interferometry, PhD thesis, University of Edinburgh.
- Halliday, D. F., Curtis, A., Vermeer, P., Strobbia, C., Glushchenko, A., van Manen, D.-J., and Robertsson, J. O., 2010, Interferometric ground-roll removal: Attenuation of scattered surface waves in single-sensor data, *Geophysics*, **75**(2), SA15–SA25, doi: 10.1190/1.3360948.
- Hardage, B. A., 1981, An examination of tube wave noise in vertical seismic profiling data, *Geophysics*, **46**, 892–903, doi: 10.1190/1.1441228.
- Harris, F., 1978, On the use of windows for harmonic analysis with the discrete Fourier transform, *Proc. IEEE*, **66**, 51–83, doi: 10.1109/PROC.1978.10837.
- He, R., Hornby, B., and Schuster, G., 2007, 3D wave-equation interferometric migration of VSP free-surface multiples, *Geophysics*, **72**(5), S195–S203, doi: 10.1190/1.2743375.
- Herrera, R. H., Fomel, S., and van der Baan, M., 2014, Automatic approaches for seismic to well tying, *Interpretation*, **2**(2), SD9–SD17, doi: 10.1190/INT-2013-0130.1.
- Herrera, R. H., and van der Baan, M., 2014, A semiautomatic method to tie well logs to seismic data, *Geophysics*, **79**(3), V47–V54, doi: 10.1190/geo2013-0248.1.
- Hillers, G., Campillo, M., and Ma, K.-F., 2014, Seismic velocity variations at TCDP are controlled by MJO driven precipitation pattern and high fluid discharge properties, *Earth and Planetary Science Letters*, **391**, 121–127, doi: 10.1016/j.epsl.2014.01.040.

- Hillers, G., Ben-Zion, Y., Campillo, M., and Zigone, D., 2015a, Seasonal variations of seismic velocities in the San Jacinto fault area observed with ambient seismic noise, *Geophysical Journal International*, **202**(2), 920–932, doi: 10.1093/gji/ggv151.
- Hillers, G., Retailleau, L., Campillo, M., Inbal, A., Ampuero, J.-P., and Nishimura, T., 2015b, In situ observations of velocity changes in response to tidal deformation from analysis of the high-frequency ambient wavefield, *Journal of Geophysical Research*, **120**, 210–225, doi: 10.1002/2014JB011318.
- Hobiger, M., Wegler, U., Shiomi, K., and Nakahara, H., 2012, Coseismic and postseismic elastic wave variations caused by the 2008 Iwate-Miyagi Nairiku earthquake, Japan, *Journal of Geophysical Research*, **117**, B09313, doi: 10.1029/2012JB009402.
- Hobiger, M., Wegler, U., Shiomi, K., and Nakahara, H., 2014, Single-station cross-correlation analysis of ambient seismic noise: application to stations in the surroundings of the 2008 Iwate-Miyagi Nairiku earthquake, *Geophysical Journal International*, **198**(1), 90–109, doi: 10.1093/gji/ggu115.
- Hong, T. -K., and Menke, W., 2006, Tomographic investigation of the wear along the San Jacinto fault, southern California, *Physics of The Earth and Planetary Interiors*, **155**(34), 236–248, doi: 10.1016/J.pepi.2005.12.005.
- Hornby, B. E., and Yu, J., 2007, Interferometric imaging of a salt flank using walkaway VSP data, *The Leading Edge*, **26**, 760–763, doi: 10.1190/1.2748493.
- Hotovec-Ellis, A. J., Gomberg, J., Vidale, J. E., and Creager, K. C., 2014, A continuous record of intereruption velocity change at Mount St. Helens from coda wave interferometry, *Journal of Geophysical Research Solid Earth*, **119**, 2199–2214, doi: 10.1002/2013JB010742.
- Hutt, C. R., Nigbor, R. L., and Evans, J., 2009, Proceedings of the guidelines for seismometer testing workshop, Albuquerque, New Mexico, 910 May 2005 ("GST"), *USGS Open-File Report*, 2009–1055, 48p.
- Jiang, Z., Sheng, J., Yu, J., Schuster, G. T., and Hornby, B. E., 2007, Migration methods for imaging different-order multiples, *Geophysical Prospecting*, **55**, 1–19, doi: 10.1111/j.1365-2478.2006.00598.x.
- Julian, B. R., and Foulger, G. R., 2010, Time-dependent seismic tomography, *Geophysical Journal International*, **182**, 1327–1338, doi: 10.1111/j.1365-246X.2010.04668.x.
- Keranen, K. M., Weingarten, M., Abers, G. A., Bekins, B. A., Ge, S., 2014, Sharp increase in central Oklahoma seismicity since 2008 induced by massive wastewater injection, *Science*, **345**, 448–451, doi: 10.1126/science.1255802.

- King, S., Curtis, A., and Poole, T.L., 2011, Interferometric velocity analysis using physical and nonphysical energy, *Geophysics*, **76**(1), SA35–SA49, doi: 10.1190/1.3521291.
- Knapp, C., and Carter, G. C., 1976, The generalized correlation method for estimation of time delay, *Acoustics, Speech and Signal Processing, IEEE Transactions*, **24**(4), 320–327, doi: 10.1109/TASSP.1976.1162830.
- Lamb, H., 1898, On the velocity of sound in a tube, as affected by the elasticity of the walls, *Manchester Memoirs*, **42**, 1–16.
- Langer, H., Falsaperla, S., Powell, T., and Thompson, G., 2006, Automatic classification and a-posteriori analysis of seismic event identification at Soufrière Hills volcano, Montserrat, *J. Volcanol. Geotherm. Res.*, **153**, 1–10, doi: 10.1016/j.jvolgeores.2005.08.012.
- Larose, E., Derode, A., Campillo, M., and Fink, M., 2004, Imaging from one-bit correlations of wideband diffuse wave fields, *Journal of Applied Physics*, **95**, 8393–8399, doi: 10.1063/1.1739529.
- Larose, E., Derode, A., Clorennec, D., Margerin, L., and Campillo, M., 2005, Passive retrieval of Rayleigh waves in disordered elastic media, *Physical Review E*, **72**(4), 046607, doi: 10.1103/PhysRevE.72.046607.
- Larose, E., Margerin, L., Derode, A., van Tiggelen, B., Campillo, M., Shapiro, N., Paul, A., Stehly, L., and Tanter, M., 2006, Correlation of random wavefields: An interdisciplinary review, *Geophysics*, **71**(4), SI11–SI21, doi: 10.1190/1.2213356
- Larose, E., Roux, P., Campillo, M., and Derode, A., 2008, Fluctuations of correlations and Green’s function reconstruction: role of scattering, *Journal of Applied Physics*, **103**(11), 114907–114907-10, doi: 10.1063/1.2939267.
- Larose, E., Planès, T., Rossetto, V., and Margerin, L., 2010, Locating a small change in a multiple scattering environment, *Applied Physics Letters*, **96**, 204101, doi: 10.1063/1.3431269.
- Lee, A. W., 1935, On the direction and approach of microseismic waves, *Proc. R. Soc. London, Ser. A, Mathematical and Physical Sciences*, **149**, 183–199, doi: 10.1098/rspa.1935.0056.
- Lobkis, O. I., and Weaver, R. L., 2001, On the emergence of the Green’s function in the correlations of a diffuse field, *The Journal of the Acoustical Society of America*, **110**(6), 3011–3017, doi: 10.1121/1.1417528.
- Lobkis, O. I., and Weaver, R. L., 2003, Coda-wave interferometry in finite solids: Recovery of P-to-S conversion rates in an elastodynamic billiard, *Physical Review Letters*, **90**, 25–27, doi: 10.1103/PhysRevLett.90.254302.

- Lowrie, W., 2007, *Fundamentals of Geophysics Second Ed.*, Cambridge University Press, New York, 375 pp.
- Lu, R., Willis, M., Campman, X., Ajo-Franklin, J., and Toksöz, M. N., 2008, Redatuming through a salt canopy and target-oriented salt-flank imaging, *Geophysics*, **73**(3), S63–S71, doi: 10.1190/1.2890704.
- Mainsant, G., Larose, E., Brönnimann, C., Jongmans, D., Michoud, C., and Jaboyedoff, M., 2012, Ambient seismic noise monitoring of a clay landslide: toward failure prediction, *Journal of Geophysical Research*, **117**(F1), F01030, doi:10.1029/2011JF002159.
- Mallinson, I., Bharadwaj, P., Schuster, G., and Jakubowicz, H., 2011, Enhanced refractor imaging by supervirtual interferometry, *The Leading Edge*, **30**, 546–550, doi: 10.1190/1.3589113.
- Maxwell, S. C., White, D. J., and Fabriol, H., 2004, Passive seismic imaging of CO₂ sequestration at Weyburn, *74th Annual International Meeting, SEG, Expanded Abstracts*, **23**, 568–571, doi: 10.1190/1.1842409.
- Maxwell, S. C., Underhill, B., Bennett, L., Woerpel, C., and Martinez, A., 2010a, Key criteria for a successful microseismic project, *SPE annual technical conference and exhibition*, **4**, 3193–3208, doi: 10.2118/134695-MS.
- Maxwell, S. C., Rutledge, J., Jones, R., and Fehler, M., 2010b, Petroleum reservoir characterization using downhole microseismic monitoring, *Geophysics*, **75**, 75A129–75A137, doi: 10.1190/1.3477966.
- Maxwell, S. C., 2011, Microseismic hydraulic fracture imaging; the path toward optimizing shale gas production, *Leading Edge*, **30**, 340–346, doi: 10.1190/1.3567266.
- Maxwell, S. C., Raymer, D., Williams, M., and Primiero, P., 2012, Tracking microseismic signals from the reservoir to surface, *The Leading Edge*, **31**, 1300–1308, doi: 10.1190/tle31111300.1.
- McMechan G. A., and Yedlin, M. J., 1981, Analysis of dispersive waves by wave field transformation, *Geophysics*, **46**, 869–874, doi: 10.1190/1.1441225.
- Mehta, K., Sheiman, J. L., Snieder, R., and Calvert, R., 2008, Strengthening the virtual-source method for time-lapse monitoring, *Geophysics*, **73**(3), S73–S80, doi: 10.1190/1.2894468.
- Meier, U., Shapiro, N. M., and Brenguier, F., 2010, Detecting seasonal variations in seismic velocities within Los Angeles basin from correlations of ambient seismic noise, *Geophysical Journal International*, **181**, 985–996, doi: 10.1111/j.1365-246X.2010.04550.x.

- Mikesell, D., van Wijk, K., Calvert, A., and Haney, M., 2009, The virtual refraction: Useful spurious energy in seismic interferometry, *Geophysics*, **74**(3), A13–A17, doi: 10.1190/1.3095659.
- Minato, S., Onishi, K., Matsuoka, T., Okajima, Y., Tsuchiyama, J., Nobuoka, D., Azuma, H., and Iwamoto, T., 2007, Cross-well seismic survey without borehole source, *77th Annual International Meeting, SEG, Expanded Abstracts*, 1357–1361, doi: 10.1190/1.2792752.
- McEvelly, T. V., and Majer, E. L., 1982, ASP: An automated seismic processor for micro-earthquake networks, *Bull. seism. Soc. Am.*, **72**, 303–325.
- McGillivray, P., 2005, Microseismic and time-lapse seismic monitoring of a heavy oil extraction process at Peace River, Canada, *CSEG Recorder*, **30**(1), 5–9.
- McNamara, D. E., and Buland, R. P., 2004, Ambient noise levels in the continental United States, *Bulletin of the Seismological Society of America*, **94**, 1517–1527, doi: 10.1785/012003001.
- Miyazawa, M., Snieder, R., and Venkataraman, A., 2008, Application of seismic interferometry to extract P- and S-wave propagation and observation of shear-wave splitting from noise data at Cold Lake, Alberta, Canada, *Geophysics*, **73**(4), 35–40, doi:10.1190/1.2937172.
- Nagaoka, Y., Nishida, K., Aoki, Y., and Takeo, M., 2010, Temporal change of phase velocity beneath Mt. Asama, Japan, inferred from coda wave interferometry, *Geophysical Research Letters*, **37**(22), L22311L, doi: 10.1029/2010GL045289.
- National Research Council, 2013, Induced Seismicity Potential in Energy Technologies, Washington, DC, *The National Academies Press*, doi:10.17226/13355.
- Nishimura, T., Uchida, N., Sato, H., Ohtake, M., Tanaka, S., and Hamaguchi, H., 2000, Temporal changes of the crustal structure associated with the M6.1 earthquake on September 3, 1998 and the volcanic activity of mount Iwate, Japan, *Geophysical Research Letters*, **27**(2), 269–272, doi: 10.1029/1999GL005439.
- Nofal, H. A.-E. M., Ahmed, E. M., Al Geldawy, F. A.-E., and Hafiz, A. G. R., 2004, Near optimum detection of the p-wave arrival using the spectrograms, *Proceedings, International Conference on Electrical, Electronic and Computer Engineering, ICEEC'04*, 710–715, doi: 10.1109/ICEEC.2004.1374577.
- Obermann, A., Planès, T., Larose, E., and Campillo, M., 2013a, Imaging preeruptive and coeruptive structural and mechanical changes of a volcano with ambient seismic noise, *Journal of Geophysical Research*, **118**, 6285–6294, doi: 10.1002/2013JB010399.

- Obermann, A., Planès, T., Larose, E., Sens-Schönfelder, C., and Campillo, M., 2013b, Depth sensitivity of seismic coda waves to velocity perturbations in an elastic heterogeneous medium, *Geophysical Journal International*, **194**, 372–382, doi: 10.1093/gji/ggt043.
- Obermann, A., Froment, B., Campillo, M., Larose, E., Planès, T., Valette, B., Chen, J. H., and Liu, Q. Y., 2014, Seismic noise correlations to image structural and mechanical changes associated with the Mw 7.9 2008 Wenchuan earthquake, *Journal of Geophysical Research*, **119**, 3155–3168, doi: 10.1002/2013JB010932.
- Özbek, A., Probert, T., Raymer, D., and Drew, J., 2013, Nonlinear Processing Methods for Detection and Location of Microseismic Events, *75th EAGE Conference and Exhibition, London, UK*, doi: 10.3997/2214-4609.20130397.
- Pacheco, C., and Snieder, R., 2005, Time-lapse travel time change of multiply scattered acoustic waves, *Journal of the Acoustical Society of America*, **118**, 1300–1310, doi: 10.1121/1.2000827.
- Peterson, J., 1993, Observations and modeling of seismic background noise, *USGS Open-File Report*, pp. 093-322.
- Pandolfi, D., Bean, C.J., and Saccorotti, G., 2006, Coda wave interferometric detection of seismic velocity changes associated with the 1999 M = 3.6 event at Mt. Vesuvius, *Geophys. Res. Lett.*, **33**(6), L06306, doi: 10.1029/2005GL025355.
- Park, J., Lindberg, C. R., and Vernon III, F. L., 1987, Multitaper spectral analysis of high-frequency seismograms, *J. Geophys. Res.*, **92**, 12675–12684, doi: 10.1029/JB092iB12p12675.
- Paul, A., Campillo, M., Margerin, L., Larose, E., and Derode, A., 2005, Empirical synthesis of time-asymmetrical Green functions from the correlation of coda waves, *J. Geophys. Res.*, **110**, B08302, doi:10.1029/2004JB003521.
- Phillips, W.S., Rutledge, J. T., and House, L., 2002, Induced microearthquake patterns in hydrocarbon and geothermal reservoirs: six case studies, *Pure Appl. Geophys.*, **159**, 345–369, doi: 10.1007/PL00001256.
- Planès, T., 2013, Imagerie de changements locaux en régime de diffusion multiple, PhD thesis, Université de Grenoble, Grenoble, France.
- Poliannikov, O. V., Malcolm, A. E., Djikpesse, H., and Prange, M., 2011, Interferometric hydrofracture microseism localization using neighboring fracture, *Geophysics*, **76**(6), WC27–WC36, doi: 10.1190/geo2010-0325.1.

- Poupinet, G., Ellsworth, W. L., and Frechet, J., 1984, Monitoring velocity variations in the crust using earthquake doublet: An application to the Calveras Fault, California, *Journal of Geophysical Research*, **89**, 5719–5731, doi: 10.1029/JB089iB07p05719.
- Prieto, G. A., Lawrence, J. F., and Beroza, G. C., 2009, Anelastic earth structure from the coherency of the ambient seismic field, *J. Geophys. Res.*, 114, B07303, doi: 10.1029/2008JB006067.
- Richter, T., Sens-Schönfelder, C., Kind, R., and Asch, G., 2014, Comprehensive observation and modeling of earthquake and temperature-related seismic velocity changes in northern Chile with passive image interferometry, *Journal of Geophysical Research*, **119**, 4747–4765, doi: 10.1002/2013JB010695.
- Rickett, J., and Claerbout, J., 1999, Acoustic daylight imaging via spectral factorization; helioseismology and reservoir monitoring, *The Leading Edge*, **18**(8), 957–960, doi: 10.1190/1.1820854.
- Riedesel, M. A., Moore, R. D., and Orcutt, J. A., 1990, Limits of sensitivity of inertial seismometers with velocity transducers and electronic amplifiers, *Bulletin of the Seismological Society of America*, **80**, 1725–1752.
- Ringler, A., and Hutt, C., 2010, Self-Noise Models of Seismic Instruments, *Seismological Research Letters*, **81**, 972–983, doi: 10.1785/gssrl.81.6.972.
- Rivet, D., Campillo, M., Shapiro, N. M., Cruz-Atienza, V., Radiguet, M., Cotte, N., and Kostoglodov, V., 2011, Seismic evidence of nonlinear crustal deformation during a large slow slip event in Mexico, *Geophysical Research Letters*, **38**, L08308, doi: 10.1029/2011GL047151.
- Rivet, D., Brenguier, F., Clarke, D., Shapiro, N. M., and Peltier, A., 2014, Long-term dynamics of Piton de la Fournaise volcano from 13 years of seismic velocity change measurements and GPS observations, *Journal of Geophysical Research Solid Earth*, **119**, 7654–7666, doi:10.1002/2014JB011307.
- Roux, P., Kuperman, W. A., and NPAL Group, 2004, Extracting coherent wavefronts from acoustic ambient noise in the ocean, *The Journal of Acoustical Society of America*, **116**, 1995–2003, doi: 10.1121/1.1797754.
- Roux, P., Sabra, K. G., Gerstoft, P., Kuperman, W. A., and Fehler, M. C., 2005, P-waves from cross correlation of seismic noise, *Geophysical Research Letters*, **32**, L19303, doi: 10.1029/2005GL023803.

- Roux, P., 2009, Passive seismic imaging with directive ambient noise: Application to surface waves and the San Andreas fault in Parkfield, California, *Geophysical Journal International*, **179**(1), 367–373, doi: 10.1111/j.1365-246X.2009.04282.x.
- Roux, P., Wathelet, M., and Roueff, A., 2011, The San Andreas Fault revisited through seismic-noise and surface-wave tomography, *Geophysical Research Letters*, **38**, L13319, doi: 10.1029/2011GL047540.
- Ruigrok, E., Campman, X., and Wapenaar, K., 2011, Extraction of P-wave reflections from microseisms, *Comptes Rendus Geoscience*, **343**, 512–525, doi: 10.1016/j.crte.2011.02.006.
- Rutqvist, J., 2012, The geomechanics of CO₂ storage in deep sedimentary formations, *Geotechnical and Geological Engineering*, **30**, 525–551, doi: 10.1007/s10706-011-9491-0.
- Sabra, K. G., Gerstoft, P., Roux, P., Kuperman, W. A., and Fehler, M. C., 2005a, Extracting time-domain Green’s function estimates from ambient seismic noise, *Geophysical Research Letters*, **32**, L03310-1–L03310-5, doi: 10.1029/2004GL021862.
- Sabra, K. G., Gerstoft, P., Roux, P., Kuperman, W. A., and Fehler, M. C., 2005b, Surface wave tomography from microseisms in southern California, *Geophysical Research Letters*, **32**, L14311-1–L14311-4, doi: 10.1029/2005GL023155.
- Sabra, K., Roux, P., and Kuperman, W., 2005c, Emergence rate of the time domain Green’s function from the ambient noise cross-correlation, *The Journal of the Acoustical Society of America*, **118**(6), 3524–3531, doi: 10.1121/1.2109059.
- Sabra, K. G., Roux, P., Gerstoft, P., Kuperman, W. A., and Fehler, M. C., 2006, Extracting coda arrivals from cross-correlations of long period scattered waves during the Mount St. Helens 2004 eruption, *Geophysical Research Letters*, **33**, L06313, doi: 10.1029/2005GL025563.
- Sánchez-Sesma, F., and Campillo, M., 2006, Retrieval of the Green’s function from cross correlation: The canonical elastic problem, *Bull. Seismol. Soc. Am.*, **96**(3), 1182–1191, doi:10.1785/0120050181.
- Scarpetta, S., Giudicepietro, F., Ezin, E. C., Petrosino, S., Del Pezzo, E., Martini, M., and Marinaro, M., 2005, Automatic classification of seismic signals at Mt. Vesuvius volcano, Italy, using neural networks, *Bull. seism. Soc. Am.*, **95**(1), 185–196, doi: 10.1785/0120030075.
- Schoenball, M., Dorbath, L., Gaucher, E., Wellmann, J. F., and Kohl, T., 2014, Change of stress regime during geothermal reservoir stimulation, *Geophysical Research Letters*, **41**, 1163–1170, doi: 10.1002/2013GL058514.

- Schuster, G. T., 2001, Theory of daylight/interferometric imaging: Tutorial, *63rd Annual International Conference and Exhibition, EAGE, Extended Abstracts*, A32.
- Schuster, G. T., Yu, J., Sheng, J., Rickett, J., 2004, Interferometric/daylight seismic imaging, *Geophysical Journal International*, **157**(2), 838–852, doi: 10.1111/j.1365-246X.2004.02251.x.
- Schuster, G. T., 2009, Seismic interferometry, *Cambridge University Press*.
- Schuster, G., and Zhou, M., 2006, A theoretical overview of model-based and correlation-based redatuming methods, *Geophysics*, **71**(4), SI103–SI110, doi: 10.1190/1.2208967.
- Seats, K. J., Lawrence, J. F., and Prieto, G. A., 2012, Improved ambient noise correlation functions using Welch’s method, *Geophysical Journal International*, **188**, 513–523, doi: 10.1111/j.1365-246X.2011.05263.x.
- Sens-Schönfelder, C., and Wegler, U. C., 2006, Passive image interferometry and seasonal variations of seismic velocity at Merapi Volcano, Indonesia, *Geophysical Research Letters*, **33**, L21302, doi: 10.1029/2006GL027797.
- Sens-Schönfelder, 2008, Synchronizing seismic networks with ambient noise, *Geophysical Journal International*, **174**, 966–970, doi: 10.1111/j.1365-246X.2008.03842.x.
- Sens-Schönfelder, C., and Larose, E., 2008, Temporal changes in the lunar soil from correlation of diffuse vibrations, *Physical Review E*, **78**, 045601, doi: 10.1103/PhysRevE.78.045601.
- Shapiro, S. A., 2008, Microseismicity: A tool for reservoir characterization, *EAGE Publications bv*.
- Shapiro, N. M., and Campillo, M., 2004, Emergence of broadband Rayleigh waves from correlations of the ambient seismic noise, *Geophysical Research Letters*, **31**, L07614, doi: 10.1029/2004GL019491.
- Shapiro, N. M., Campillo, M., Stehly, L., and Ritzwoller, M. H., 2005, High-resolution surface wave tomography from ambient seismic noise, *Science*, **307**(5715), 1615–1617, doi: 10.1126/science.1108339.
- Shapiro, S. A., Dinske, C., and Kummerow, J., 2007, Probability of a given magnitude earthquake induced by a fluid injection, *Geophysical Research Letters*, **34**, L22314, doi: 10.1029/2007GL031615.
- Shapiro, S. A., Krüger, O. S., Dinske, C., and Langenbruch, C., 2011, Magnitudes of induced earthquakes and geometric scales of fluid-stimulated rock volumes, *Geophysics*, **76**(6), WC55–WC63, doi:10.1190/geo2010-0349.1.

- Shemeta, J. E., Maxwell, S., Warpinski, N. R., Quimby, S., Tiebel, T., Phillips, Z., Kinsler, R., Hinds, G., Green, T. W., and Waltman, C. K., 2009, Stacking Seismograms To Improve Microseismic Images, *SPE Production & Operations*, **24**, 156-164, doi: 10.2118/108103-PA.
- Sheriff, R. E., and Geldart, L. P., 1995, *Exploration Seismology*, Cambridge University Press.
- Shumway, R. H., 2003, Time-frequency clustering and discriminant analysis, *Statistics & Probability Letters*, **63**, pp. 307–314, doi: 10.1016/S0167-7152(03)00095-6.
- Slob, E., Draganov, D., and Wapenaar, K., 2007, Interferometric electromagnetic Green's functions representations using propagation invariants, *Geophysical Journal International*, **169**(1), 60–80, doi: 10.1111/j.1365-246X.2006.03296.x.
- Slob, E., Wapenaar, K., 2007, Electromagnetic Green's functions retrieval by crosscorrelation and cross-convolution in media with losses, *Geophysical Research Letters*, **34**(5), L05307, doi: 10.1029/2006GL029097.
- Snieder, R., Grêt, A., Douma, H., and Scales, J., 2002, Coda wave interferometry for estimating nonlinear behavior in seismic velocity, *Science*, **295**, 2253–2255, doi: 10.1126/science.1070015.
- Snieder, R., 2003, Coda wave interferometry, In: McGraw-Hill (Ed.), McGraw-Hill 2004 Yearbook of Science & Technology, McGraw-Hill, New York, 54–56.
- Snieder, R., 2004, Extracting the Green's function from the correlation of coda waves: A derivation based on stationary phase, *Physical Review E*, **69** (4), 046610, doi: 10.1103/PhysRevE.69.046610.
- Snieder, R., and Hagerty, M., 2004, Monitoring change in volcanic interiors using coda wave interferometry: Application to Arenal Volcano, Costa Rica, *Geophysical Research Letters*, **31**(9), L09608, doi: 10.1029/2004GL019670.
- Snieder, R., 2006, The theory of coda wave interferometry, *Pure and Applied Geophysics*, **163**, 455–473, doi: 10.1007/s00024-005-0026-6.
- Snieder, R., Wapenaar, K., and Larner, K., 2006, Spurious multiples in seismic interferometry of primaries, *Geophysics*, **71**(4), SI111–SI124, doi: 10.1190/1.2211507.
- Snieder, R., and Safak, E., 2006, Extracting the building response using seismic interferometry: Theory and application to the Millikan Library in Pasadena, California, *Bulletin of the Seismological Society of America*, **96**(2), 586–598, doi: 10.1785/0120050109.

- Snieder, R., 2007, Extracting the Green's function of attenuating heterogeneous acoustic media from uncorrelated waves, *Journal of the Acoustic Society of America*, **121**(5), 2637–2643, doi: 10.1121/1.2713673.
- Snieder, R., Wapenaar, K., and Wegler, U., 2007, Unified Green's function retrieval by crosscorrelation; connection with energy principles, *Physical Review E*, **75**(3), 036103, doi: 10.1103/PhysRevE.75.036103.
- Stehly, L., Campillo, M., and Shapiro, N. M., 2006, A study of the seismic noise from its long-range correlation properties, *J. Geophys. Res.*, **111**, B10306, doi:10.1029/2005JB004237.
- Stehly, L., Campillo, M., and Shapiro, N. M., 2007, Traveltime measurements from noise correlation: stability and detection of instrumental time-shifts, *Geophysical Journal International*, **171**, 223–230, doi: 10.1111/j.1365-246X.2007.03492.x.
- Stehly, L., Cupillard, P., and Romanowicz, B., 2011, Towards improving ambient noise tomography using simultaneously curvelet denoising filters and SEM simulations of seismic ambient noise, *Comptes Rendus-Geoscience*, **343**(8), 591–599, doi: 10.1016/j.crte.2011.03.005.
- Stephen, R. A., Koelsch, D. E., Berteaux, H., Bocconcelli, A., Bolmer, S., Cretin, J., Etourmy, N., Fabre, A., Goldsborough, R., Goulds, M., Kery, S., Laurent, J., Omnes, G., Peal, K. R., Swift, S. A., Turpening, R., and Zani, C., 1994, The Seafloor Borehole Array Seismic System (SEABASS) and VLF Ambient Noise, *Marine Geophysical Researches*, **16**, 243–286, doi: 10.1007/BF01224745.
- St-Onge, A., Eaton, D. W., and Pidlisecky, A., 2013, Borehole vibration response to hydraulic fracture pressure, *CSEG Geoconvention, Calgary*.
- Swindell, S. W., and Snell, N. S., 1977, Station processor automatic signal detection system, phase I: final report, station processor software development: Texas Instruments final report No. ALEX (01)–FR–77–01, AFrAC contract number F08606–76–C–0025, Texas Instruments Inc., Dallas, Texas.
- Tary, J–B., van der Baan, M., and Eaton, D. W., 2014, Interpretation of resonance frequencies recorded during hydraulic fracturing treatments, *Journal of Geophysical Research: Solid Earth*, **119**, 1295–1315, doi: 10.1002/2013JB010904.
- Tary, J–B., Herrera, R. H., Han, J., and van der Baan, M., 2015, Spectral estimation - What is new? What is next?, *Rev. Geophys.*, **52**, 723–749, doi: 10.1002/2014RG000461.
- Thomson, D. J., 1982, Spectrum estimation and harmonic analysis, *Proc. IEEE*, **70**, 1055–1096, doi: 10.1109/PROC.1982.12433.

- Trampert, J., Cara, M., and Frogneux, M., 1993, *SH* propagator matrix and Q_s estimates from borehole- and surface-recorded earthquake data, *Geophysical Journal International*, **112**, 290–299, doi: 10.1111/j.1365-246X.1993.tb01456.x.
- Trnkoczy, A., 2002, Understanding and parameter setting of STA/LTA trigger algorithm, in *IASPEI New Manual of Seismological Observatory Practice*, **2**, 01-20, ed. Bormann, P., doi: 10.2312/GFZ.NMSOP-2_IS_8.1.
- Tsai, V. C., 2009, On establishing the accuracy of noise tomography travel-time measurements in a realistic medium, *Geophysical Journal International*, **178**, 1555–1564, doi:10.1111/j.1365-246X.2009.04239.x.
- Ugalde, A., Faite, B., and Villasenor, A., 2014, Temporal variations of seismic velocity at Paradox Valley, Colorado, using passive image interferometry, *Bulletin of the Seismological Society of America*, **104**(3), 1088–1099, doi: 10.1785/0120130133.
- Vaezi, Y., and DeMeersman, K., 2014, Supervirtual S-wave Refraction Interferometry for Converted Wave Statics and Near-surface S-wave Velocity Model Building, *76th EAGE Conference and Exhibition 2014, Expanded Abstract*, doi: 10.3997/2214-4609.20140996 .
- Vaezi, Y., and van der Baan, M., 2014, Analysis of instrument self-noise and microseismic event detection using power spectral density estimates, *Geophysical Journal International*, **197**(2), 1076–1089, doi: 10.1093/gji/ggu036.
- Vaezi, Y., and van der Baan, M., 2015, Interferometric assessment of clamping quality of borehole geophones, *Geophysics*, **80**(6), WC89–WC98, doi: 10.1190/geo2015-0193.1.
- van der Baan, M., 2001, Acoustic wave propagation in one-dimensional random media: The wave localization approach, *Geophysical Journal International*, **145**, 631–646, doi: 10.1046/j.1365-246X.2001.01405.x.
- van der Baan, M., 2009, The origin of SH-wave resonance frequencies in sedimentary layers, *Geophysical Journal International*, **178**, 1587–1596, doi: 10.1111/j.1365-246X.2009.04245.x.
- van der Baan, M., Eaton, D. W., and Dusseault, M., 2013, Microseismic monitoring developments in hydraulic fracture stimulation, in Bungler, A.P., McLennan, J., and Jeffrey, R., eds., *Effective and sustainable hydraulic fracturing: InTech*, 439–466, doi: 10.5772/56444.
- van Manen, D. –J., Robertsson, J. O. A., and Curtis, A., 2005, Modeling of Wave Propagation in Inhomogeneous Media, *Physical Review Letters*, **94**(16), 164301, doi: 10.1103/PhysRevLett.94.164301.

- van Manen, D. -J., Curtis, A., and Robertsson, J. O. A., 2006, Interferometric modeling of wave propagation in inhomogeneous elastic media using time reversal and reciprocity, *Geophysics*, **71**(4), SI47–SI60, doi: 10.1190/2F1.2213218.
- Van Tiggelen, B., 2003, Green function retrieval and time reversal in a disordered world, *Phys. Rev. Lett.*, **91**(24), 243904, doi: 10.1103/PhysRevLett.91.243904.
- Vasconcelos, I., 2008, Generalized representations of perturbed fields applications in seismic interferometry and migration, *SEG Technical Program Expanded Abstracts*, **27**(1), 2927–2931, doi: 10.1190/1.3063954.
- Vasconcelos, I., and Snieder, R., 2008, Interferometry by deconvolution, Part I: Theory for acoustic waves and numerical examples, *Geophysics*, **73**(3), SI15–SI28, doi: 10.1190/1.2904554.
- Verdon, J. P., Kendall, J- M., White, D. J., Angus, D. A., Fisher, Q. J. and Urbancic, T., 2010, Passive seismic monitoring of carbon dioxide storage at Weyburn, *Leading Edge*, **29**, 200–206, doi: 10.1190/1.3304825.
- Wang, Y., Luo, Y., and Schuster, G. T., 2009, Interferometric interpolation of missing seismic data, *Geophysics*, **74**(3), SI37–SI45, doi: 10.1190/1.3110072.
- Wapenaar, K., Draganov, D., Thorbecke, J., and Fokkema, J., 2002, Theory of acoustic daylight imaging revisited, *SEG Technical Program Expanded Abstracts*, 2269-2272, doi: 10.1190/1.1817165.
- Wapenaar, K., 2003, Synthesis of an inhomogeneous medium from its acoustic transmission response, *Geophysics*, **68**(5), 1756–1759, doi: 10.1190/1.1620649.
- Wapenaar, K., 2004, Retrieving the elastodynamic Green's function of an arbitrary inhomogeneous medium by cross Correlation, *Physical Review Letters*, **93**(25), 254301, doi: 10.1103/PhysRevLett.93.254301.
- Wapenaar, K., and Fokkema, J., 2006, Green's function representations for seismic interferometry, *Geophysics*, **71**(4), SI33SI46, doi: 10.1190/1.2213955.
- Wapenaar, K., Slob, E., and Snieder, R., 2006, Unified Green's Function Retrieval by Cross Correlation, *Physical Review Letters*, **97**(23), 234301, doi: 10.1103/PhysRevLett.97.234301.
- Wapenaar, K., 2006, Nonreciprocal Green's function retrieval by cross correlation, *Journal of the Acoustical Society of America*, **120**, EL7–EL13, doi: 10.1121/1.2208153.

- Wapenaar, K., Slob, E., and Snieder, R., 2008a, Seismic and electromagnetic controlled-source interferometry in dissipative media, *Geophysical Prospecting*, **56**, 419–434, doi: 10.1111/j.1365-2478.2007.00686.x.
- Wapenaar, K., van der Neut, J., and Ruigrok, E., 2008b, Passive seismic interferometry by multidimensional deconvolution, *Geophysics*, **75**(6), A51–A56, doi: 10.1190/1.2976118.
- Wapenaar, K., Draganov, D., Snieder, R., Campman, X., and Verdel, A., 2010a, Tutorial on seismic interferometry: Part 1 Basic principles and applications, *Geophysics*, **75**(5), 75A195–75A209, doi: 10.1190/1.3457445.
- Wapenaar, K., Slob, E., Snieder, R., and Curtis, A., 2010b, Tutorial on seismic interferometry: Part 2 Underlying theory and new advances, *Geophysics*, **75**(5), 75A211–75A227, doi: 10.1190/1.3463440.
- Wapenaar, K., and van der Neut, J., 2010, A representation for Green's function retrieval by multidimensional deconvolution, *The Journal of the Acoustical Society of America*, **128**(6), EL366–EL371, doi:10.1121/1.3509797.
- Warpinski, N. R., 2009, Microseismic monitoring: inside and out, *J. Pet. Technol.*, **61**, 80–85, doi: 10.2118/118537-MS.
- Warpinski, N. R., Mayerhofer, M. J., Vincent, M. C., Cipolla, C. L., and Lolon, E. P., 2009, Stimulating Unconventional Reservoirs: Maximizing Network Growth While Optimizing Fracture Conductivity, *Journal of Canadian Petroleum Technology*, **48**, 39–51, doi:10.2118/114173-MS.
- Weaver, R. L., and Lobkis, O. I., 2001, Ultrasonics without a source: Thermal fluctuation correlations at MHz frequencies, *Physical Review Letters*, **87**, 134301/1–134301/4, doi: 10.1103/PhysRevLett.87.134301.
- Weaver, R. L., and Lobkis, O. I., 2004, Diffuse fields in open systems and the emergence of the Green's function (L), *The Journal of Acoustical Society of America*, **116**, 2731–2734, doi: 10.1121/1.1810232.
- Weaver, R. L., Hadziioannou, C., Larose, E., and Campillo, M., 2011, On the precision of noise correlation interferometry, *Geophysical Journal International*, **185**, 1384–1392, doi: 10.1111/j.1365-246X.2011.05015.x.
- Wegler, U., Lühr, B. –G., Snieder, R., and Ratdomopurbo, A., 2006, Increase of shear wave velocity before the 1998 eruption of Merapi volcano (Indonesia), *Geophysical Research Letters*, **33**, L09303, doi:10.1029/2006GL025928.

- Wegler, U., and Sens-Schönfelder, C., 2007, Fault zone monitoring with passive image interferometry, *Geophysical Journal International*, **168**, 1029–1033, doi: 10.1111/j.1365-246X.2006.03284.x.
- Wegler, U., Nakahara, H., Sens-Schönfelder, C., Korn, M., and Shiomi, K., 2009, Sudden drop of seismic velocity after the 2004 Mw 6.6 mid-Niigata earthquake, Japan, observed with passive image interferometry, *Journal of Geophysical Research*, **114**, B06305, doi: 10.1029/2008JB005869.
- Welch, P. D., 1967, The use of fast Fourier transform for the estimation of power spectra: a method based on time averaging over short, modified periodograms, *IEEE Transactions on Audio and Electroacoustics*, **15**, 70–73, doi: 10.1109/TAU.1967.1161901.
- White, J. E., 1965, Seismic waves: Radiation, transmission, and attenuation, *McGraw-Hill Book Co.*
- Willis, M. E., Lu, R., Campman, X., Toksöz, M. N., Zhang, Y., and de Hoop, M. V., 2006, A novel application of time-reversed acoustics: Salt-dome flank imaging using walkaway VSP surveys, *Geophysics*, **71**(2), A7–A11, doi: 10.1190/1.2187711.
- Withers, M., Aster, R., Young, C., Beiriger, J., Harris, M., Moore, S., and Trujillo, J., 1998, A comparison of select trigger algorithms for automated global seismic phase and event detection, *Bulletin of the Seismological Society of America*, **88**(1), 095–106.
- Xiao, X., Zhou, M., and Schuster, G. T., 2006, Salt-flank delineation by interferometric imaging of transmitted P- and S-waves, *Geophysics*, **71**(4), SI197–SI207, doi: 10.1190/1.2209550.
- Xiao, X., Luo, Y., Fu, Q., Jarvis, M., Dasgupta, S., and Kelamis, P., 2009, Locate Microseismicity by Seismic Interferometry, *EAGE, Extended Abstracts*, A22, doi: 10.3997/2214-4609.20146748.
- Xue, Y., Dong, S., and Schuster, G. T., 2009, Interferometric prediction and subtraction of surface waves with a nonlinear local filter, *Geophysics*, **74**(1), SI1–SI8, doi: 10.1190/1.3008543.
- Yang, Y., and Ritzwoller, M. H., 2008, Characteristics of ambient seismic noise as a source for surface wave tomography, *Geochemistry, Geophysics, Geosystems*, **9**, Q02008, doi:10.1029/2007GC001814.
- Yao, H., Van Der Hilst, R. D., and De Hoop, M. V., 2006, Surface-wave array tomography in SE Tibet from ambient seismic noise and two-station analysis - i. Phase velocity maps, *Geophysical Journal International*, **166**, 732–744. doi: 10.1111/j.1365-246X.2006.03028.x.

- Yu, J., and Schuster, G. T., 2006, Crosscorrelogram migration of inverse vertical seismic profile data, *Geophysics*, **71**(1), S1–S11, doi: 10.1190/1.2159056.
- Zhan, Z., Tsai, V. C., and Clayton, R. W., 2013, Spurious velocity changes caused by temporal variations in ambient noise frequency content, *Geophysical Journal International*, **194**(3), 1574–1581, doi: 10.1093/gji/ggt170.
- Zhang, J., Gerstoft, P., and Shearer, P. M., 2010, Resolving P-wave traveltimes anomalies using seismic array observations of oceanic storms, *Earth and Planetary Science Letters*, **292**, 419–427, doi: 10.1016/j.epsl.2010.02.014.
- Zhao, P. -P. , Chen, J. -H., Michel, C., Liu, Q. -Y., Li, Y., Li, S. -C., Guo, B., Wang, J., Qi, S. -H., 2012, Crustal velocity changes associated with the Wenchuan M8.0 earthquake by auto-correlation function analysis of seismic ambient noise, *Chinese Journal of Geophysics*, **55**, 137–145 (in Chinese with English abstract), doi: 10.6038/j.issn.0001-5733.2012.01.013.
- Zhou, R., Huang, L., Rutledge, J. T., Fehler, M., Daley, T. M., and Majer, E. L., 2010, Coda-wave interferometry analysis of time-lapse VSP data for monitoring geological carbon sequestration, *International Journal of Greenhouse Gas Control*, **4**(4), 679–686, doi: 10.1016/j.ijggc.2010.01.010.